Identification of an Unsteady Aerodynamic Model up to High Angle of Attack Regime

By

Yigang Fan

Dissertation submitted to the Faculty of
Virginia Polytechnic Institute and State University
in partial fulfillment of the requirements for the degree of

Doctor of Philosophy
in
Aerospace Engineering

Approved:

Dr. Frederick H. Lutze, Chairman

Dr. Mark R. Anderson

Dr. Eugene M. Cliff

Dr. Wayne C. Durham

Dr. Roger L. Simpson

November 1997

Blacksburg, Virginia

Identification of an Unsteady Aerodynamic Model up to High Angle of Attack Regime

By

Yigang Fan

Committee Chairman: Dr. Frederick H. Lutze

Aerospace Engineering

(ABSTRACT)

The harmonic oscillatory tests for a fighter aircraft configuration using the Dynamic Plunge-Pitch-Roll (DyPPiR) model mount at Virginia Tech Stability Wind Tunnel are described and analyzed. The corresponding data reduction methods are developed on the basis of multirate digital signal processing techniques. Since the model is sting-mounted to the support system of DyPPiR, the Discrete Fourier Transform (DFT) is first used to identify the frequencies of the elastic modes of sting. Then the sampling rate conversion systems are built up in digital domain to resample the data at a lower rate without introducing distortions to the signals of interest. Finally linear-phase Finite Impulse Response (FIR) filters are designed by Remez exchange algorithm to extract the aerodynamic characteristics responses to the programmed motions from the resampled measurements. These data reduction procedures are also illustrated through examples.

The results obtained from the harmonic oscillatory tests are then illustrated and the associated flow mechanisms are discussed. Since no significant hysteresis loops are observed for the lift and the drag coefficients for the current angle of attack range and the tested reduced frequencies, the dynamic lags of separated and vortex flow effects are small in the current oscillatory tests. However, large hysteresis loops are observed for pitch moment coefficient in the current tests. This observation suggests that at current flow conditions, pitch moment has large pitch rate and $\dot{\alpha}$ dependencies. Then the nondimensional maximum pitch rate $\hat{q}_{max}$ is introduced to characterize these harmonic oscillatory motions. It is

found that at current flow conditions, all the hysteresis loops of pitch moment coefficient with same $\hat{q}_{max}$ are tangential to one another at both top and bottom of the loops, implying approximately same maximum offset of these loops from static values. Several cases are also illustrated.

Based on the results obtained and those from references, a state-space model is developed to describe the unsteady aerodynamic characteristics up to the high angle of attack regime. A nondimensional coordinate is introduced as the state variable describing the flow separation or vortex burst. First-order differential equation is used to govern the dynamics of flow separation or vortex bursting through this state variable. To be valid for general configurations, Taylor series expansions in terms of the input variables are used in the determination of aerodynamic characteristics, resembling the current approach of the stability derivatives. However, these derivatives are longer constant. They are dependent on the state variable of flow separation or vortex burst. In this way, the changes in stability derivatives with the angle of attack are included dynamically. The performance of the model is then validated by the wind-tunnel measurements of an NACA 0015 airfoil, a 70^o delta wing and, finally two F-18 aircraft configurations. The results obtained show that within the framework of the proposed model, it is possible to obtain good agreement with different unsteady wind tunnel data in high angle-of-attack regime.

Acknowledgments

During the last four years, I was fortunate to work with Dynamics and Control Research Group in the Department of Aerospace and Ocean Engineering at Virginia Polytechnic Institute and State University. The unique environment of cooperation and support both in studies and research encouraged and greatly contributed to my academic and professional growth.

In the very first lines of this work, I would like to express my deep gratitude and thankfulness to my advisor and committee chair, Dr. Frederick H. Lutze. From my very first days at Virginia Tech, he was a source of guidance, support and help. No matter what kind of problem was discussed, his advice and encouragement always provided new perspectives. The expertise that he shared with me remains a tremendous source for the professional growth to me. I am very thankful for everything he has done for me.

Also, I am deeply indebted to Dr. Eugene M. Cliff. His help, advice and support could not be overestimated, especially in summer of 1994 when I was in a difficult situation, he helped through this period. All his extraordinary help are greatly appreciated.

I am thankful to all the members of my committee: Dr. Mark R. Anderson, Dr. Wayne C. Durham and Dr. Roger L. Simpson. Their expertise and assistance played an important role in the progress of my research. I am grateful for all their efforts.

The great contribution to what I have done in this research was made by Dr. Todd G. Wetzel and Dr. Jonathan L. Fleming, who were responsible for running the wind tunnel and taking the data. It is their efforts that make this research possible. Their key contributions are deeply appreciated. Other individuals from whom I benefited in this research included, but were not limited to, Daniel C. Lluch, Gregory Stagg, Troy B. Jones and Yufei Wu.

Financial support for this research project was provided by NASA Langley Research Center, under grant NAG1-1737. I am thankful to our contract monitor, Sue B. Grafton, and other individuals who assisted with this project.

Foremost, I wish to thank my parents Yanru and Run Fan, who always provide guidance and on whom I can rely upon everything I do. They made me understand the great power of knowledge.

This work would not be accomplished without two most precious persons in my life. Their everyday patience, love, and care are the driving force for all my achievements. Expressing my deepest love to my son Pengyu and my wife Yuling, I dedicate this work to them.

Contents

List of Figures

List of Tables

Chapter 1

Introduction

Determining and describing the aerodynamic forces and moments on an aircraft is a very important subject in atmospheric flight mechanics. It is primarily this aerodynamic ingredient that distinguishes flight mechanics from other branches of mechanics. Aerodynamic forces and moments are, strictly speaking, functionals of the variables associated with flight conditions. They are dependent not only on the instantaneous values of these variables but also on their entire past histories. Practically, we can write the aerodynamic forces and moments as functions of these variables and all their derivatives, and expand them as Taylor series about some reference values. Based on this assumption, certain practical schemes have been developed for the flight mechanics and control applications. In this chapter, we first discuss the current approaches used in describing the aerodynamic characteristics. Then we will review some typical wind-tunnel investigations of unsteady aerodynamics up to the high angle of attack regime. The mechanisms associated with these results will also be discussed. Finally, we will summarize our research work and briefly disscuss the major results obtained in this dissertation.

1.1 Stability Derivative Approach

For many years, the aerodynamic forces and moments were approximated by the linear expressions in their Taylor series expansions, leading to the concept of stability and control derivatives[1−3]. This approximation has been found to work extremely well for attached flows at low angles of attack. Furthermore, the addition of nonlinear terms, expressing the changes in stability derivatives with angle of attack, can extend the range of flight applications. Thus, a major fraction of the total effort in the aerodynamic research in the past has been devoted to the determination, by theoretical and experimental means[3], of the aerodynamic derivatives needed for applications to flight mechanics and controls. The in-phase and out-of-phase derivative approach[3], for example, is the approach using the experimental measurements of oscillatory motions in the determination of these aerodynamic derivatives. We will describe this approach in detail in Appendix A.

In the above approach, however, using either linear or nonlinear aerodynamics, it is assumed that the parameters appearing in the representations are time-invariant. This assumption was many times questioned based on studies of unsteady aerodynamics. Especially in the region of high angles of attack where separated and vortex flows are developed, this representation becomes invalid. The values of the unsteady aerodynamic derivatives are found to be strongly dependent on the amplitude and frequency of the aircraft oscillations. As the high angle-of-attack region becomes more accessible for modern aircraft, properly modeling the aerodynamic characteristics in this region is highly desirable.

1.2 Nonlinear Lifting Line Formulation

The nonlinear lifting line theory was studied in the application of modeling the aerodynamics in poststall range by Levinsky[4] and Hreha[5]. In their works [4-5], a nonlinear lifting line

procedure with unsteady wake effects has been developed for predicting wing-body aerodynamic characteristics up to and beyond stall. A discrete vortex lattice representation is used for the time dependent wake. Each chordwise section is assumed to act aerodynamically like a 2-D airfoil in steady flow at an effective angle of attack, which may be time dependent. Their approach and procedure may prove useful for simulating and aleviating such adverse wing stalling characteristics as wing rock, wing drop, loss of roll control or roll control reversal. However, while this method models the effects of the aerodynamic time histories of the wake, it does not model the dynamics of the flow separation and vortex burst which is important for unsteady aerodynamics in poststall range.

1.3 Indicial Function Method

Another more accurate approach used to obtain the airloads on an aircraft undergoing an arbitrary motion is the indicial function method[6−8] in conjunction with the superposition principle.

$$\vec{C} = \int_0^t A(t-\tau)\dot{\vec{h}}d\tau$$

where $\vec{C} = (C_x, C_y, C_z, C_l, C_m, C_n)^T$ is the combined vector of total aerodynamic force and moment coefficients, $A = \{a_{ij}\}$ is a matrix of indicial response functions for stepwise variation of kinematic parameters, such as angle of attack and sideslip, roll, pitch and yaw rates, and control surface deflections which form a vector $\vec{h} = (\alpha, \beta, p, q, r, \delta_a, \delta_e, \delta_r)^T$.

This approach is certainly efficient, but it is difficult to combine this functional representation with the equations of an aircraft motion, which are expressed in the form of differential equations. In such a case, the resulting equations of motion will be represented by a set of integral-differential equations which are not convenient for the analysis. Such an approach can also be extended to a nonlinear case corresponding to the separated and vortex flow

conditions[8]. But in this case, the use of such a description becomes very complicated and very difficult to handle.

1.4 State-Space Representations

The description of the unsteady aerodynamic characteristics associated with the motion time history is certainly possible by utilizing ordinary differential equations[9−10]. In order to describe the aerodynamic characteristics measured experimentally $\vec{C}(t) \in R^6$, the following type of the input-output dynamic system can be assumed:

$$D_i(\vec{C}, \quad \frac{d\vec{C}}{dt}, ..., \frac{d^k\vec{C}}{dt^k}) = N_i(\vec{h}, \frac{d\vec{h}}{dt}, ..., \frac{d^m\vec{h}}{dt^m})$$
$$\vec{C} \in R^6, \quad \vec{h} \in R^8, \ i = 1, 2, ..., 6$$

where D_i and N_i are some nonlinear functions, to be determined.

This approach has been found to be very interesting since it is easy to combine this functional representation with the equations of motion of an aircraft for solving flight mechanics problems. The inclusion of the unsteady aerodynamics simply leads to an increase in the problem dimensions. In such a case, we can analyze the motion stability by means of classical methods. Another interesting aspect is that this representation results in the concept of state which is a very important part for describing the dynamic system of the aerodynamic characteristics. It gives the information required for the determination of the instant and future values of the aerodynamic characteristics. This description becomes the so-called state-space representation[11−14] of aerodynamics systems.

In Ref. [12], a method is presented to model the unsteady lift, drag, and pitch moment acting on a two-dimensional airfoil operating under attached flow conditions. Starting from suitable generalizations and approximations to aerodynamic indicial functions, the

unsteady airloads due to an arbitrary forcing motion are represented in a state-space formulation. This model is in a form compatible with the aeroelastic analyses of both fixed-wing and rotary-wing systems. But this model is linear and only valid for attached flows at low angles of attack, where there are no separated and vortex flows.

Goman and Khrabrov[13] are the first to propose a state-space representation to model unsteady aerodynamics at high angles of attack. They start from the flowfield around an airfoil up to high angles of attack and introduce an internal variable to describe the location of the separation point on the upper surface of the airfoil. Since the quasi-steady and unsteady aerodynamic effects, such as the circulation and the boundary-layer convection lag, as well as the dynamic properties of the separated flow adjustment, influence the conditions of the flow separation and its reattachment, the instant position of the separation point depends on all these effects. The aerodynamic coefficients depend in turn on the kinematic parameters of the motion and the position of flow separation. Based on these analyses, the location of the separation point is defined as the state of the aerodynamic system which gives the information required for the determination of the current and future values of the aerodynamic characteristics. A first-order differential equation is developed to govern the movement of this separation point. Using this state variable and kinematic parameters in determination of aerodynamic coefficients, a state-space representation is built to model the unsteady aerodynamics up to high angle of attack regime.

In this formulation, however, one problem is that there are no explicit expressions available in determining the aerodynamic characteristics from the state and kinematic parameters for general configurations. Furthermore, for complex configurations, there exist a lot of separation points associated with vortex flows, and these flows can interact with each other. In such complex hybrid flowfields, is this state-space model still valid in describing the unsteady aerodynamic characteristics ? Extensive research efforts are expected to investigate these aspects.

1.5 Experimental Investigations

In order to properly model the unsteady aerodynamics, the flow physics and mechanisms have to be well-understood on the basis of experimental investigations. The experimental study of dynamic stall can be traced back several decades[15], and has appeared with increasing abundance up to the present. The experimental conditions range from the effect of a constant rate of change of angle of attack (constant-$\dot{\alpha}$)[18−19], to various nonconstant-$\dot{\alpha}$ pitching, the most common of which is oscillatory motion[13−22]. The models tested range from 2-D airfoils, 3-D delta wings, to full aircraft.

1.5.1 Typical Results for Airfoils

A fundamental study of unsteady lift on an airfoil due to abrupt changes in the angle of attack was made by Wagner in Ref. [16]. This work was extended by Theodorsen to computing forces and moments on an oscillating airfoil, whereas Kussner and Sears studied the lift on an airfoil as it penetrated a sharp-edge or harmonically varying gust, respectively (see Ref. [17]). In more recent years, the wind-tunnel studies of dynamic stall for an NACA 0015 airfoil pitching up about the midchord at a constant rate were reported by Jumper, *et al*[18−19]. They studied the flowfields of the airfoil from attachment to separation and determined the lift and moment coefficients as functions of angle of attack for 100 test cases, covering 20 dynamic airspeed and pitch rate combinations. The dynamic-stall effects of the change in the angle of attack at which separation occurs at the quarter chord and the change in the angle of attack at which stall occurs were found to relate to a nondimensional pitch rate given by the chord times the pitch rate divided by two times the freestream velocity. Their results showed that there are significant delays of the stall and the magnitude of the maximum lift coefficient from the static values for the ramping airfoil. These delays are found to be proportional to the variation of angle of attack for fixed freestream velocity.

Niven and Galbraith[20] presented the experimental results for ramp-down motion of airfoils from fully stalled conditions to full establishment of the attached flows. Significant delays of flow reattachment to a negative flow incidence in a rapid pitch-down motion have been observed. Based on these experimental results, an analysis has been performed by Ericsson[21−23] to explain that the flow physics responsible for the observed delays are the accelerated flow and "moving wall" effects. The analysis shows that the dominant role played by the moving wall effect during pitch-down motions is in agreement with existing experimental results for a rotating circular cylinder. However, the delays of reattachment may not be the same as those of flow separations.

1.5.2 Typical Results for Delta Wings

For the flowfields on a swept delta wing, a central feature of the vortex formation from a swept leading edge at finite incidence angle is the vortex core. At a sufficiently high angle of attack, this core breaks down, causing loss of local lift. For stationary wings, the location of vortex breakdown x_b, defined as the distance from the nose of the wing at which the vortex core diameter abruptly increases, attains its minimum value at maximum angle of attack, and conversely. A full description of these and other features, as well as a synopsis of theoretical development pertaining to flows past wings and analogous internal tube flows, was given by Wedemeyer[24].

Characterization of the unsteady nature of vortex breakdown on a delta wing subjected to periodic excitation has remained unsolved. Basic features of the vortex developemnt and breakdown on a wing oscillating in pitch are reported by Rockwell *et al*[25−26] and Brandon[30]. In general, it is expected that the location of vortex breakdown x_b will exhibit a hysteresis loop as angle of attack is varied. This hypothesis is based on the analogous findings for a two-dimensional airfoil subjected to a pitch motion[27], as well as visualization of the overall flow structure on an oscillating delta wing[28]. In the latter, it was revealed

that the gross behavior of the vortical flow structure was hysteretic with respect to the wing motion. This investigation focuses on the development and breakdown of the core of the vortex, defined by the vorticity fed into the vortex at and near the nose of the wing.

The fluid-mechanical processes that are causing these hysteresis loops are explained as the dynamic lags of delta wing vortex breakdown in the high-rate and large-amplitude pitch oscillations also in Ref. [29].

1.5.3 Typical Results for Aircraft

A significant amount of experimental research has been conducted in the area of unsteady aerodynamics at high angles of attack. However, few of the works to date have focused on full aircraft. Current design trends for advanced aircraft configurations show a clear need for extending the experimental research to a complete aircraft configuration.

Brandon[30] is probably the first one to investigate and publish the unsteady aerodynamic tests for an F-18 aircraft in ramp motions up to high angles of attack regime. The test configuration incorporated a moderately swept wing with a highly swept leading-edge extension (LEX) which generates concentrated vortical flowfields similar to those of delta wings. In addition to the vortical flowfields, the aircraft has moderately swept wings and tail surfaces that can create separated flows over the configuration at high angles of attack. These two types of flowfields can interact with each other. In such a hybrid flowfield, both the separation and vortex burst phenomena exist, and it is not easy to describe the locations of flow separation and vortex bursts.

The static results show that the flowfield over the model at high angles of attack is dominated by a strong vortex system generated by the LEX. This vortex system contributes both to increased lift and reduced pitch stability. Development of the LEX vortex system starts at very moderate angles of attack. At these conditions, the vortex system trails over

the wing and passes just outboard of the vertical tails. With increasing angle of attack, breakdown of the vortices progresses forward such that the burst point moves over the wing and LEX, and is associated with a substantial decrease in lift and a substantial increase in pitch stability.

For the aircraft pitching up at constant rate, an increase in lift coefficient due to pitch rate over entire range of motion has been observed and the maximum increment of the lift coefficient occurred beyond the angle of attack for maximun lift of the static test. A number of factors must be responsible for these observations. The dominant one is the flow lag associated first with flow separation and vortex formation at the low angles of attack, and then with vortex breakdown at the higher angles of attack.

For the aircraft pitching down at constant rate, the flow condition on the model is characterized by complete flow separation and vortex breakdown at the beginning. During the pitch-down motion, the formation of the LEX vortex system lags in comparison to the static case and reattachment of the wing flow is delayed. This behavior results in large decreases in lift coefficient compared to those in the static case at the same angle of attack due to the motion. As pitch rate is increased, the loss in lift increases due to the lags in vortex development and wing flow reattachment.

These experimental studies of the unsteady aerodynamics at high angle of attack regime show significant dynamic effects of the separated and vortex flows. However, the physics and mechanisms associated with the these complex separated and vortex flows are still not completely understood. Further studies are expected in this area.

1.6 Current Research

The research work in this dissertation can roughly be classified in four parts, i.e., harmonic oscillatory tests and data reduction, oscillatory aerodynamic data analysis, aerodynamic modeling, and model performance validation. Each part and the main results can be summarized as follows.

1.6.1 Harmonic Oscillatory Tests and Data Reduction

In current research, we first conduct experimental studies on the unsteady aerodynamic characteristics of a fighter aircraft configuration through the harmonic oscillatory tests at Virginia Tech. The model was sting-mounted on the Dynamic Plunge-Pitch-Roll (DyPPiR) model mount in the Virginia Tech Stability Wind Tunnel through a six-component strain-gage balance. In order to reduce the interference effects of the support system, a sting mount used is relatively long. Thus, the elastic deformations of the sting in the tests are not negligible. The associated elastic modes will enter the system as extra inputs when the model is put into the pitch oscillations. Therefore, the measurements obtained include the aerodynamic responses to the pre-programmed inputs and the aerodynamic responses to the elastic deformation of the sting, plus the corresponding inertia loads due to the actual motions of the aircraft. Since the elastic motions of the sting are not measurable in the tests, data reduction becomes a nontrivial problem. To obtain the aerodynamic responses to the programmed input time histories, we design a data reduction system in the digital domain on the basis of multirate digital signal processing approach to process the data. First we identify the frequencies of the elastic modes of sting by using Discrete Fourier Transforms (DFT). Then we design the sampling rate conversion system in the digital domain to reduce the bandwidth of interest since the sampling frequencies are much higher than the signal frequencies of interest. In this resampling process, the effects of the

noise and the sting modes with high frequencies are removed. Finally, we design Finite Impulse Response (FIR) digital filters with linear phase characteristics to reject the effects of the dominant mode of the sting. All these processes compose the digital system of data reduction. After these operations in the digital domain, we reject all the effects of the elastic modes of sting, and end up with the aerodynamic characteristics responses to the pre-programmed motion.

1.6.2 Oscillatory Aerodynamic Data Analysis

Numerous studies have documented the hysteresis and overshoot characteristics as the model is undergoing pitch oscillations at high angles of attack. The flow mechanisms responsible for these unsteady effects are the dynamic lags of the vortex bursting and flow separations. Because of these flow lags, it is generally expected that the aerodynamic forces and moments will exhibit similar hysteresis loops in the pitch oscillatory maneuvers. In the current pitch oscillatory tests, however, the tested angle of attack range is below 40^o and the reduced frequencies $\hat{\omega} = \omega c/2V$ in the tests are not large. In such testing conditions, the flowfields may not result in significant dynamic effects of vortex bursting and flow separations.

From results obtained, we observed no significant hysteresis loops for the lift and the drag coefficients in the oscillations for the current angle of attack range and the frequencies. This observation suggests that the dynamic lags of the vortex and separation flows are small in the current oscillatory maneuvers. The flowfields around the model are pretty much at the attached flow conditions. However, we see the significant hysteresis loops for the pitch moment coefficients in such flow conditions. It can further be observed that these hysteresis loops are dependent on the amplitudes, the frequencies and the mean angles of attack of the oscillations. The unsteady aerodynamic characteristics responsible for the pitch moment hysteresis loops are attributed to the effects of pitch rate and $\dot{\alpha}(t)$. The associated flow mechanisms are discussed in this dissertation. Then the nondimensional analyses about the characteristics of these hysteresis loops are performed. The nondimensional maximum pitch rate $\hat{q}_{max}$ is introduced to characterize these harmonic oscillations since it contains the information of both the amplitude and frequency of the oscillatory maneuvers. The performance of $\hat{q}_{max}$ in characterizing the unsteady aerodynamic characteristics in the harmonic oscillations is shown through several examples.

1.6.3 Aerodynamic Modeling

Based on the data we obtained and some other data at high angles of attack obtained from several documents, we develop a state-space model to describe the unsteady aerodynamic characteristics up into the high angle of attack regime. The purpose is to extract a good aerodynamic model from selected wind tunnel data by using an identification method. We start from the model as proposed by Goman and Khrabrov[13]. However we further develop the model in several aspects in order to analyze more complex unsteady aerodynamics problems at high angles of attack. The state of flow separation or vortex burst is still described by a first order differential equation but the effects of body rate on the flow separation and vortex burst are included. In order to be valid for general configurations, Taylor series expansions in terms of input variables are used for the determination of aerodynamic coefficients, resembling the current approach of stability derivatives. However these derivatives are no longer constant. They become functions of state variables which can strongly depend on the amplitude and frequency of aircraft oscillations. The minimum mean-square error approach is used to identify the unknown parameters in the model from wind tunnel data.

1.6.4 Model Performance Validation

The performances of the proposed model are first validated by using the wind tunnel data of an airfoil and a 70^o delta wing in describing the dynamics of flow separation and vortex bursting respectively. The corresponding dynamic properties of these two flowfields are discussed. Based on the fact that the model can be used to describe the dynamics of flow separation and vortex bursting individually, it is further used to describe the flowfield around a full aircraft, where both flow separation and vortex bursting exist. The unsteady wind tunnel measurements for a configuration of an F-18 aircraft are used to validate the

model performance in describing such a hybrid flow. All these results and analyses show that within the framework of the proposed state-space representation, it is possible to model more complex unsteady aerodynamics at high angles of attack for a full aircraft.

Based on these examples, we further apply this model to the harmonic oscillatory data we obtained for the F-18 aircraft configuration even though there are no large separated and vortex flow effects in the corresponding flowfields. The identification results show several nice features of the proposed model. These include the aerodynamics prediction capability, characteristics time scales, and significant improvement to the traditional stability derivative approach.

1.7 Presentations of the Current Research

The harmonic oscillatory tests and the associated digital systems of data reduction are presented in Chapter 2. In Chapter 3, we discuss the flow mechanisms associated with these oscillatory maneuvers and perform the nondimensional analyses in characterizing the corresponding unsteady aerodynamics. The state-space model is then developed in Chapter 4. The parameter identification approach is described in Chapter 5. In Chapter 6, the model performance is validated using the wind tunnel measurements of a NACA 0015 airfoil and a 70^o flat delta wing in describing the dynamics of flow separation and vortex bursting. Based on the results obtained, the model is further used to describe the flowfields around full aircraft for the ramp motion up to high angles of attack with flow separation and vortex bursting, and the harmonic oscillatory motions with delay effects due to $\dot{\alpha}$. The performance of the proposed model are also shown. In Chapter 7, we summarize the present work and make suggestions for future research. In appendix A, we discuss the method of computing the stability derivatives using the concept of in-phase and out-of-phase derivatives.

Chapter 2

Harmonic Oscillatory Tests and Data Reduction

Several references have documented the hysteresis loops of aerodynamic responses versus the angle of attack for a wing oscillating in pitch[24−26]. In general, it is thought that the location of vortex breakdown or separation point exhibit a hysteresis loop as angle of attack is varied. This hypothesis is based upon the findings for a two-dimensional airfoil subjected to pitching motion[27], as well as visualization of the overall flow structure on an oscillating delta wing[28]. Here in the present research, low-speed wind tunnel experiments were conducted to explore the unsteady aerodynamic characteristics of a modern fighter aircraft configuration through the harmonic oscillatory motions. The purpose is to provide some insights into the mechanism of hysteresis loops for a full aircraft whose flowfield includes both vortex flows and separation flows. The harmonic oscillatory motions of interests include the oscillations in pitch, as well as the oscillations in plunge. The pitch oscillations involve the effects of both $\dot{\alpha}(t)$ and pitch rate $q(t)$ while the plunge oscillations only have the $\dot{\alpha}(t)$ effects.

First we present the static test results for this aircraft, and briefly discuss the associated aerodynamic characteristics. Then we describe the harmonic oscillatory tests of current

interest, including the amplitudes, the frequencies, and the mean angles of attack, both for the oscillations in pitch and the oscillations in plunge. Since these harmonic oscillatory tests were conducted through the Dynamic Plunge-Pitch-Roll (DyPPiR) model mount, a new apparatus installed in the Virginia Tech Stability Wind Tunnel, we then analyze the DyPPiR dynamic tests and develop, in detail, the data reduction techniques specifically for the DyPPiR data acquisition system based on a multirate signal processing approach. Finally we illustrate the developed data reduction techniques by processing the experimental data for an oscillatory maneuver in pitch, as well as an oscillatory maneuver in plunge.

2.1 Static Tests and Results

The static tests were conducted at dynamic pressure Q of approximately 10 lbs/ft^2. The static data were obtained over an angle-of-attack range of -6^o to 40^o. The longitudinal force and moment data measured in the current tests are presented as the corresponding coefficients in Figures 2.1 (a) and (b).

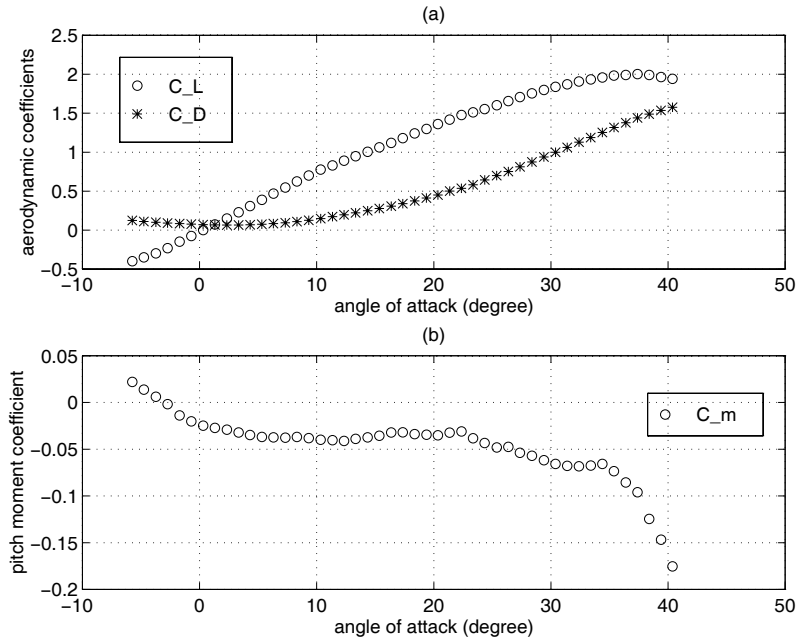

Figure 2.1: (a) Static lift and drag coefficients (b) Static pitch moment coefficient

Figure 2.1 (a) shows a linear variation in lift with angle of attack up to about 20^o. At this point, the lift-curve slope begins to decrease. This reduction in lift-curve was possibly caused by the development of flow separation and the progression of the leading-edge extention(LEX) vortex burst point onto the wing. However, lift continued to increase until a maximum value was reached at about $\alpha = 35^o$. The drag shows a quadratic variation with the angle of attack. Figure 2.1 (b) shows the pitching moment characteristics. The results

indicate near neutral stability for angles of attack between 5^o and 20^o. This characteristic is due in large part to the lift produced on the LEX ahead of the moment reference center. Above $\alpha = 35^o$, the data show a substantial increase in pitch stability.

2.2 Harmonic Oscillatory Motions in Current Tests

The harmonic oscillatory motions in current wind-tunnel tests include sinusoidal oscillations in pitch and sinusoidal oscillations in plunge.

The mathematical descriptions for the oscillatory motions in pitch are given as following,

$$\begin{aligned} \alpha(t) &= \alpha_0 + \alpha_A sin(\omega t) \\ \dot{\alpha}(t) &= \alpha_A \omega cos(\omega t) \\ \hat{q}(t) &= \frac{c}{2V}\dot{\alpha}(t) = \hat{q}_{max} cos(\omega t) \end{aligned} \tag{2.1}$$

$\hat{q}_{max}$ is the normalized maximum pitch rate which is defined as,

$$\hat{q}_{max} = \frac{c}{2V}\alpha_A \omega \tag{2.2}$$

As one can see that the sinusoidal oscillatory pitch motions are characterized by the amplitude α_A (degrees), the frequency $f = \omega/2\pi$ (Hz), and the mean angles of attack α_0 (degrees). The DyPPiR was programmed to generate the oscillatory pitch motions according to the description in Eq.(2.1) for the amplitudes, the frequencies and the mean angles of attack of interest, and the corresponding aerodynamic forces and moments were measured by an internal six-component strain-gage balance.

Currently, we investigated the aerodynamic characteristics of the sinusoidal pitch oscillations for four amplitudes (5 degrees, 7.07 degrees, 10 degrees and 14.14 degrees), four

frequencies (0.5 Hz, 0.707 Hz, 1.0 Hz and 1.414 Hz), and three mean angles of attack (0 degrees, 12 degrees and 24 degrees) at two tunnel speeds of 95 ft/s and 67 ft/s, respectively.

For the oscillatory motions in plunge, the mathematical descriptions can be expressed as follows,

$$\begin{aligned} h(t) &= h_A sin(\omega t) \\ \dot{h}(t) &= h_A \omega cos(\omega t) \\ \alpha(t) &= tan^{-1} \frac{V sin(\alpha_0) - \dot{h}(t) cos(\alpha_0)}{V cos(\alpha_0) + \dot{h}(t) sin(\alpha_0)} \\ \dot{\alpha}(t) &= \frac{V h(t) \omega^2 cos^2[\alpha(t)]}{[V cos(\alpha_0) + \dot{h}(t) sin(\alpha_0)]^2} \\ \hat{q}(t) &= 0 \end{aligned} \tag{2.3}$$

where V is the tunnel speed. $h(t)$ is the DyPPiR plunge distance from the nominal position and h_A is the amplitude of the oscillations.

As we can see, from Eq.(2.3), that the pitch rate $\hat{q}(t)$ is zero in the oscillatory motions in plunge. Only $\dot{\alpha}(t)$ shows up in the motion time histories. Therefore we can investigate the $\dot{\alpha}(t)$ effects on the aerodynamic characteristics while ,on the other hand, in the oscillatory motions in pitch, $q(t) = \dot{\alpha}(t)$, and the $\dot{\alpha}(t)$ effects can't be separated from those of the pitch rate $q(t)$.

The oscillatory motions in plunge are characterized by the plunge amplitude h_A, the frequency $f = \omega/2\pi$, and the mean angle of attack α_0. In current wind-tunnel tests, we investigated the maneuvers for two amplitudes (0.5 ft and 1.0 ft), two frequencies (1.0 Hz and 1.5 Hz), and two mean angles of attack (0 degrees and 24 degrees) at the tunnel speed of 67 ft/s only. The DyPPiR is programmed to perform the sinusoidal oscillations as formulated in Eqs.(2.1) and (2.3), and the associated data acquisition system measures the corresponding forces and moments on the model, as well as the motion time histories. However, the DyPPiR only measures the time histories of the angle of attack $\alpha(t)$ and

the plunge position $h(t)$ of the motion. The $\dot{\alpha}(t)$ and the pitch rate $q(t)$ time histories have to be obtained from the measurements by numerical differentiation techniques. In the following, we are going to analyze these oscillatory tests and develop the data reduction methods based on the multirate signal processing techniques.

2.3 Dynamic Test Analyses and Sting Modeling

The DyPPiR is installed in Virginia Tech's Stability Wind Tunnel as shown in Figure 2.2. It combines three hydraulic actuators to plunge a model through a 4.92 ft (1.5m) range vertically, pitch the model through $\pm 45^o$ range, and roll the model through a $\pm 140^o$ range. The three actuators provide the power required to force 3.08 slug (45 kg) model and over 17.13 slug (250 kg) DyPPiR hardware at rates approaching 29.53 ft/s (9 m/s) in plunge and over 90 deg/s in pitch. The DyPPiR is digitally controlled by a personal computer, so it is capable of performing general pre-programmed maneuvers, however only the harmonic sinusoidal oscillations are of current interest.

As one can see, from Figure 2.2, the model is mounted on an internal six-component strain-gage balance, which in turn is mounted on one end of a sting. The other end of the sting is mounted on the DyPPiR support system. In order to avoid the interference effects of the support system, the sting is relatively long. The current sting is of a length of approximately 4 feet, and is not very stiff in structure. In this case, the sting will be subject to elastic deformation during the tests. Similarly, since the balance has the sting part and model part, a part mounted to the sting and a part mounted to the model separated by beam flexible elements, there exists elastic deformation between these two parts when the DyPPiR is performing a maneuver. Therefore the elastic deformations of the sting and the balance will change the actual angle of attack of the model when the model is put into a sinusoidal oscillation. These structural effects of the balance and the sting, however, have

to be identified and considered in the data reduction.

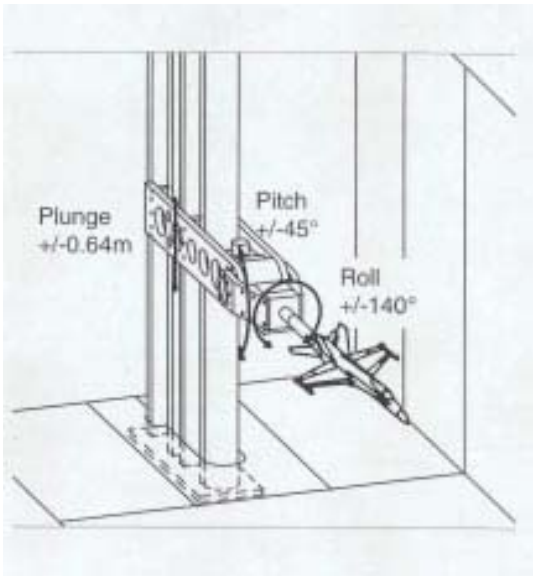

Figure 2.2: DyPPiR Model Mount installed in the wind tunnel

Currently, we assume that the balance is rigid because its elastic deformation is very small compared with that of the sting. With this assumption, we further model the sting as a cantilever beam with the model mounted on the free end as shown in Figure 2.3 (a). Since the deflection of the model on the free end changes the angle of attack of the model, the actual angle of attack time histories will be different from the corresponding DyPPiR feedback measurements. This variation of angle of attack must be considered in analyzing the experimental data.

To simplify the analysis without losing the major characteristics of the problem, in the present study, we neglect the effects of the axial compression and extension of the sting, and only the structural dynamics normal to sting axis are considered in modeling the associated angle-of-attack variations. Specifically, the deflection of the model on the free end of the sting is modeled approximately by an one-dimensional spring-mass system as illustrated in Figure 2.3 (a) and (b).

In Figure 2.3 (a), m_1 and m_2 are, respectively, the mass of the model plus the aircraft side of the balance, and the mass of the sting plus the sting side of the balance. $F_n(t)$ is the normal force acting on the model and z is the deflection of the model with respect to its nominal position. The spring-mass model of the system is shown in Figure 2.3 (b) where m is the equivalent mass of the system consisting of m_1 and part of m_2. k and c_0 are the equivalent spring constant and damping coefficient, respectively.

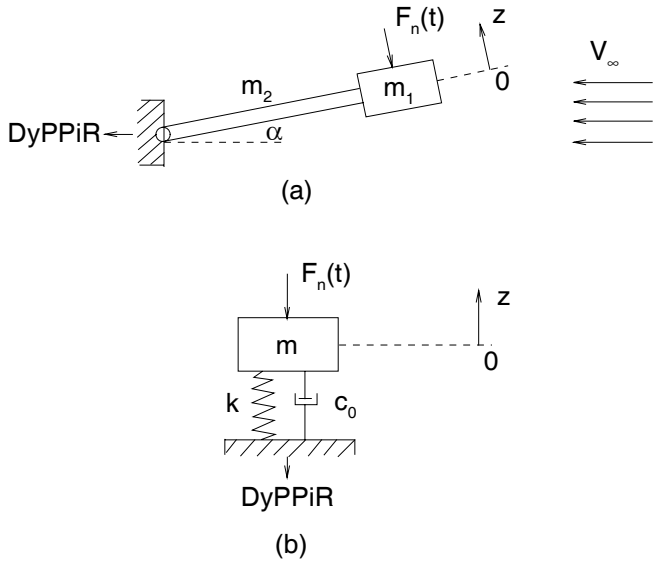

Figure 2.3: (a) Sting-model system (b) Model as a spring-mass system

Based on the model shown in Figure 2.3, the dynamic properties of the system were investigated through experimental means. We generated the free oscillations of the system by plunging the system to a new position instantly. Then we took the measurements of the balance normal force responses. The measured force in this case corresponds to the inertia force of the system due to the free oscillations, and the system equivalent weight. Figure 2.4 plots the measurements of the balance normal force responses at a sampling frequency of $f_s = 1000$ Hz.

The inertia normal force is actually the product of the normal acceleration and the equivalent mass of the system, that is, $-m\ddot{z}(t)$, where m is the equivalent mass of the system and $z(t)$ is the deflection of the center of gravity of the model at time t. Therefore the normal force time history shown in Figure 2.4 is actually the scaled time history of the acceleration of the system. We can use it to estimate the elastic modes included in the motion.

As one can see, from Figure 2.4, that the motion shows the characteristics of a second-order system except at the beginning where there are some high frequency modes showing up. But these modes damp out very rapidly, and after that the motion of the system is dominated by one second-order mode.

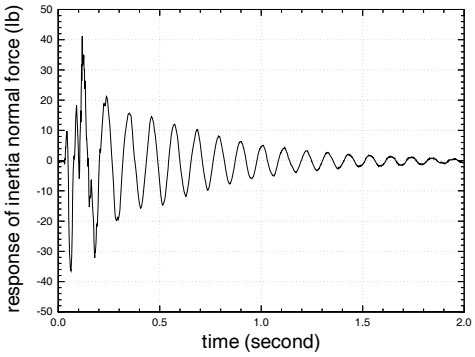

Figure 2.4: Response of inertia normal force (lb)

To confirm the above observations, we resort to the Fast Fourier Transform (FFT) algorithm to compute the Discrete Fourier Transform (DFT) of this sampled signal. We use the first 1500 samples to do DFT analysis. These 1500 samples of data represent the motion time history from $t = 0$ to $t = 1.5$ seconds since the sampling frequency for this signal is $f_s = 1000$ Hz. We divide these data into three blocks with 500 samples in each block. The first block represents the time history from t=0 to t=0.5 second, the second from t=0.501 second to t=1.0 second, and the last from t=1.001 seconds to t=1.5 seconds.

By zero-padding, we take 2048-point FFT of each block of data to investigate the frequency

components contained in corresponding block of data. Figure 2.5 shows the magnitudes of the DFT values of these three blocks of data.

From Figure 2.5, one can see that two spectrum peaks show up for 1st block of data. The dominant one is located at $f_1 = 9.28\ Hz$ and the other is at $f_2 = 23.44\ Hz$. For the 2nd and 3rd blocks of data, only one frequency component shows up at $f_1 = 9.28\ Hz$ and the frequency peak showing up in 1st block of data at $f_2 = 23.44\ Hz$ has damped out. This result is consistent to what we have observed from Figure 2.4. So the motion of this equivalent system is dominated by an elastic mode at frequency $f_1 = 9.28\ Hz$.

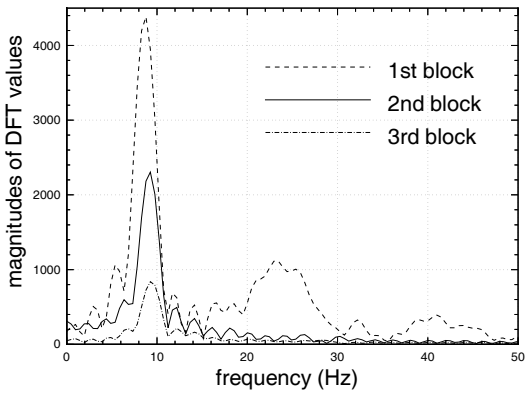

Figure 2.5: Spectra of three blocks of data

The natural frequency and damping ratio of this dominant mode can then be estimated as follows,

$$\begin{aligned} \omega_{n1} &= 2\pi f_1 \\ \zeta_1 &= \frac{1}{2\pi} ln(\frac{N_p}{N_q}) \end{aligned} \tag{2.4}$$

where N_p and N_q are two successive peak values of the balance normal force response as shown in Figure 2.4. We found from the measurements shown in Figure 2.4 that this

damping ratio is not a constant. Based on the data as shown in Figures 2.4 and 2.5, we obtained an estimate in average sense as: $\omega_n \approx 58.31$ (rad/s) and $\zeta_1 \approx 0.032$.

Thus the equivalent system as shown in Figure 2.3 (b) can then be described approximately by the following second-order linear differential equation,

$$\ddot{z}(t) + 2\zeta_1\omega_{n1}\dot{z}(t) + \omega_{n1}^2 z(t) = \frac{1}{m}[F_{n,iner}(t) + F_{n,aero}(t) - Wcos(\alpha)] \tag{2.5}$$

where $F_{n,iner}(t)$ is the normal inertia force at the center of gravity (CG) of the model due to the pre-programmed maneuvers of the DyPPiR, $F_{n,aero}(t)$ is the normal aerodynamic force and W is the equivalent weight of the system.

The general solution of this second-order system is of the following form,

$$z(t) = A_0 e^{-\zeta_1\omega_{n1}t} sin(\omega_{n1}\sqrt{1-\zeta_1^2}t + \varphi_0) + z^*(t) \tag{2.6}$$

where A_0 and φ_0 are constants determined by the initial conditions and $z^*(t)$ is the steady-state solution of Eq.(2.5) which depends on $F_{n,iner}(t)$, $F_{n,aero}(t)$ and W.

The transient term in Eq.(2.6) is of the frequency of the system, i.e., 58.31 radians/s (or 9.28 Hz) while the steady state solution $z^*(t)$ is of the same frequencies as the inputs. The properties of $z^*(t)$, however, are characterized by the frequency responses of the system. Let $G_z(s)$ be the transfer function of the system. Then its magnitude and phase responses are given by,

$$\begin{aligned} |G_z(j\omega)| &= \frac{1/\omega_{n1}^2}{\sqrt{[1-(\omega/\omega_{n1})^2]^2 + 4\zeta_1^2(\omega/\omega_{n1})^2}} \\ \angle G_z(j\omega) &= -tan^{-1}\frac{2\zeta_1(\omega/\omega_{n1})}{1-(\omega/\omega_{n1})^2} \end{aligned} \tag{2.7}$$

The frequency responses given in Eq.(2.7) are plotted in Figure 2.6 for the damping ratio $\zeta_1 = 0.01, 0.032$ and 0.1, respectively. From the plots, one can see that this system is a

resonator at the natural frequency $\omega_{n1} = 58.31$ radians/s (or 9.28 Hz). One can also see the dependence of the resonance on the damping ratio ζ_1. Any inputs with frequencies far from 9.28 Hz will be attenuated to some extent at the steady state output.

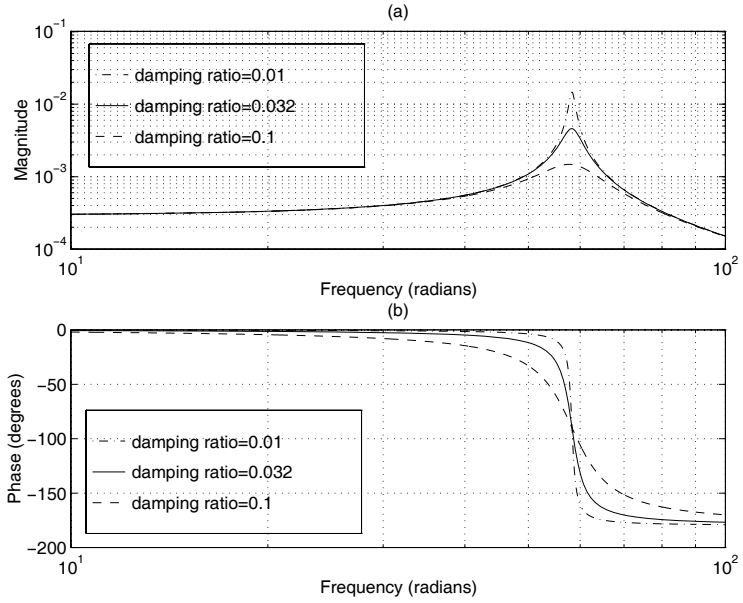

Figure 2.6: (a) Magnitude response (b) Phase response

For the oscillatory motions of current interests, the driven terms in Eq.(2.5): $F_{n,iner}(t)$, $F_{n,aero}(t)$ and $Wcos(\alpha)$, generally have the frequency components at the maneuver frequency and the frequency components at the natural frequencies of the system (9.28 Hz and 23.44 Hz). Accordingly, the steady state solution will have the same frequency components. Therefore, the solution given in Eq.(2.6) can be written as,

$$z(t) = z_s(t) + z_h(t) \tag{2.8}$$

where $z_s(t)$ is the steady state solution associated with the maneuver frequency while $z_h(t)$ includes the steady state solution associated with the system natural frequencies and the transient part, which is also of the system natural frequencies.

The variations of angle of attack $\Delta\alpha(t)$ associated with the deflection $z(t)$ can then be estimated by the relation between the slope and the deflection of a cantilever beam at the free end as,

$$\begin{aligned} \Delta\alpha(t) &= \frac{3}{2l}z(t) \\ &= \frac{3}{2l}z_s(t) + \frac{3}{2l}z_h(t) \\ &= \Delta\alpha_s(t) + \Delta\alpha_h(t) \end{aligned} \tag{2.9}$$

where l is the length of the sting, and $\Delta\alpha_s(t)$ is the variation of angle of attack associated with the maneuver frequency while $\Delta\alpha_h(t)$ is the one associated with the system natural frequency.

Thus the actual angle of attack time history in the tests can be written as,

$$\begin{aligned} \alpha(t) &= \alpha_{fdbk}(t) + \Delta\alpha(t) \\ &= \alpha_{fdbk}(t) + \Delta\alpha_s(t) + \Delta\alpha_h(t) \end{aligned} \tag{2.10}$$

where $\alpha_{fdbk}(t)$ is the angle-of-attack time histories of the pre-programmed maneuvers. For the sinusoidal oscillations in pitch, $\alpha_{fdbk}(t)$ are directly the angle of attack measurements of the DyPPiR while for the sinusoidal oscillations in plunge, $\alpha_{fdbk}(t)$ have to be obtained from the DyPPiR plunge measurements by numerical differentiation techniques according to the motion descriptions given in Eq.(2.3).

However, obtaining a good estimate of $\Delta\alpha(t)$ is a nontrivial problem because Eq.(2.5) is just an approximation to the system. The high frequency modes and the nonlinearities of the system have been neglected. However, even if we obtain an estimate of the actual angle of attack time history, we don't know the associated aerodynamic load time histories.

What we have are the balance measurements which include the aerodynamic loads and all the inertia loads due to the actual motion of the aircraft in the tests.

Although these forces and moments are not separable in time domain, they can be separable in frequency domain under certain conditions. Furthermore, as one can see, from Eq.(2.10), that if $\Delta\alpha_s(t)$ is negligibly small, the variation of the angle of attack due to elastic deformation of the sting is also separable from the angle of attack of the pre-programmed maneuvers in frequency domain. In such a case, we don't need to estimate the variations of the angle of attack due to the elastic deformation of the sting. These analyses result in the signal processing approach used in the current aerodynamic data reduction.

2.4 Digital Filter and Signal Processing Approach

For the aerodynamic system tested, the input is given by Eq.(2.10), where $\alpha_{fdbk}(t)$ can be obtained either by the direct measurements of the DyPPiR (for pitch oscillations) or by the numerical differentiation of the DyPPiR measurements (for plunge oscillations). $\Delta\alpha(t) = \Delta\alpha_s(t) + \Delta\alpha_h(t)$ are considered as input noise, caused by the elastic deformation of the sting and, presently, are not measurable. However, if $\Delta\alpha_s(t)$ is negligibly small, from the above discussions, we know that the noise term $\Delta\alpha(t)$ contains the natural frequencies of the sting while the signal $\alpha_{fdbk}(t)$ contains the frequency of the pre-programmed maneuver. In such a case, the signal $\alpha_{fdbk}(t)$ is resolvable from the noise $\Delta\alpha(t)$ in frequency domain.

The corresponding aerodynamic responses to the input are then composed of the responses to the signal $\alpha_{fdbk}(t)$ and the responses to the noise $\Delta\alpha(t)$ if a linear aerodynamics system is assumed. These responses are summed up in time domain but are resolvable in frequency domain. The question is that, currently, we don't have the pure aerodynamic response measurements. What we have are the balance readings which include the aerodynamic loads and all the inertia loads due to the actual motion of the aircraft in the tests. However,

we will show, in this section, that the inertia loads due to the pre-programmed maneuver can be eliminated by subtracting the measurements in the wind-off tests from those in the corresponding wind-on tests. What are left are the aerodynamic responses and the residual inertia loads which are dominated by the components of the natural frequencies of the sting. In such a case, we can extract the aerodynamic responses to the signal $\alpha_{fdbk}(t)$ by a digital filtering operation.

2.4.1 Analysis of Input Time Histories

First let's show that $\Delta\alpha_s(t)$ is negligibly small. The order of $\Delta\alpha_s(t)$ can be obtained by estimating the order of $z_s(t)$ according to Eq.(2.9). As we know, the $z_s(t)$ is the steady state solution of Eq.(2.5) at the maneuver frequency which is generally low. Based on the flat characteristics of the magnitude response at low frequencies as shown in Figure 2.6 (a), the upper bound of $|z_s(t)|$ can be estimated by its maximum direct current (DC) value, i.e.,

$$|z_s(t)| \leq \frac{1}{m\omega_{n1}^2}|F^s_{n,iner}(t) + F^s_{n,aero}(t) - Wcos(\alpha)|_{max} \tag{2.11}$$

where $F^s_{n,iner}(t)$ and $F^s_{n,aero}(t)$ are the normal inertia and aerodynamic forces at the maneuver frequency, respectively.

The equivalent spring constant in Figure 2.3 was obtained from the off-line test as $k = 2858$ lbs/ft, and then the equivalent mass can be estimated by,

$$m = \frac{k}{\omega_{n1}^2} = 0.84 \quad (slugs) \tag{2.12}$$

Since the balance readings for the normal force in the current wind-tunnel tests are less than 60 lbs, the corresponding upper bound of $|z_s(t)|$ is then,

$$|z_s(t)| \leq \frac{60}{k} = 0.252 \quad (inches) \tag{2.13}$$

and the corresponding upper bound of $\Delta\alpha_l(t)$ can be obtained by

$$|\Delta\alpha_s(t)| \leq (\frac{3}{2l})(0.252) = 0.656 \quad (degrees) \tag{2.14}$$

Actually, the $|\Delta\alpha_s(t)|$ in tests is much less than the bound given in Eq.(2.14) because the maximum magnitude of the inputs at the maneuver frequency as shown in Eq.(2.11) is much less than the maximum balance readings.

After neglecting $\Delta\alpha_s(t)$, the actual angle of attack time history given in Eq.(2.10) reduces to

$$\alpha(t) = \alpha_{fdbk}(t) + \Delta\alpha_h(t) \tag{2.15}$$

From Eq.(2.15), one can see that $\alpha_{fdbk}(t)$ is of the maneuver frequency while $\Delta\alpha_h(t)$ is of the natural frequency of the system. They are summed up in time domain but they are separable in frequency domain.

2.4.2 Analysis of Output Time Histories

Next, let's look at the balance measurements. Currently, the dynamic tests were conducted for both wind-on and wind-off cases for each maneuver. For wind-off tests, the aerodynamic force is assumed zero and Eq.(2.5) reduces to

$$\ddot{z}_0(t) + 2\zeta_1\omega_{n1}\dot{z}_0(t) + \omega_{n1}z_0(t) = \frac{1}{m}[F_{n,iner}(t) - Wcos(\alpha)] \tag{2.16}$$

We assume that the normal inertia forces due to the pre-programmed maneuvers are exactly the same for both wind-on and wind-off tests. Thus subtracting Eq.(2.16) from Eq.(2.5), we obtain,

$$\Delta\ddot{z}(t) + 2\zeta_1\omega_{n1}\Delta\dot{z}(t) + \omega_{n1}^2\Delta z(t) = \frac{1}{m}F_{n,aero}(t) \tag{2.17}$$

where $\Delta z(t) = z(t) - z_0(t)$.

Accordingly, we subtract the balance measurements in wind-off tests from the balance measurements in the corresponding wind-on tests. Let $F_{n,w}(t)$ and $F_{n,o}(t)$ be the balance measurements of the normal force in wind-on and wind-off tests, respectively, we have

$$\Delta F_{n,bal}(t) = F_{n,w}(t) - F_{n,o}(t) \tag{2.18}$$

We claim that this difference contains the normal aerodynamic force and the normal inertia force due to the elastic oscillation of the system driven by the aerodynamic normal force only, i.e.,

$$\Delta F_{n,bal}(t) = F_{n,aero}(t) + [-m\Delta\ddot{z}(t)] \tag{2.19}$$

Under the assumption of the linear aerodynamic system, the normal aerodynamic force responses $F_{n,aero}(t)$ in Eq.(2.19) consist of the response to the signal and the response to the noise, i.e.,

$$F_{n,aero}(t) = F^s_{n,aero}(t) + F^h_{n,aero}(t) \tag{2.20}$$

where $F^s_{n,aero}(t)$ is the response of the normal aerodynamic force to the signal $\alpha_{fdbk}(t)$ at the maneuver frequency while $F^h_{n,aero}(t)$ is the response of the normal aerodynamic force to the noise $\Delta\alpha(t)$ due to elastic deformation of sting at the frequencies of $f_1 = 9.28\ Hz$ and $f_2 = 23.44\ Hz$.

Substitute Eq.(2.20) into Eq.(2.19), we obtain,

$$\Delta F_{n,bal}(t) = F^s_{n,aero}(t) + F^h_{n,aero}(t) + [-m\Delta\ddot{z}(t)] \tag{2.21}$$

Since $-m\Delta\ddot{z}(t)$ is the normal inertia force of the system when the system is driven by the normal aerodynamic force only, it consists of the transient terms and the steady state

terms associated with $F^s_{n,aero}(t)$ and $F^h_{n,aero}(t)$, respectively. We can show that the steady state term associated with $F^s_{n,aero}(t)$ can be approximated as,

$$[-m\Delta\ddot{z}(t)]_s = \frac{1}{(f_1/f)^2 - 1} F^s_{n,aero}(t) \tag{2.22}$$

where $f_1 = 9.28$ Hz is the sting frequency and f is the frequency of $F^s_{n,aero}(t)$, that is, the maneuver frequency.

In the current wind-tunnel tests, the maximum maneuver frequency of interest is $f = 1.5$ Hz. Substituting it into Eq.(2.22), we obtain $[-m\Delta\ddot{z}(t)]_s = 0.0268\ F^s_{n,aero}(t)$, which is less than 3 percent of the driven force. Based on this analysis, this term can be neglected. Therefore we can combine the last two terms in Eq.(2.21) as one,

$$\Delta F_{n,bal}(t) = F^s_{n,aero}(t) + \Delta F_{n,h}(t) \tag{2.23}$$

where $\Delta F_{n,h}(t)$ consists of the aerodynamic component $F^h_{n,aero}(t)$ and the component of the inertia force $-m\Delta\ddot{z}(t)$ at the system natural frequencies ($f_1 = 9.28\ Hz$ and $f_2 = 23.44\ Hz$).

Similarly, we can write the expressions for the axial force and pitch moment as,

$$\begin{aligned} \Delta F_{x,bal}(t) &= F^s_{x,aero}(t) + \Delta F_{x,h}(t) \\ \Delta M_{bal}(t) &= M^s_{aero}(t) + \Delta M_h(t) \end{aligned} \tag{2.24}$$

where $F^s_{x,aero}(t)$ and $M^s_{aero}(t)$ are associated with $\alpha_{fdbk}(t)$ while $\Delta F_{x,h}(t)$ and $\Delta M_h(t)$ are those components associated with the system natural frequencies.

Thus the balance data are classified into two parts in Eqs.(2.23) and (2.24). One contains the frequency of the pre-programmed maneuver which is the aerodynamic response to the signal $\alpha_{fdbk}(t)$, and the other contains the natural frequencies of the sting which is the aerodynamic response to the noise $\Delta\alpha(t)$ and some residual inertia loads. These two parts are added up in time domain but they are separable in frequency domain because the

frequency f of the pre-programmed maneuver is significantly less than the system natural frequency $f_1 = 9.28\ Hz$. In such a case, we can apply a low-pass filter to balance data $\Delta F_{n,bal}(t)$, $\Delta F_{x,bal}(t)$, and $\Delta M_{bal}(t)$ to extract the corresponding aerodynamic components $F^s_{n,aero}(t)$, $F^s_{x,aero}(t)$ and $M^s_{aero}(t)$, respectively, which are exactly the responses to the angle of attack time histories $\alpha_{fdbk}(t)$ measured by the DyPPiR.

2.4.3 Digital Filter and Signal Processing

The above discussions were conducted in continuous time domain for convenience of the statement of the arguments. However, all the wind-tunnel measurements are available in discrete time domain with a certain sampling frequency f_s. For current wind-tunnel tests, the total number of samples taken in the experiment for each maneuver is fixed at N=4096 while the sampling frequency f_s is chosen to be different from maneuver to maneuver. The discrete time versions of Eqs.(2.23) and (2.24) are,

$$\begin{aligned} \Delta F_{n,bal}(n) &= F^s_{n,aero}(n) + \Delta F_{n,h}(n) \\ \Delta F_{x,bal}(n) &= F^s_{x,aero}(n) + \Delta F_{x,h}(n) \\ \Delta M_{bal}(n) &= M^s_{aero}(n) + \Delta M_h(n) \end{aligned} \tag{2.25}$$

corresponding to the following angle of attack sequence,

$$\alpha(n) = \alpha_{fdbk}(n) + \Delta\alpha_h(n) \tag{2.26}$$

which are associated with the following time instants,

$$t_n = nT_s, \quad n = 0, 1, 2, ..., N-1 \tag{2.27}$$

where $T_s = 1/f_s$ is the sampling period of the data.

With the expressions as shown in Eq.(2.25), we can design a digital low-pass filter which has the following ideal frequency response as,

$$H(e^{j\omega}) = \begin{cases} 1, & |\omega| \leq \omega_c \\ 0, & \omega_c < |\omega| \leq \pi \end{cases} \tag{2.28}$$

where $\omega = 2\pi f/f_s$ is the frequency normalized by the sampling rate f_s and $\omega_c = 2\pi f_c/f_s$ is normalized cut-off frequency.

Thus, the filter can eliminate all the frequency components beyond the cut-off frequency $\omega_c = 2\pi f_c/f_s$. Therefore, by properly choosing the cut-off frequency f_c, we can use the filter to extract the aerodynamic components $F^s_{n,aero}(n)$, $F^s_{x,aero}(n)$ and $M^s_{aero}(n)$ from the corresponding balance data $\Delta F_{n,bal}(n)$, $\Delta F_{x,bal}(n)$ and $\Delta M_{bal}(n)$, respectively. In frequency domain, this filtering operation can be expressed as,

$$\begin{aligned} F^s_{n,aero}(e^{j\omega}) &= H(e^{j\omega})\Delta F_{n,bal}(e^{j\omega}) \\ F^s_{x,aero}(e^{j\omega}) &= H(e^{j\omega})\Delta F_{x,bal}(e^{j\omega}) \\ M^s_{aero}(e^{j\omega}) &= H(e^{j\omega})\Delta M_{bal}(e^{j\omega}) \end{aligned} \tag{2.29}$$

where argument $e^{j\omega}$ in parenthesis implies the Discrete-Time Fourier Transforms (DTFT) of the corresponding data.

In the time domain, the responses of the aerodynamic forces and moment to the angle of attack time histories $\alpha_{fdbk}(n)$ can be obtained by taking inverse DTFT of Eq.(2.29), resulting the following convolutions,

$$
\begin{aligned}
F^s_{n,aero}(n) &= h(n) \otimes \Delta F_{n,bal}(n) \\
&= \sum_{k=0}^{M} h(k) \Delta F_{n,bal}(n-k) \\
F^s_{x,aero}(n) &= h(n) \otimes \Delta F_{x,bal}(n) \\
&= \sum_{k=0}^{M} h(k) \Delta F_{x,bal}(n-k) \\
M^s_{aero}(n) &= h(n) \otimes \Delta M_{bal}(n) \\
&= \sum_{k=0}^{M} h(k) \Delta M_{bal}(n-k)
\end{aligned}
\tag{2.30}
$$

where $h(n)$ is the impulse response of the filter and M is the order of $h(n)$.

Next we need to design the digital lowpass filter whose frequency response approximates the ideal one as given in Eq.(2.28). We are going to design general linear-phase Finite Impulse Response (FIR) filters to process the data since the linear-phase characteristics guarantee no phase distortion on any signals passing through.

There are several techniques available to design linear-phase FIR filters, such as window based techniques, frequency sampling techniques and optimal designs. However, whatever techniques we use, the digital filters have to be designed in the normalized frequency domain $\omega = 2\pi f/f_s$. As we mentioned previously, for the current wind-tunnel tests, the total number of samples taken in the experiments is fixed at N=4096 while the sampling rate f_s is different from maneuver to maneuver. We need to convert the sampling rate to the same level without losing the information of interest in the data. On the other hand, the sampling rates used in the data acquisition are generally much higher than the frequency band of interest. According to the Nyquist sampling theorem, we could reduce the sampling rate by a fair amount since the minimum rate needed is the Nyquist rate, that is, two times the bandwidth of the frequency band of interest. In such a case, the efficient design of the digital filters can generally be obtained at a lower rate. Therefore we need to develop

techniques to convert the sampling rate in digital domain before we can start to design the digital filters to process the wind-tunnel measurements.

2.5 Sampling Rate Conversion

The process of sampling rate conversion in the digital domain can be viewed as a linear filtering operation, as illustrated in Figure 2.7. We are given the input signal $x(n)$, sampled at the rate $F_x = 1/T_x$, and wish to compute the output signal $y(m)$ with a new sampling rate $F_y = 1/T_y$, where T_x and T_y are the corresponding sampling periods. We will assume in present treatment that the ratio of sampling periods of $y(m)$ and $x(n)$ can be expressed as rational fraction, i.e.,

$$\frac{T_y}{T_x} = \frac{F_x}{F_y} = \frac{D}{L} \tag{2.31}$$

where D and L are integers. We will show that the linear filter is characterized by a time-variant impulse response, denoted as $h(n, m)$. Hence the input $x(n)$ and output $y(m)$ are related by the convolution summation for time-variant systems.

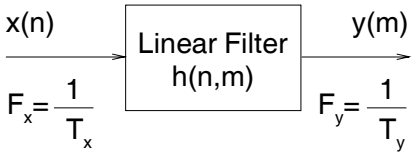

Figure 2.7: Basic process of digital sampling rate conversion

The sampling rate conversion process can also be understood from the point of view of digital resampling of the same analog signal. Let $x(t)$ be the analog signal that is sampled

at the first rate F_x to generate $x(n)$. The goal of rate conversion is to obtain another sequence $y(m)$ directly from $x(n)$, which is equal to the sampled values of $x(t)$ at a second rate F_y.

Before considering the general case of sampling rate conversion, we shall study the structure and properties of systems that perform two special cases of sampling rate conversion. One is the case of sampling rate reduction by an integer D, namely decimation by factor D. The other is the case of sampling rate increase by an integer L, namely interpolation by factor L.

2.5.1 Decimation by an Integer Factor D

Let us assume that the signal $x(n)$ with spectrum $X(e^{j\omega})$ is to be downsampled by an integer factor D, i.e., the new sampling rate is,

$$F_y = \frac{F_x}{D} \tag{2.32}$$

The spectrum $X(e^{j\omega})$ is assumed to be nonzero in the frequency interval $|\omega| \leq \pi$, or equivalently, $|f| \leq F_x/2$, where $\omega = 2\pi f/F_x$.

We know that if we reduce the sampling rate simply by selecting every Dth value of $x(n)$, the resulting signal will be an aliased version of $x(n)$, with folding frequency of $F_x/2D$. To avoid aliasing, we must first reduce the bandwidth of $x(n)$ to $\omega_{max} = \pi/D$, or equivalently, $F_{max} = F_x/2D$. Then we may downsample by D and thus avoid aliasing.

The decimation process is illustrated in Figure 2.8. The input sequence $x(n)$ is passed through a lowpass filter, characterized by the unit pulse response $h(n)$ which has frequency response $H_D(e^{j\omega})$, ideally satisfying the condition,

$$H_D(e^{j\omega}) = \begin{cases} 1, & |\omega| \leq \pi/D \\ 0, & otherwise. \end{cases} \tag{2.33}$$

Thus the filter eliminates the spectrum of $X(e^{j\omega})$ in the range $\pi/D < \omega < \pi$. Of course, the implication is that only the frequency components of $x(n)$ in the range $|\omega| \leq \pi/D$ are of interest in the further processing of the signal.

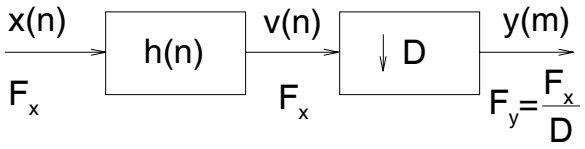

Figure 2.8: Decimation by a factor D

The output of the filter is a sequence $v(n)$ which is given by the convolution of input sequence $x(n)$ with unit pulse response of the filter $h(n)$,

$$v(n) = \sum_{k=0}^{\infty} h(k)x(n-k) \tag{2.34}$$

Then $v(n)$ is downsampled by the factor D to produce $y(m)$,

$$\begin{aligned} y(m) &= v(mD) \\ &= \sum_{k=0}^{\infty} h(k)x(mD-k) \end{aligned} \tag{2.35}$$

The frequency-domain characteristics of the output sequence $y(m)$ can be obtained by relating the spectrum of $y(m)$ to the spectrum of the input sequence $x(n)$ through the frequency response of the filter $H_D(e^{j\omega})$ as,

$$Y(e^{j\omega'}) = \frac{1}{D}\sum_{k=0}^{D-1} H_D(\frac{\omega' - 2\pi k}{D})X(\frac{\omega' - 2\pi k}{D}) \tag{2.36}$$

where ω' is normalized frequency relative to new sampling rate $F_y = F_x/D$, i.e.,

$$\omega' = 2\pi\frac{f}{F_y} = 2\pi\frac{f}{F_x}D = \omega D \tag{2.37}$$

The purpose of the low-pass filter $H_D(e^{j\omega})$ is to sufficiently filter $x(n)$ so that its components above the frequency $\omega = \pi/D$ are negligible. This result implies that all terms for $k \neq 0$ in Eq.(2.36) are removed and, consequently, all but the first term in Eq.(2.36) vanish. Hence,

$$Y(e^{j\omega'}) = \frac{1}{D} X(\frac{\omega'}{D}), \qquad for \quad |\omega'| \leq \pi \tag{2.38}$$

The spectra for the sequences $x(n), v(n)$, and $y(m)$ are illustrated in Figure 2.9.

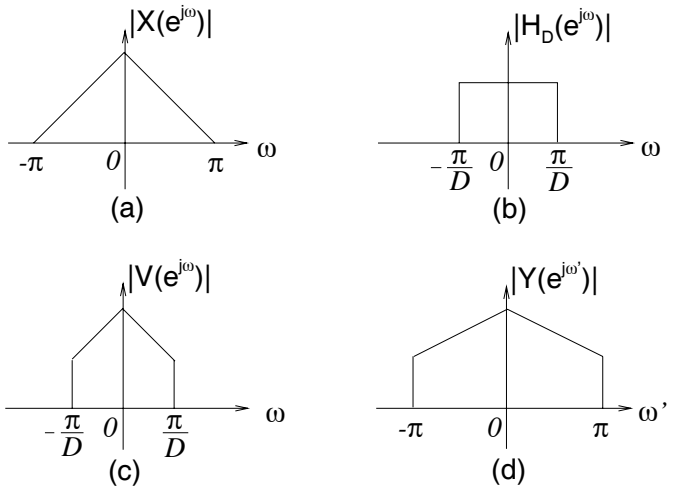

Figure 2.9: (a) spectrum of $x(n)$. (b) ideal response of filter. (c) spectrum of $v(n)$. (d) spectrum of $y(m)$.

2.5.2 Interpolation by an Integer Factor L

Assume that the signal $x(n)$ is to be upsampled by an integer factor L to produce signal $y(m)$ at sampling rate F_y,

$$F_y = LF_x \tag{2.39}$$

This process of increasing the sampling rate by L implies that we must interpolate $L-1$ new sample values between each pair of sample values of $x(n)$.

Let $w(m)$ denote a sequence at rate F_y, which is obtained from $x(n)$ by adding $L-1$ zeros between successive values of $x(n)$,

$$w(m) = \begin{cases} x(m/L), \ m = 0, \ \pm L, \ \pm 2L, \ ..., \\ 0, \qquad otherwise. \end{cases} \tag{2.40}$$

and its sampling rate is identical to the rate of $y(m)$. This sequence has a z-transform,

$$\begin{aligned} W(z) &= \sum_{m=0}^{\infty} w(m) z^{-m} \\ &= \sum_{m=0}^{\infty} x(m) z^{-mL} \\ &= X(z^L) \end{aligned} \tag{2.41}$$

Evaluating $W(z)$ on the unit circle, gives the spectrum of $w(m)$ expressed in terms of the spectrum of input signal $x(n)$,

$$W(e^{j\omega'}) = X(e^{j\omega' L}) \tag{2.42}$$

where ω' is normalized frequency relative to new sampling rate $F_y = F_x L$, i.e.,

$$\omega' = 2\pi \frac{f}{F_y} = 2\pi \frac{f}{F_x L} = \frac{\omega}{L} \tag{2.43}$$

Based on Eq.(2.42), the spectra $X(e^{j\omega})$ and $W(e^{j\omega'})$ are illustrated in Figure 2.10. We observe that the sampling rate increase, obtained by the addition of $L-1$ zero samples between successive values of $x(n)$, results in a signal whose spectrum $W(e^{j\omega'})$ is an L-fold periodic repetition of the input signal spectrum $X(e^{j\omega})$.

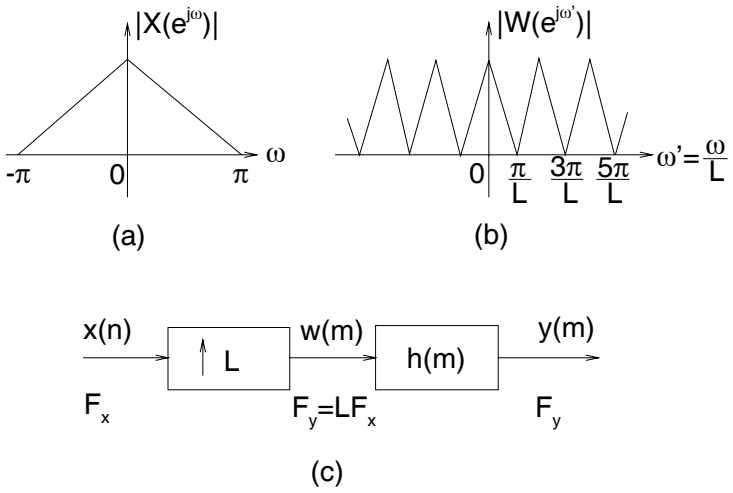

Figure 2.10: (a) spectrum of $x(n)$. (b) spectrum of $w(m)$. (c) Interpolation by a factor L

Since only the frequency components of $x(n)$ in the range $0 \leq \omega' \leq \pi/L$ are of interest, the unwanted images of $X(e^{j\omega})$ above $\omega' = \pi/L$ should be rejected by passing the sequence $w(m)$ through a low-pass filter with frequency response $H_L(e^{j\omega'})$ that approximates the ideal characteristic,

$$H_L(e^{j\omega'}) = \begin{cases} G, \ |\omega'| \leq \pi/L; \\ 0, \ otherwise. \end{cases} \tag{2.44}$$

where G is a scale factor required to normalize the output sequence $y(m)$. Consequently, the output spectrum is

$$\begin{aligned} Y(e^{j\omega'}) &= H_L(e^{j\omega' L})X(e^{j\omega' L}) \\ &= \begin{cases} GX(e^{j\omega' L}), & |\omega'| \le \pi/L; \\ 0, & otherwise. \end{cases} \end{aligned} \tag{2.45}$$

The scale factor G is selected to ensure that the amplitude of $y(m)$ is correct, i.e., we need

$$y(m) = x(m/L), \quad for\ m = 0,\ \pm L,\ \pm 2L, ... \tag{2.46}$$

For mathematical convenience, we examine the zeroth sample of the sequences.

$$\begin{aligned} y(0) &= \frac{1}{2\pi}\int_{-\pi}^{\pi} Y(e^{j\omega'})d\omega' \\ &= \frac{1}{2\pi}\int_{-\pi}^{\pi} H_L(e^{j\omega'})X(e^{j\omega' L})d\omega' \\ &= \frac{G}{2\pi}\int_{-\pi/L}^{\pi/L} X(e^{j\omega' L})d\omega' \\ &= \frac{G}{L}\frac{1}{2\pi}\int_{-\pi}^{\pi} X(e^{j\omega})d\omega \\ &= \frac{G}{L}x(0) \end{aligned} \tag{2.47}$$

Therefore, a gain $G = L$ is required to match the amplitude of the envelopes of the signals $y(m)$ and $x(n)$.

Therefore, a gain $G = L$ is required to match the amplitude of the envelopes of the signals $y(m)$ and $x(n)$.

Finally, we indicate that the output sequence $y(m)$ can be expressed as a convolution of the sequence $w(m)$ with the unit pulse response $h(n)$ of the low-pass filter.

$$y(m) = \sum_{k=0}^{\infty} h(m-k)w(k) \tag{2.48}$$

Since $w(k) = 0$ except at multiples of L, where $w(kL) = x(k)$, Eq.(2.48) becomes

$$y(m) = \sum_{k=0}^{\infty} h(m-kL)x(k) \tag{2.49}$$

2.5.3 Sampling Rate Conversion by a Rational Factor L/D

Having discussed the special cases of decimation and interpolation, we now consider the general case of sampling rate conversion by a rational factor L/D. Basically, this conversion can be achieved by first performing interpolation by factor L and then decimating the output of the interpolator by factor D. In other words, a sampling rate conversion by the rational factor L/D is accomplished by cascading an interpolator with a decimator, as illustrated in Figure 2.11 (a).

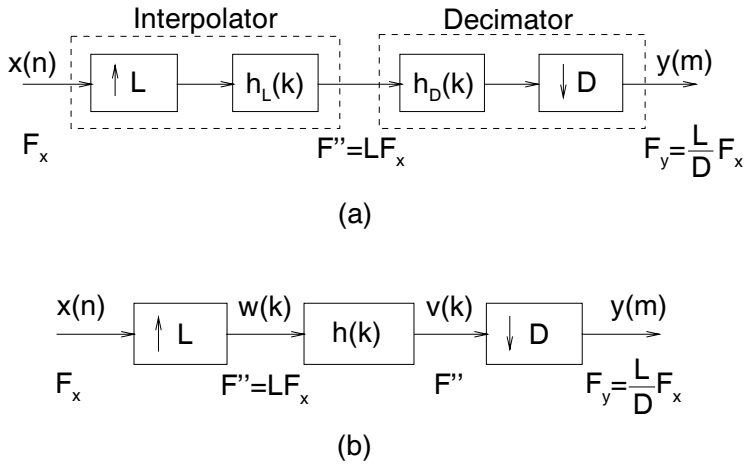

Figure 2.11: (a) Cascade of an interpolator and a decimator (b) Sampling rate conversion by a factor L/D

We emphasize that the importance of performing the interpolation first and the decimation second, is to preserve the desired special characteristics of $x(n)$. Furthermore, with the cascade configuration illustrated in Figure 2.11 (a), the two filters $h_L(k)$ and $h_D(k)$ are operating in cascade at the same sampling rate LF_x and hence can be combined into one single lowpass filter with unit pulse response $h(k)$ as shown in Figure 2.11 (b). Since this

digital filter must serve the purpose of both the interpolation and decimation operations described in the previous sections, its frequency response must ideally possess the frequency response characteristic,

$$H(e^{j\omega''}) = \begin{cases} L, \ |\omega''| \leq min(\pi/L, \pi/D); \\ 0, \ otherwise. \end{cases} \tag{2.50}$$

where

$$\omega'' = 2\pi \frac{f}{F''} = 2\pi \frac{f}{LF_x} \tag{2.51}$$

In the time domain, the output of the upsampler is the sequence

$$w(k) = \begin{cases} x(k/L), \ k = 0, \ \pm L, \ \pm 2L, \ ... \\ 0, \qquad otherwise. \end{cases} \tag{2.52}$$

and the output of the linear time-invariant filter is

$$\begin{aligned} v(k) &= \sum_{r=0}^{\infty} h(k-r)w(r) \\ &= \sum_{r=0}^{\infty} h(k-rL)x(r) \end{aligned} \tag{2.53}$$

Finally, the output of the sampling rate converter is the sequence $y(m)$, which is obtained by downsampling the sequence $v(k)$ by a factor of D.

$$\begin{aligned} y(m) &= v(mD) \\ &= \sum_{r=0}^{\infty} h(mD - rL)x(r) \end{aligned} \tag{2.54}$$

Similarly, the frequency-domain relationships can be obtained by combining the results of the interpolation and decimation processes. Thus the spectrum at the output of the lowpass filter with unit pulse response $h(k)$ is

$$\begin{aligned} V(e^{j\omega''}) &= H(e^{j\omega''})X(e^{j\omega''L}) \\ &= \begin{cases} LX(e^{j\omega''L}), \ |\omega''| \leq min(\pi/L, \pi/D); \\ 0, \qquad\qquad otherwise. \end{cases} \end{aligned} \tag{2.55}$$

The spectrum of the output sequence $y(m)$, obtained by decimating the sequence $v(k)$ by a factor D, is

$$Y(e^{j\omega'}) = \frac{1}{D}\sum_{l=0}^{D-1} V(\frac{\omega' - 2\pi l}{D}) \tag{2.56}$$

where $\omega' = D\omega'' = 2\pi(fD)/(F_x L)$ is normalized frequency relative to new sampling rate $F_y = F_x(L/D)$.

Since the lowpass filter prevents aliasing as implied by Eq.(2.56), the spectrum of the output sequence $y(m)$ reduces to

$$Y(e^{j\omega'}) = \begin{cases} \frac{L}{D}X(e^{j\omega' L/D}), & |\omega'| \leq min(\pi, \frac{\pi D}{L}) \\ 0, & otherwise. \end{cases} \tag{2.57}$$

Thus far, we have developed the general system for sampling rate conversion of signals by arbitrary rational factors L/D. We will implement the above sampling rate conversion system to resample the unsteady wind-tunnel data at the appropriate rates for further processing. Further information about the theory of multirate signal processing, one can refer to Ref.[36].

2.6 Linear-phase FIR Lowpass Filter Designs

As indicated in the discussion above, sampling rate conversion by a factor L/D can be achieved by first upsampling the input signal by factor L, followed by linear filtering of the resulting sequence to eliminate the unwanted images, and finally, by downsampling the filtered signal by factor D. Thus we need to design the linear filter for this sampling conversion system.

Furthermore, after resampling the wind-tunnel measurements using the above system, we need to design lowpass filters with different specifications for further processing of the resampled data to extract the aerodynamic forces and moment responses to the angle of attack time histories $\alpha_{fdbk}(n)$, as discussed in **Section 2.4.** In this section, we consider the design of general linear-phase FIR lowpass filters.

The frequency range of a practical lowpass filter is generally classified as three bands of interest as follows,

$$\begin{aligned} &0 \leq \omega \leq \omega_p, \qquad Passband \\ &\omega_p < \omega < \omega_s, \qquad Transition\ band \\ &\omega_s \leq \omega \leq \pi, \qquad Stopband \end{aligned} \tag{2.58}$$

where ω_p and ω_s are edge frequencies for passband and stopband, respectively.

Let $H(e^{j\omega})$ be the frequency response of the lowpass filter to be designed. The specifications of the design are generally of the form,

$$\begin{aligned} &1 - \delta_p \leq |H(e^{j\omega})| \leq 1 + \delta_p,\ |\omega| \leq \omega_p \\ &|H(e^{j\omega})| \leq \delta_s,\ \omega_s < |\omega| \leq \pi \end{aligned} \tag{2.59}$$

where δ_p is the passband ripple while δ_s is the stopband attenuation. The transition band

is defined as a "don't-care" region.

The specifications given in Eq.(2.59) are illustrated in Figure 2.12.

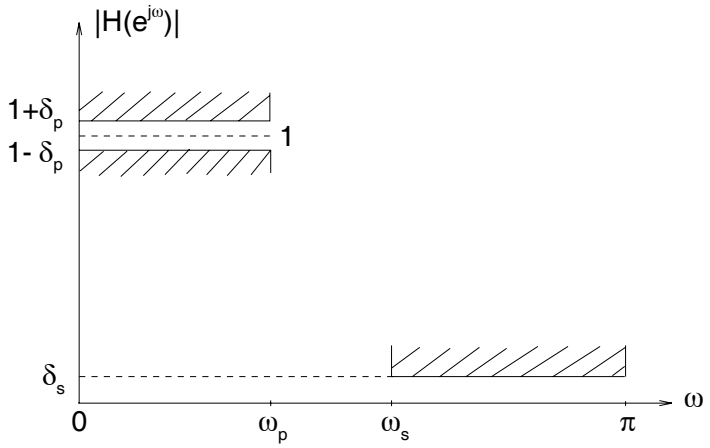

Figure 2.12: Specifications for a practical lowpass filter

We are required to design general linear-phase FIR filter to meet the specifications as shown in Figure 2.12 and the linear-phase characteristics guarantee no phase distortion on the signals passing through the filter, except for a pure delay.

There are a number of filter design procedures which apply to the design of the lowpass filters, such as window designs, frequency sampling designs and optimal designs. We will not discuss all of these methods since they are well documented in several references[36−38]. Here we are going to use the equiripple design based on Chebyshev approximation methods. The filters designed by this technique are optimal in the sense that the weighted peak approximation error in the frequency domain over the frequency range of interest is minimized. Although a closed-form design technique is not available for these filters, an elegant and powerful iterative algorithm: the Remez exchange algorithm, does provide the

basis for efficient design methods. Since CAD software for Remez exchange algorithm is readily available in MATLAB and elsewhere to do the equiripple design[38], we will not be concerned with the design details.

Here we show a design example. Suppose that we want to design a linear-phase FIR filter meeting the following specifications,

$$\begin{aligned} &\delta_p \leq 0.005, \quad \delta_s \leq 0.001 \\ &\omega_p = 0.1\pi, \quad \omega_s = 0.1667\pi \end{aligned} \tag{2.60}$$

The specifications in Eq.(2.60) can be stated alternatively in terms of dB, that is, the passband ripple is less than 0.044 dB while stopband attenuation is larger than 60 dB.

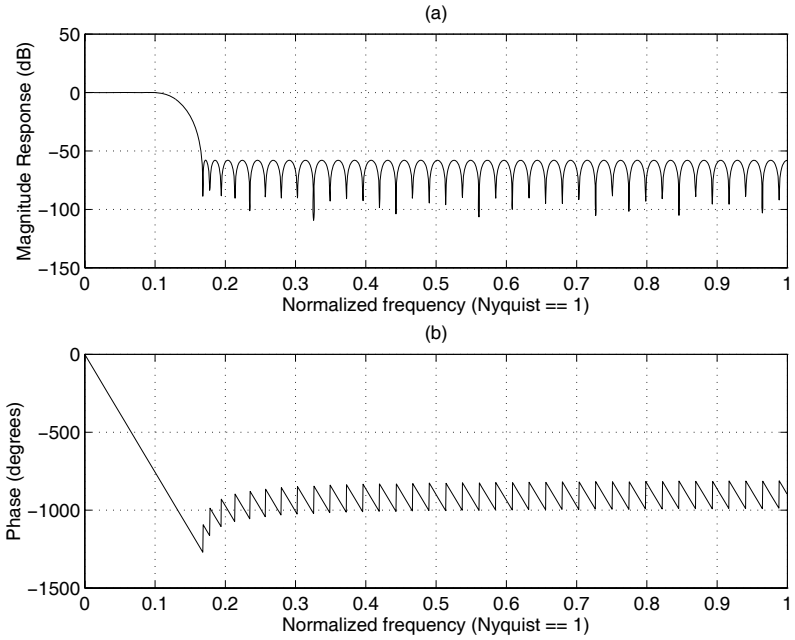

Figure 2.13: Equiripple design for a practical lowpass filter

Using Remez exchange algorithm in MATLAB, we obtain the filter of the lowest order that meets the above specifications. The order of this filter is $M = 84$. Its magnitude and phase responses are plotted in Figure 2.13 (a) and (b), respectively.

From Figure 2.13, one can see that in passband: $0 \leq \omega \leq 0.1\pi$, the ripple is less than 0.044 dB and phase is indeed linear, while in stopband: $0.1667\pi \leq \omega \leq \pi$, the attenuation is at least 60 dB. The specifications are satisfied and the design is indeed equiripple. The phase response of the filter in passband can be proved to be,

$$\begin{aligned} \angle H(e^{j\omega}) &= -\frac{M}{2}\omega \\ &= -42\omega \end{aligned} \tag{2.61}$$

The linear-phase characteristic implies that all the frequency components of an input sequence are similarly delayed in the output sequence. The filter has no phase distortion on the input sequence. We can see this characteristic by considering a single sinusoidal input sequence with frequency ω_0 in passband,

$$x(n) = sin(n\omega_0), \quad n = 0, 1, 2, ... \tag{2.62}$$

The corresponding steady-state output sequence of the filter can be written as,

$$y(n) = |H(e^{j\omega_0})|sin[n\omega_0 + \angle H(e^{j\omega_0})] \tag{2.63}$$

Noting that $|H(e^{j\omega_0})| \approx 1$ in passband and substituting the linear-phase characteristic in Eq.(2.61) into Eq.(2.63), we have,

$$\begin{aligned} y(n) &= sin(n\omega_0 - \frac{M}{2}\omega_0) \\ &= sin(n - 42)\omega_0 \end{aligned} \tag{2.64}$$

From Eqs.(2.62) and (2.64), one can see that the output sequence is exactly same as the input sequence, except for a pure delay by $M/2 = 42$ samples.

The impulse response $h(n)$ of the filter is plotted in Figure 2.14 from which one can see the even symmetry in the $h(n)$ about its midpoint $M/2 = 42$. It is this even symmetric characteristic that ensures linear phase. The response $y(n)$ of the filter to any input sequence $x(n)$ can be obtained by computing the convolution of the $h(n)$ with the input $x(n)$ as follows,

$$\begin{aligned} y(n) &= h(n) \otimes x(n) \\ &= \sum_{k=0}^{M} h(k)x(n-k) \end{aligned} \tag{2.65}$$

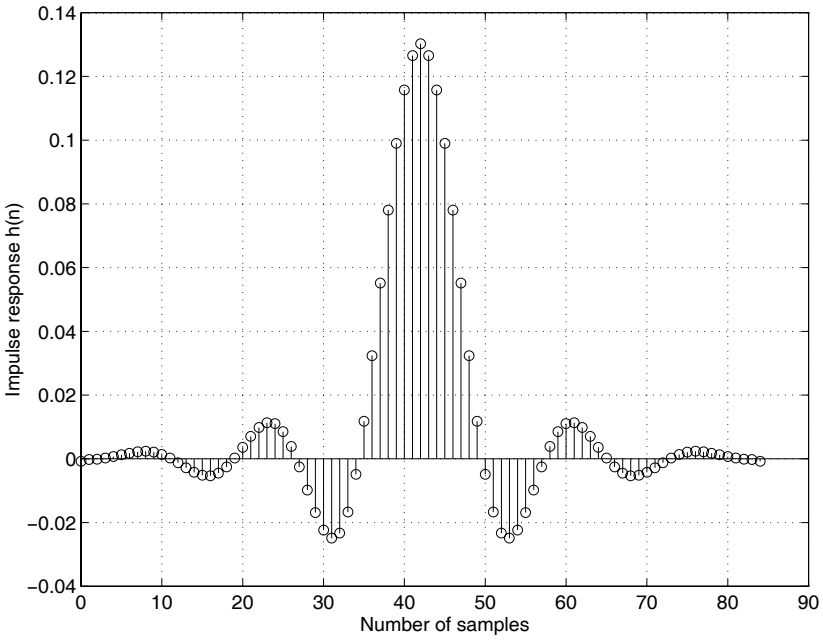

Figure 2.14: Impulse response of the lowpass filter

2.7 Aerodynamic Data Processing

After the development of multirate system for sampling rate conversion and discussion of the linear-phase FIR filter design, we are ready to process the wind-tunnel data based on the analysis in **Section 2.3**.

First, we need to obtain the aerodynamic data: $\Delta F_{n,bal}(n)$, $\Delta F_{x,bal}(n)$, and $\Delta M_{bal}(n)$ by subtracting the balance measurements in wind-off test from those in corresponding wind-on test. Based on the analyses indicated in Eq.(2.30), these data contain the aerodynamic forces and moment responses to the angle of attack time histories $\alpha_{fdbk}(n)$, at the maneuver frequency, and aerodynamic responses to the noise $\Delta\alpha(t)$ and some residual inertia loads at the natural frequencies of the sting. Digital lowpass filters are needed to eliminate these extra responses at the natural frequencies of the sting. Before designing such filters, we need to convert the sampling rate to the desired level for all the maneuvers without losing the information of interest. In this case, we can do more efficient designs of the digital filters at low sampling rates. In the following, we are going to illustrate the procedures of the data reduction techniques developed above for a oscillatory pitch maneuver and also a oscillatory plunge maneuver. The processings for the balance readings are similar except that for the plunge maneuvers, we have to obtain the input signal $\alpha_{fdbk}(n)$ from the DyPPiR plunge measurements by numerical differentiation while for the pitch maneuvers, the $\alpha_{fdbk}(n)$ are directly measured by the DyPPiR.

2.7.1 Data Processing for an Oscillatory Pitch Maneuver

As an illustration, let's look at the experimental data of sinusoidal pitch oscillation about zero mean angle of attack with amplitude of 5 degrees and frequency of 0.5 Hz. The tunnel speed is 95 feet/s for this maneuver.

2.7.1.1 Resampling of the Data

The sampling rate used in the data acquisition for this maneuver is $f_s = 200\ Hz$, which implies a 100 Hz frequency bandwidth of interest. Figure 2.15 (a), (c), and (e) plot the time histories of the normal force $\Delta F_{n,bal}(n)$, the axial force $\Delta F_{x,bal}(n)$, and the pitch moment $\Delta M_{bal}(n)$, respectively. They were obtained by subtracting the balance measurements in wind-off test from those in wind-on test for this sinusoidal pitch oscillation maneuver. As one can see that these signals are very noisy in time domain. In order to identify the frequency components contained in the data, we compute the DFT values of these signals by the FFT algorithm. Figure 2.15 (b), (d), and (f) plot the DFT values of $\Delta F_{n,bal}(n)$, $\Delta F_{x,bal}(n)$, and $\Delta M_{bal}(n)$, respectively.

From Figure 2.15 (a) and (b), one can see that the normal force $\Delta F_{n,bal}(n)$ contains a frequency peak at the maneuver frequency of 0.5 Hz, and two frequency peaks at around the sting frequencies of 9.28 Hz and 23.44 Hz, respectively. This result is consistent with the previous analyses of the dynamic oscillatory tests.

From Figure 2.15 (c) and (d), one can see that the axial force contains some components with frequencies around 0.5 Hz and several components with frequencies from 50 Hz to 70 Hz. The low frequency components are the responses to the maneuver of the model and the high frequency components are associated with the structural dynamics of the sting in the axial direction.

From Figure 2.15 (e) and (f), one can see that the pitch moment contains frequency peaks at the maneuver frequency, and at the sting frequencies of 9.28 Hz and 23.44 Hz. Besides these frequency components, one can also see several frequency peaks with frequencies from 30 Hz to 50 Hz. These high frequency components are possibly associated with the balance frequencies or some other sources that we would not like to investigate in current research efforts. These high frequency components are considered as noise that is to be rejected by digital filter operations.

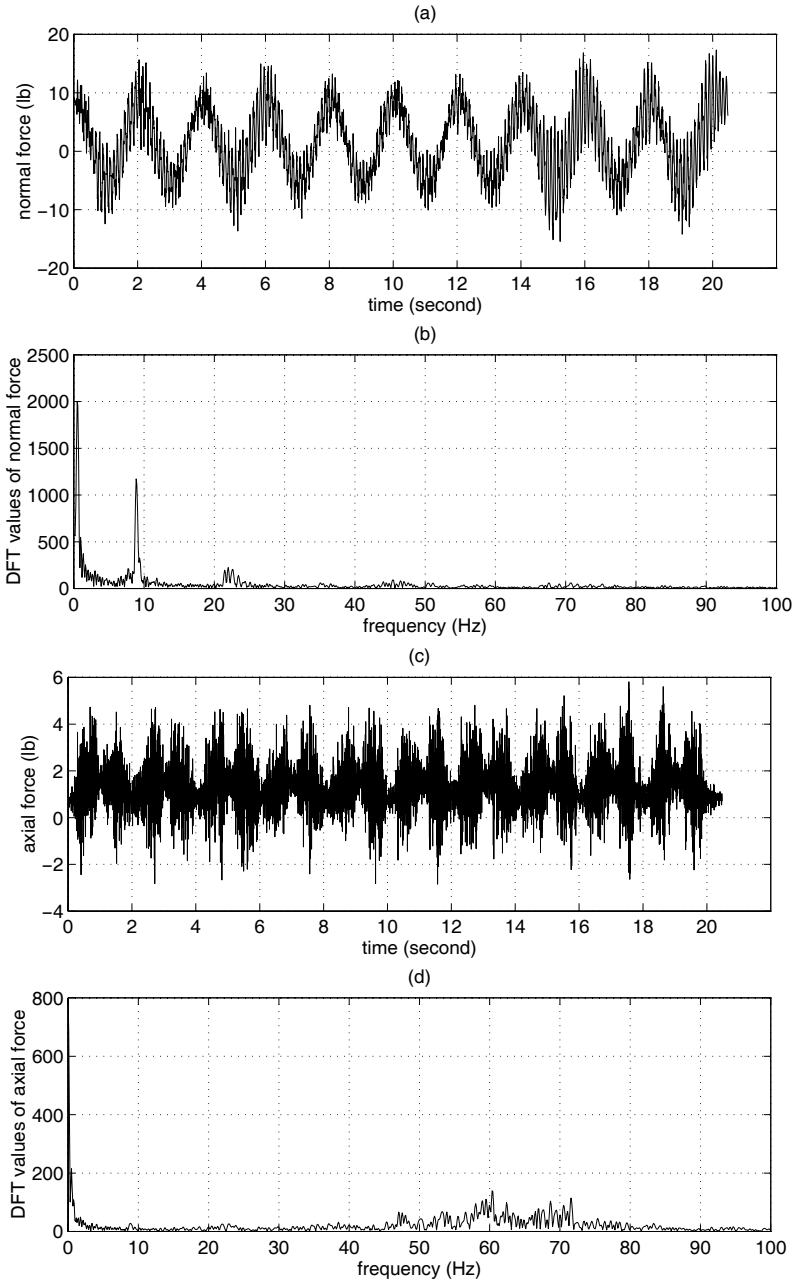
(a)
normal force (lb)
time (second)
(b)
DFT values of normal force
frequency (Hz)
(c)
axial force (lb)
time (second)
(d)
DFT values of axial force
frequency (Hz)

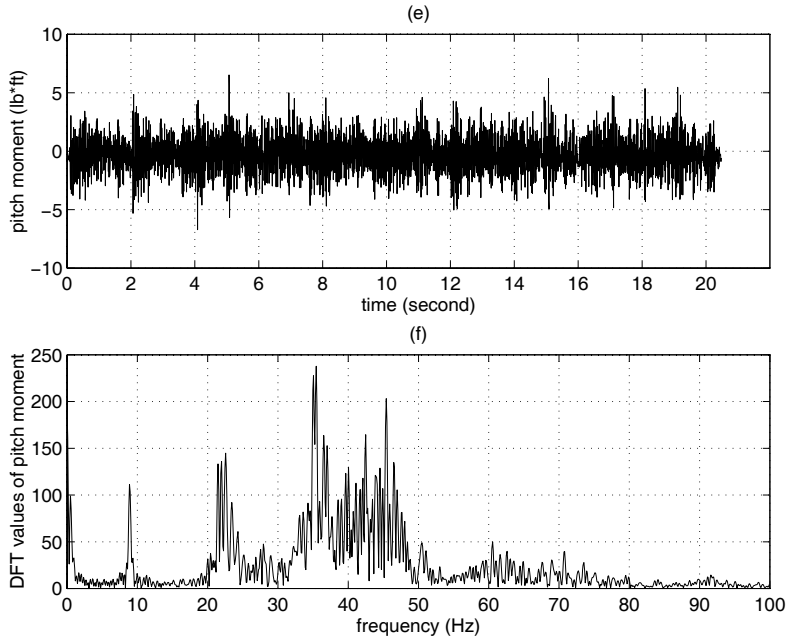

Figure 2.15: (a) Normal force time history (b) DFT values of normal force (c) Axial force time history (d) DFT values of axial force (e) Pitch moment time history (f) DFT values of pitch moment

First we convert the sampling rate of the above measured data from the $f_s = 200\ Hz$ used in the data acquisition for this maneuver to $f_s' = 30\ Hz$. The new sampling rate means that we want to reduce the frequency bandwidth of interest from $f_s/2 = 100\ Hz$ to $f_s'/2 = 15\ Hz$. The reason why $15\ Hz$ is chosen as new bandwidth of interest is that we want to keep all the information contained in the balance data at the maneuver frequency and at the natural frequency of dominant mode of the sting. Any information with frequencies higher than $15\ Hz$ is treated as noise and is to be rejected in the resampling process. The sampling rate conversion can be achieved by first performing interpolation by factor $L = 3$ and then decimating the output of the interpolator by factor $D = 20$, so we can obtain $f_s' = (L/D)f_s = 30\ Hz$. The design details are discussed in **Sections 2.4 and 2.5**. Through this sampling rate reduction, all the frequency components above $15\ Hz$ are

already eliminated in the sampling rate conversion operations. The resampled data and the corresponding DFT values of the normal force, the axial force and the pitch moment are plotted in Figure 2.16 (a-f), respectively.

From Figure 2.16 (a) and (b), one can see that the frequency components of the normal force at around $f_2 = 23.44\ Hz$ contained in the original data are attenuated in the resampling process. What is left in the resampled data are frequency components associated with the maneuver frequency and the dominant mode frequency $f_1 = 9.28\ Hz$ of the sting.

For the axial force, the resampled data contain the DC values and the frequency component associated with maneuver frequency. Through the sampling rate reduction, one can see that the frequency resolution is also increased since we can not resolve the DC component with the component associated with the maneuver frequency in the original data by using the same point-DFT as shown in Figure 2.15 (d). Besides these components, one can also identify some small contributions to the axial force due to the dominant mode of the sting at $f_1 = 9.28\ Hz$, from Figure 2.16 (c) and (d).

From Figure 2.16 (e) and (f), one can see that the resampled data of the pitch moment contain the DC values, the component associated with the maneuver frequency and the component associated with the dominant frequency of the sting at $f_1 = 9.28\ Hz$. Those high frequency components are already removed from the data in the resampling process.

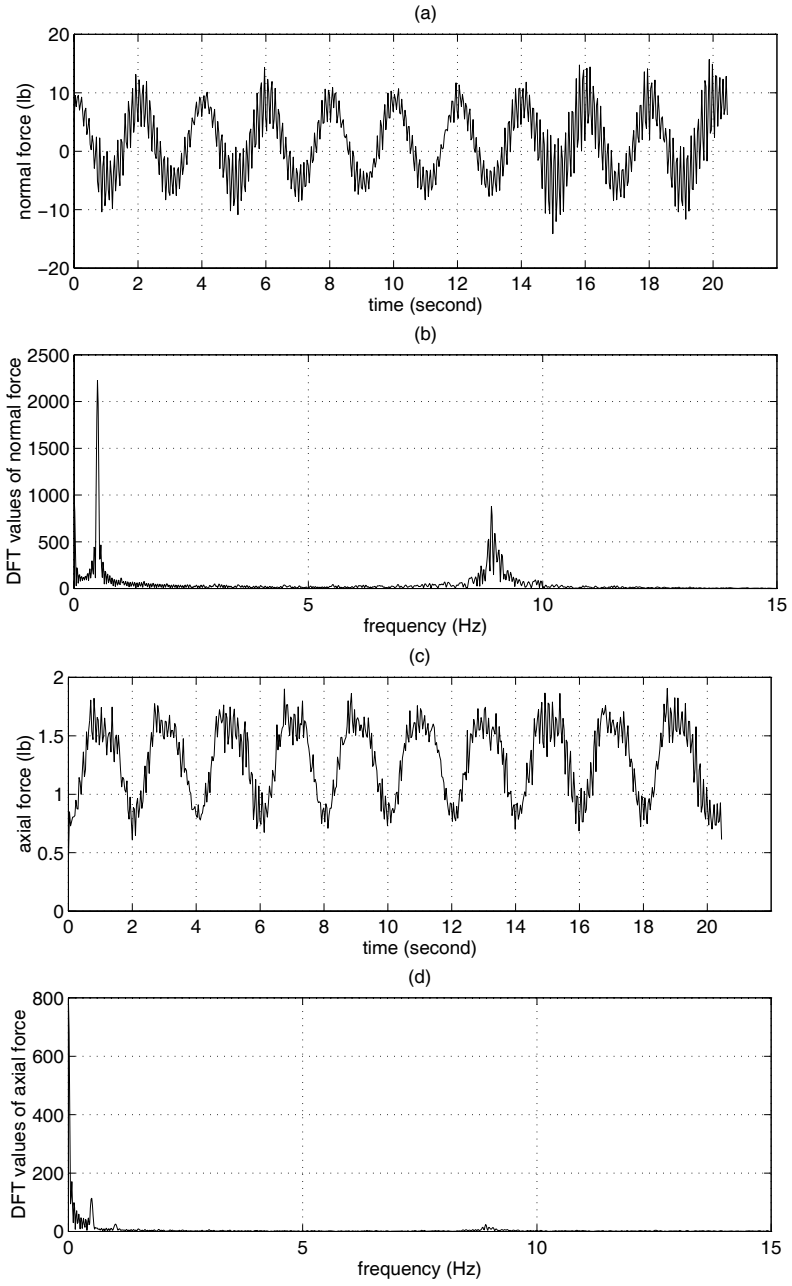
(a)
normal force (lb)
time (second)
(b)
DFT values of normal force
frequency (Hz)
(c)
axial force (lb)
time (second)
(d)
DFT values of axial force
frequency (Hz)

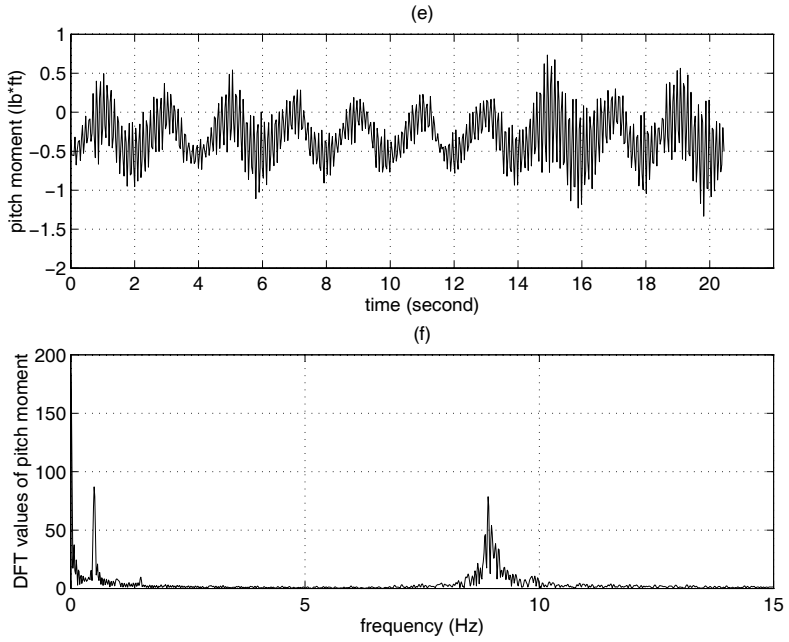

Figure 2.16: (a) Resampled normal force (b) DFT's of resampled ΔN_{bal} (c) Resampled axial force (d) DFT's of resampled axial force (e) Resampled pitch moment (f) DFT's of the resampled pitch moment

2.7.1.2 Digital Filtering of the Data

As we discussed before, the DC values and the components of the balance data at the frequency of pre-programmed maneuver are the aerodynamic responses to the angle of attack time history $\alpha_{fdbk}(n)$ measured by the DyPPiR for the pitch oscillatory maneuver while the components at the natural frequencies of the sting are the aerodynamic responses to the angle of attack variation time history $\Delta\alpha(n)$ due to the elastic deformation of the sting and some residual inertia loads. With the resampled data as given in Figure 2.16, we need to design a digital lowpass filter at the new sampling rate $f_s' = 30\ Hz$ to eliminate the frequency components at the natural frequency of the sting ($f_1 = 9.28\ Hz$).

The specifications for the digital lowpass filter are given as follows. Since the frequency for the current maneuver is 0.5 Hz, we define the passband edge frequency as $f_p = 1.5\ Hz$ and the stopband edge frequency as $f_q = 2.5\ Hz$. The width of the transition band is thus $\Delta f = 1\ Hz$. The digital versions of these edge frequencies can be obtained by normalizing them using new sampling rate $f_s' = 30\ Hz$, that is,

$$\begin{aligned} \omega_p &= 2\pi f_p / f_s' = 0.1\pi \\ \omega_s &= 2\pi f_q / f_s' = 0.1667\pi \end{aligned} \tag{2.66}$$

and furthermore we define the passband ripple and stopband attenuation requirements as,

$$\begin{aligned} \delta_p &\leq 0.005 \\ \delta_s &\leq 0.001 \end{aligned} \tag{2.67}$$

As one can see that the specifications as given above are exactly same as those given in Eq.(2.60) and thus the digital filter satisfying these specifications obtained there by using Remez algorithm can be used to process the current aerodynamic data. The frequency responses of this filter were shown in Figure 2.13 and the impulse response in time domain shown in Figure 2.14.

Using this digital filter, we further processed the data of the normal force, the axial force and the pitch moment as shown in Figure 2.16 (a), (c) and (e). As we pointed out in Eq.(2.64), when these data pass through the filter, all the frequency components in passband are purely delayed by $M/2 = 42$ samples on the output. These delay effects can easily be eliminated by getting rid of the first 42 samples in the output sequences. That is the reason why we need a filter of the even order in order to make $M/2$ an integer. After these operations, the filtered time histories of the normal force, the axial force and the pitch moment are plotted in Figure 2.17 (a), (c) and (e), respectively while their DFT values are plotted in Figure 2.17 (b), (d) and (f), accordingly.

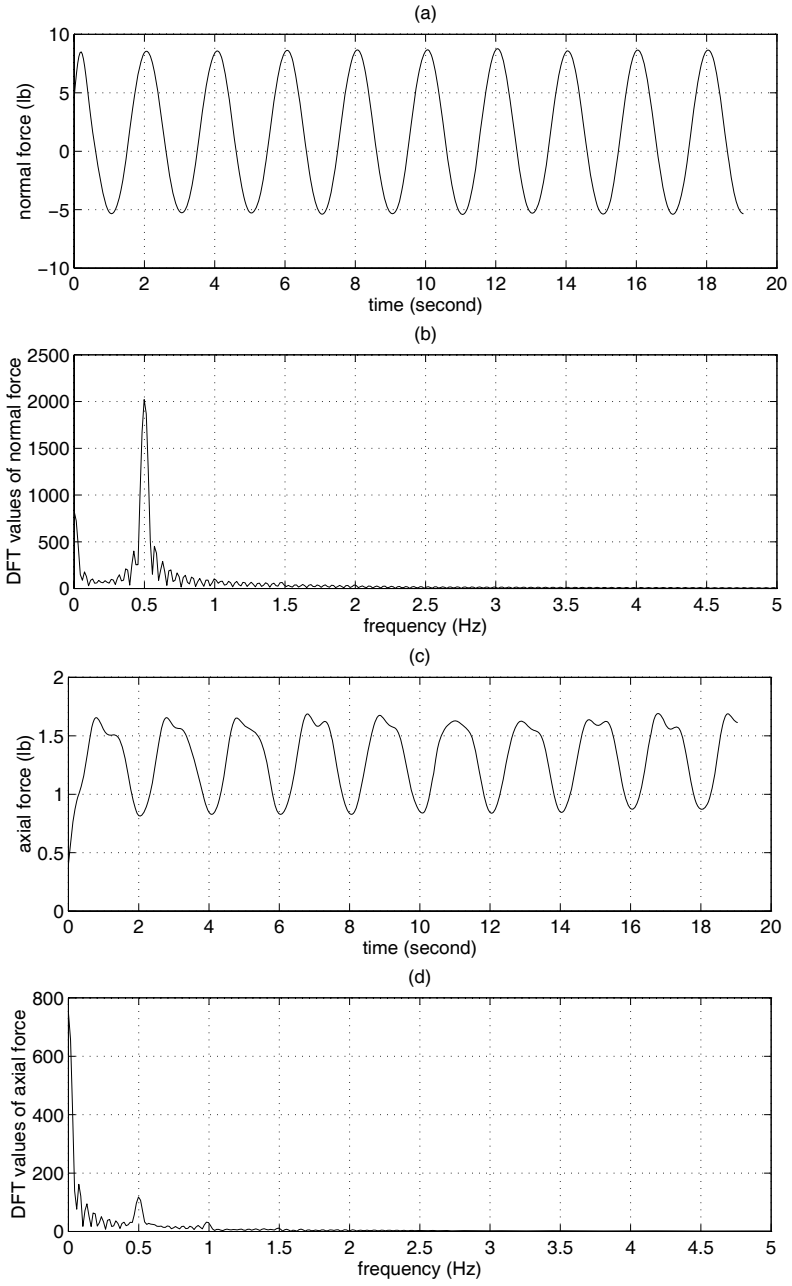
(a)
normal force (lb)
time (second)
(b)
DFT values of normal force
frequency (Hz)
(c)
axial force (lb)
time (second)
(d)
DFT values of axial force
frequency (Hz)

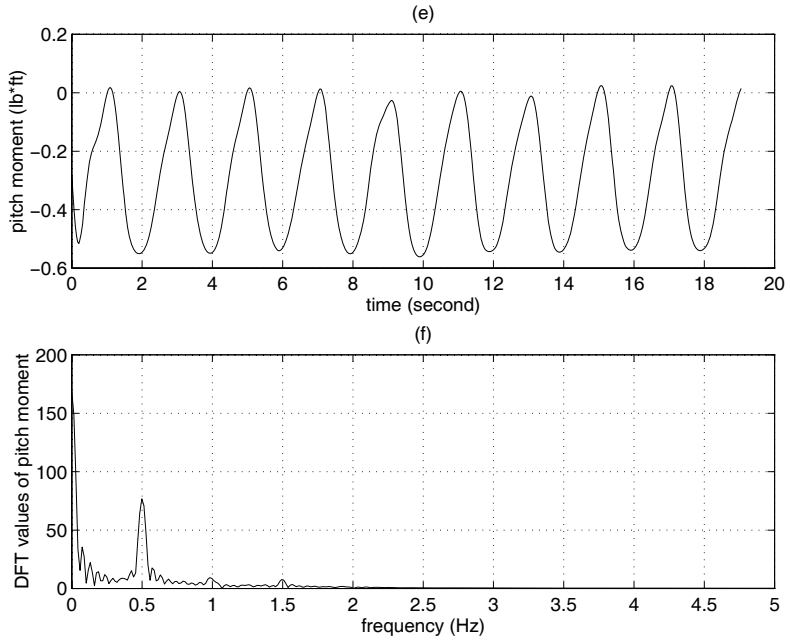

Figure 2.17: (a) Time history of N_{aero} (b) DFT's of N_{aero} (c) Time history of X_{aero} (d) DFT's of X_{aero} (e) Time history of M_{aero} (f) DFT's of M_{aero}

From Figure 2.17 (a) and (b), one can see that the normal force response has the dominant component at $f = 0.5\ Hz$ which is the frequency of the maneuver. Besides this component, this normal force response also has DC values which mean nonzero normal force at zero angle of attack for this aircraft.

From Figure 2.17 (c) and (d), one can see that the dominant component of the axial force response is the DC value. This result occurs because the axial force is the major contribution to the drag. One can also see a small frequency component of the axial force at the maneuver frequency.

From Figure 2.17 (e) and (f), one can see that the pitch moment also has relatively large DC value, as well as the frequency component at $f = 0.5\ Hz$.

2.7.1.3 Computation of Input Time Histories

The time histories as shown in Figure 2.17 (a), (c) and (e) are the aerodynamic forces and moment responses to the angle of attack time history $\alpha_{fdbk}(n)$. This angle of attack time history was measured by the DyPPiR and plotted in Figure 2.18 (a) as a dashed line.

From the aerodynamics modeling point of view, the inputs also include $\dot{\alpha}(t)$ and pitch rate $q(t)$, and these two time histories were not measured in the experimental data acquisition. However, since $\dot{\alpha}(t) = q(t)$ in the wind-tunnel tests, we can obtain these time histories from the angle of attack measurements by numerical differentiation.

As we mentioned previously, we have 4096 samples obtained at the sampling rate of $f_s = 200\ Hz$ for all the measured variables in the experimental data acquisiton. Therefore we also want to compute 4096 samples of the derivatives $\dot{\alpha}_{fdbk}(n)$ from the 4096 samples of the angle of attack measurements. Here we use the 2nd forward finite difference equation to compute the 1st sample of the derivative and 2nd backward finite difference to compute the last sample. For the samples in between, we use 2nd order central difference approximation. The mathematical equations used are given as follows,

$$\begin{aligned}
\dot{\alpha}_{fdbk}(1) &= \frac{-3\alpha_{fdbk}(1) + 4\alpha_{fdbk}(2) - \alpha_{fdbk}(3)}{2T_s} \\
\dot{\alpha}_{fdbk}(i) &= \frac{\alpha_{fdbk}(i+1) - \alpha_{fdbk}(i-1)}{2T_s}, \qquad i = 2, 3, 4, ..., 4095 \\
\dot{\alpha}_{fdbk}(4096) &= \frac{3\alpha_{fdbk}(4096) - 4\alpha_{fdbk}(4095) + \alpha_{fdbk}(4094)}{2T_s}
\end{aligned} \tag{2.68}$$

where $T_s = 1/f_s$ is the sampling period.

The results obtained from the above numerical differentiation schemes are plotted in Figure 2.18 (a) as solid line. For the convenience of comparison, we actually plot this derivative scaled by the frequency so that it is supposed to have the same amplitude as the angle of

attack. From the plot, one can see that this numerical differentiation result contains noise besides the frequency component of the pitch rate. This noise is caused by the numerical differentiation, so we should eliminate it by a filtering operation.

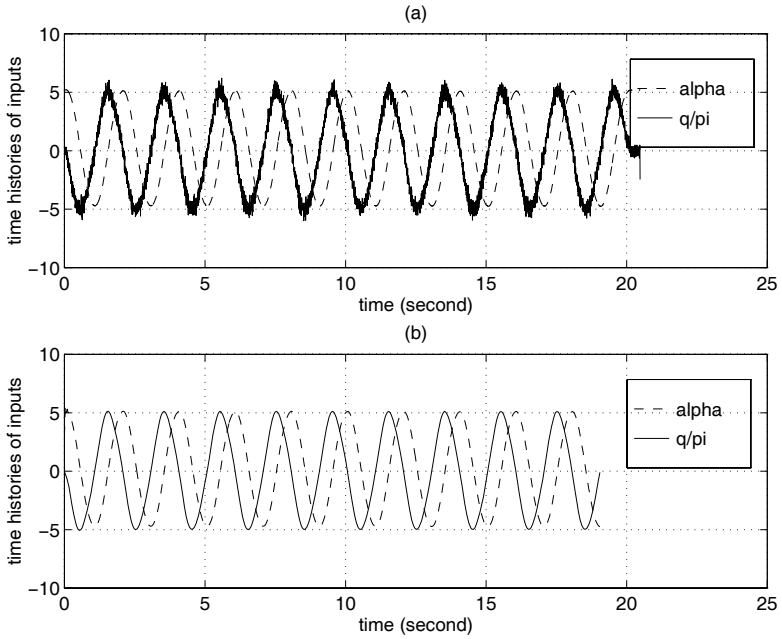

Figure 2.18: (a) Raw data of α and $\dot{\alpha}$ (b) Resampled data of α and $\dot{\alpha}$

Consistent to the processing of the forces and moment, we resample the angle of attack measurements and the computed derivatives using new sampling rate $f_s' = 30\ Hz$. Then we apply a digital filter to the resampled pitch rate only since we assume that the pitch rate in this case should have the same frequency component as the angle of attack. The resampled angle of attack and the filtered pitch rate are plotted in Figure 2.18 (b) as dashed line and solid line, respectively. These are considered as the input time histories of the maneuver. The responses of the unsteady aerodynamics to these input time histories are the time histories of the normal force , the axial force and the pitch moment as shown in Figure 2.17 (a), (c) and (e), respectively.

2.7.1.4 Computation of Aerodynamic Coefficients

Using the obtained time histories of the normal force and the axial force, we can compute the corresponding time histories of the lift and drag by,

$$\begin{aligned} L_{aero} &= F_{n,aero}cos(\alpha_{fdbk}) - F_{x,aero}sin(\alpha_{fdbk}) \\ D_{aero} &= F_{n,aero}sin(\alpha_{fdbk}) + F_{x,aero}cos(\alpha_{fdbk}) \end{aligned} \tag{2.69}$$

and the aerodynamic coefficient time histories can then be obtained by,

$$\begin{aligned} C_L &= \frac{L_{aero}}{QS} \\ C_D &= \frac{D_{aero}}{QS} \\ C_m &= \frac{M_{aero}}{QSc} \end{aligned} \tag{2.70}$$

where Q is the measured dynamic pressure.

The time histories of the lift, drag and pitch moment coefficients for this maneuver are plotted as solid lines in Figure 2.19 (a), (b) and (c), respectively.

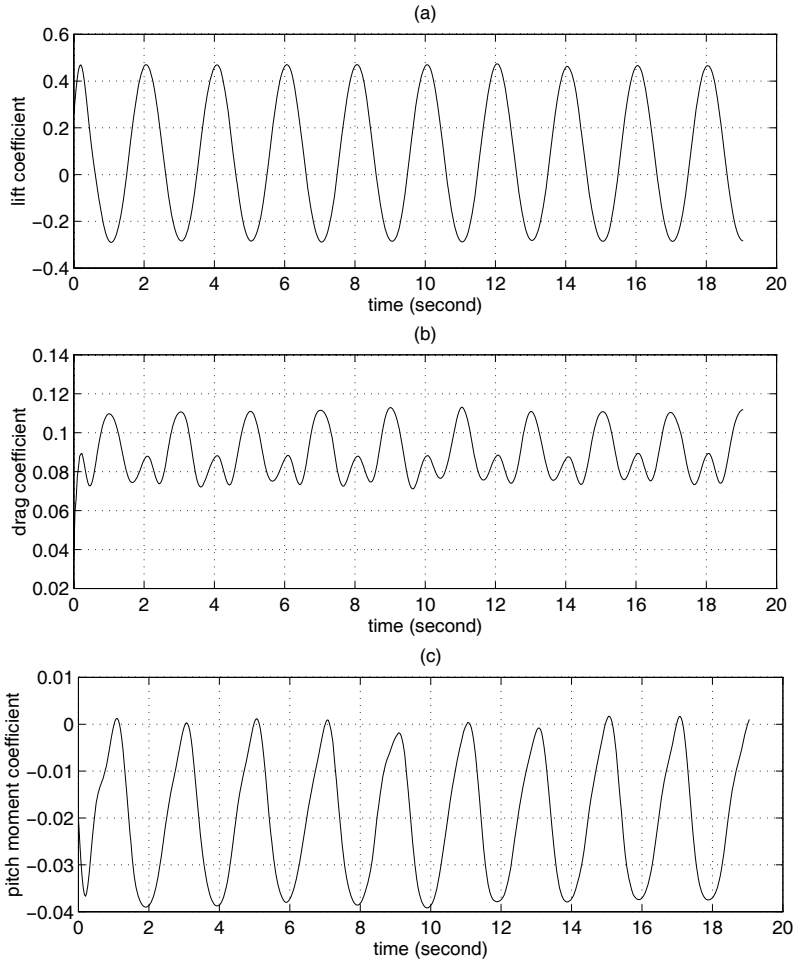

Figure 2.19: Aerodynamic coefficient time histories for the maneuvers of $\alpha_A = 5^o$, f=0.5 Hz and $\alpha_0 = 0^o$ at the tunnel speed of V=95 ft/s

2.7.2 Data Processing for an Oscillatory Plunge Maneuver

For the oscillatory maneuvers in plunge, the resampling and filtering operations of the balance data are completely similar to the procedures as illustrated above for the oscillatory maneuvers in pitch. However, unlike the oscillatory maneuvers in pitch, the input signal $\alpha_{fdbk}(n)$ are not directly measured by the DyPPiR. We have to obtain this input time history from the DyPPiR plunge measurements by numerical differentiation according to kinematic relations given in Eq.(2.3).

First we have to compute the actual tunnel speed time histories V from the DyPPiR measurements. Currently, the data acquisition system measures the tunnel dynamic pressure Q (lbs/ft^2), the ambient pressure P (lbs/ft^2), and the tunnel temperature T_m (K) at the same sampling frequency as the other measurements. From the ambient pressure and the temperature measurements, we can compute the actual density time history ρ (slug/ft^3) in the test by the ideal-gas equation of state,

$$\rho(n) = \frac{P(n)}{RT_m(n)} \tag{2.71}$$

where $R = 3089.2$ (lbs.ft/slug.K) is the gas constant, and n is the index of samples.

Then from the measurement of the tunnel dynamic pressure Q and the density ρ obtained above, we can further compute the actual tunnel speed by

$$V(n) = \sqrt{\frac{2Q(n)}{\rho(n)}} \tag{2.72}$$

After obtaining the tunnel speed time history, we then differentiate the plunge position measurements $h(n)$ of the DyPPiR numerically to obtain the first derivative $\dot{h}(n)$ by using the same schemes given in Eq.(2.68). The angle-of-attack time history as input are then obtained by the kinematic relation given in Eq.(2.3), i.e.,

$$\alpha_{fdbk}(n) = tan^{-1}\{\frac{V(n)sin(\alpha_0) - \dot{h}(n)cos(\alpha_0)}{V(n)cos(\alpha_0) + \dot{h}(n)sin(\alpha_0)}\} \tag{2.73}$$

The pitch rate $\hat{q} = 0$ in the plunge oscillations while the derivative of the angle of attack $\dot{\alpha}_{fdbk}(n)$ can further be obtained by the $h(n)$ and $\dot{h}(n)$ using the kinematic relation given in Eq.(2.3) as follows,

$$\dot{\alpha}(n) = \frac{V(n)h(n)\omega^2 cos^2[\alpha_{fdbk}(n)]}{[V(n)cos(\alpha_0) + \dot{h}(n)sin(\alpha_0)]^2} \tag{2.74}$$

Thus, the input time histories for the oscillatory maneuvers in plunge are finally obtained through the Eqs.(2.73) and (2.74).

Here, we illustrate the data reduction procedure for an oscillatory plunge maneuver with $\alpha_0 = 0$, $h_A = 0.5$ ft, and $f = 1.5$ Hz. The sampling frequency for this maneuver is $f_s = 600$ Hz, which implies a 300 Hz bandwidth of interest. Therefore, we only need to perform a decimation by factor $D = 20$ to achieve the new sampling rate of $f_s' = 30$ Hz of interest.

By following the procedures discussed above, the input time histories of the $\alpha_{fdbk}(n)$ and the $\dot{\alpha}_{fdbk}(n)$ are obtained and plotted in Figure 2.20 (a) ($\dot{\alpha}_{fdbk}(n)$ is scaled by the frequency $2\pi f$ in the plot). As one can see, the $\alpha_{fdbk}(n)$ is noisy while the $\dot{\alpha}_{fdbk}(n)$ is smooth. This result occurs because the $\alpha_{fdbk}(n)$ is computed from the $\dot{h}(n)$ which is obtained from the numerical differentiation of the $h(n)$ while the $\dot{\alpha}_{fdbk}(n)$ are dominated by the $h(n)$ and are computed directly from the DyPPiR plunge measurements.

Figure 2.20 (b) shows the resampled and filtered time histories for the $\alpha_{fdbk}(n)$ and the scaled $\dot{\alpha}_{fdbk}(n)$, which are the input time histories for this maneuver.

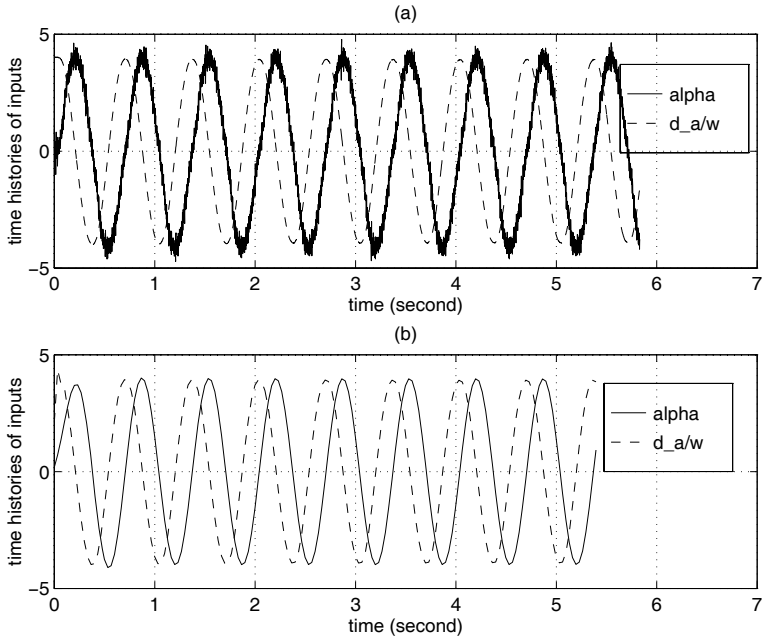

Figure 2.20: (a) Raw data of α and $\dot{\alpha}$ (b) Filtered data of α and $\dot{\alpha}$

Figure 2.21 (a), (c), and (e) plot the time histories of the normal force $\Delta F_{n,bal}(n)$, the axial force $\Delta F_{x,bal}(n)$, and the pitch moment $\Delta M_{bal}(n)$, which are obtained by subtracting the balance readings in wind-off test of this maneuver from those in the corresponding wind-on test. Figure 2.21 (b), (d), and (f) plot the DFT values of the normal force, the axial force and the pitch moment, respectively, to show the corresponding frequency contents. From these plots, one can see that these measurements are very noisy.

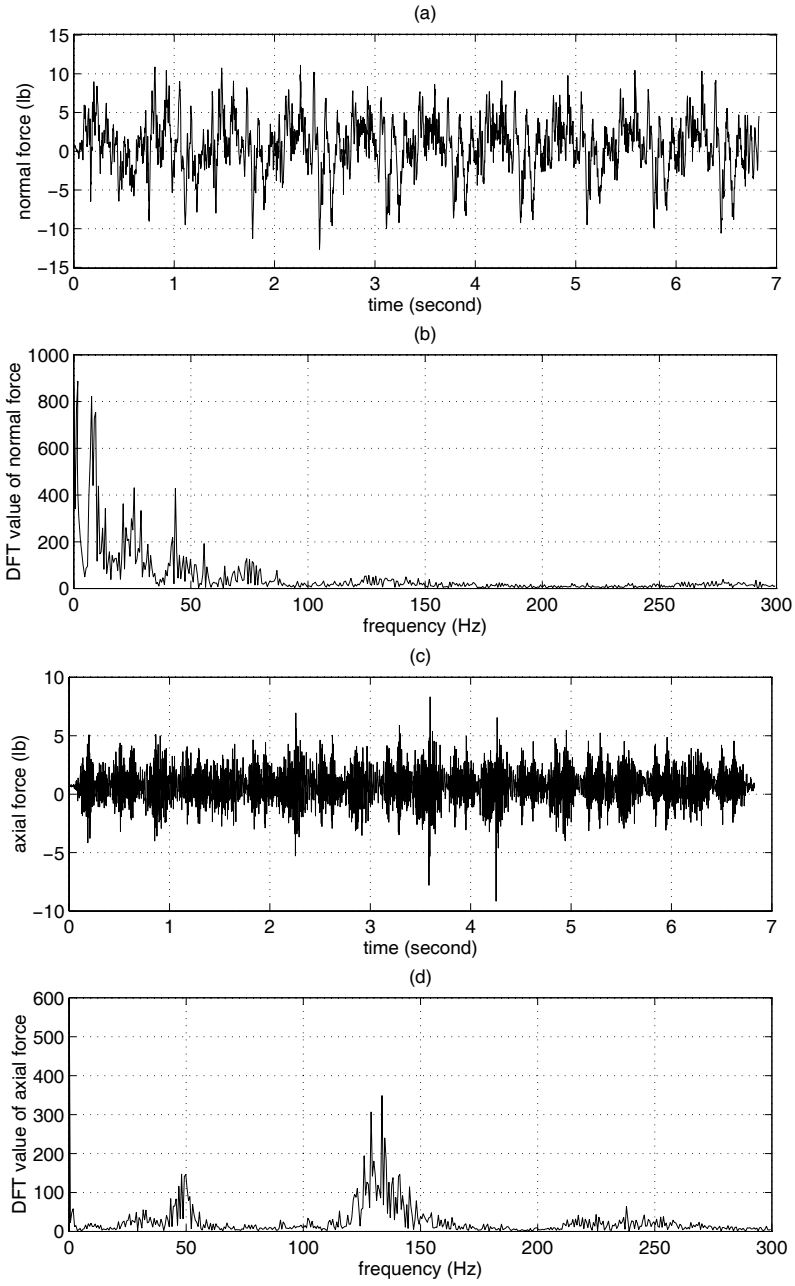
(a)
normal force (lb)
time (second)
(b)
DFT value of normal force
frequency (Hz)
(c)
axial force (lb)
time (second)
(d)
DFT value of axial force
frequency (Hz)

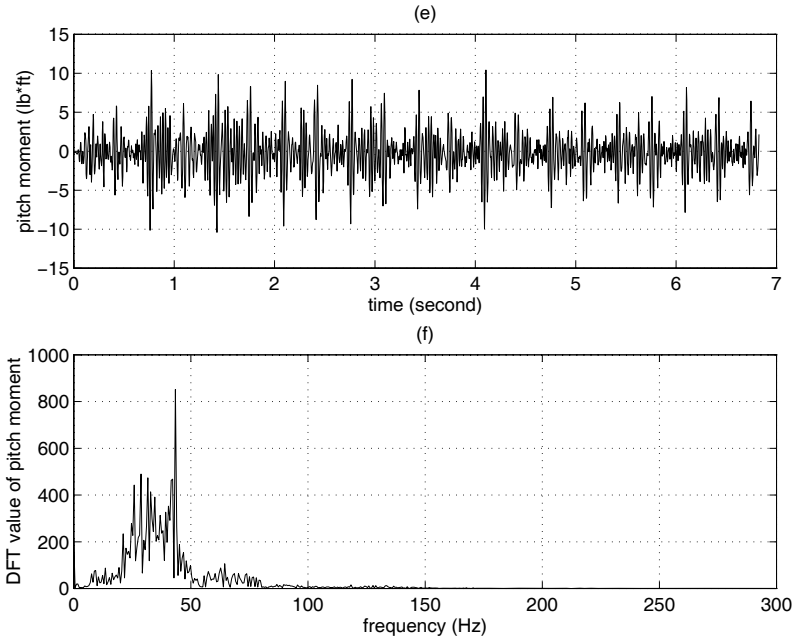

Figure 2.21: (a) Normal force time history (b) DFT values of normal force (c) Axial force time history (d) DFT values of axial force (e) Pitch moment time history (f) DFT values of pitch moment force

After performing the resampled and filtered operations on these balance measurements, the aerodynamic load responses to the input time histories shown in Figure 2.20 (b) are plotted in Figure 2.22 (a), (c), and (e) for the normal force, the axial force, and the pitch moment, respectively. Figure 2.22 (b), (d), and (f) plot the associated DFT values of these responses to show the corresponding frequency contents.

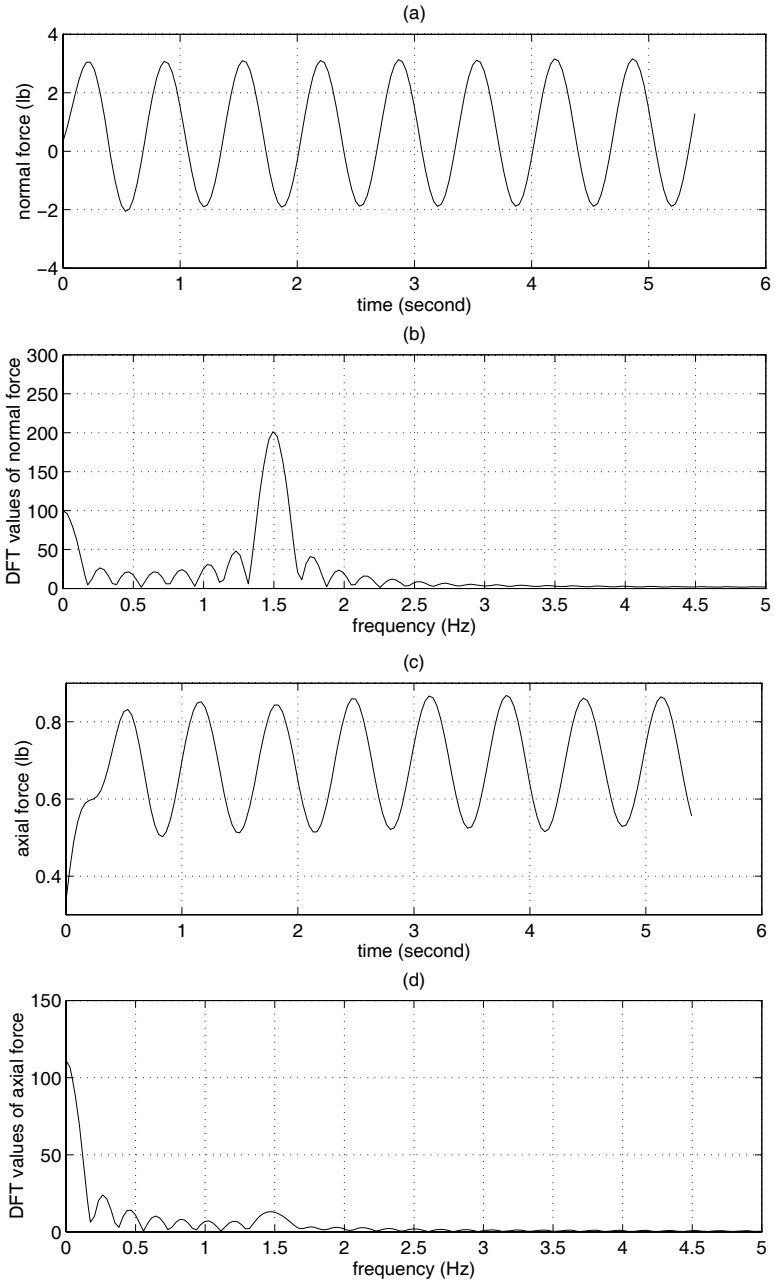
(a)
normal force (lb)
time (second)
(b)
DFT values of normal force
frequency (Hz)
(c)
axial force (lb)
time (second)
(d)
DFT values of axial force
frequency (Hz)

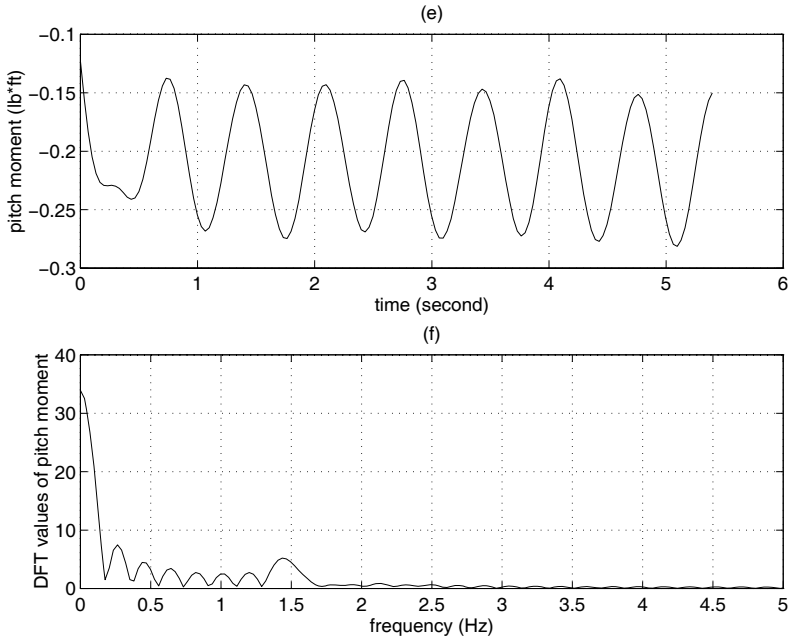

Figure 2.22: (a) Normal force time history (b) DFT values of normal force (c) Axial force time history (d) DFT values of axial force (e) Pitch moment time history (f) DFT values of pitch moment force

From Figure 2.22 (a) and (b), one can see that the normal force is dominated by the frequency component at the maneuver frequency of 1.5 Hz while the axial force is dominated by the DC values from Figure 2.22 (c) and (d). This result occurs because the axial force is the major contribution to the drag. From Figure 2.22 (e) and (f), one can see that the pitch moment is also dominated by the DC values even if there is a small component showing up at the maneuver frequency of 1.5 Hz.

From the normal force and the axial force given above, we can compute the lift and drag by using Eq.(2.69). Then the aerodyamic coefficient time histories for this maneuver can be further computed by Eq.(2.70). The obtained lift, drag, and pitch moment coefficients are plotted in in Figure 2.23 (a), (b), and (c), respectively.

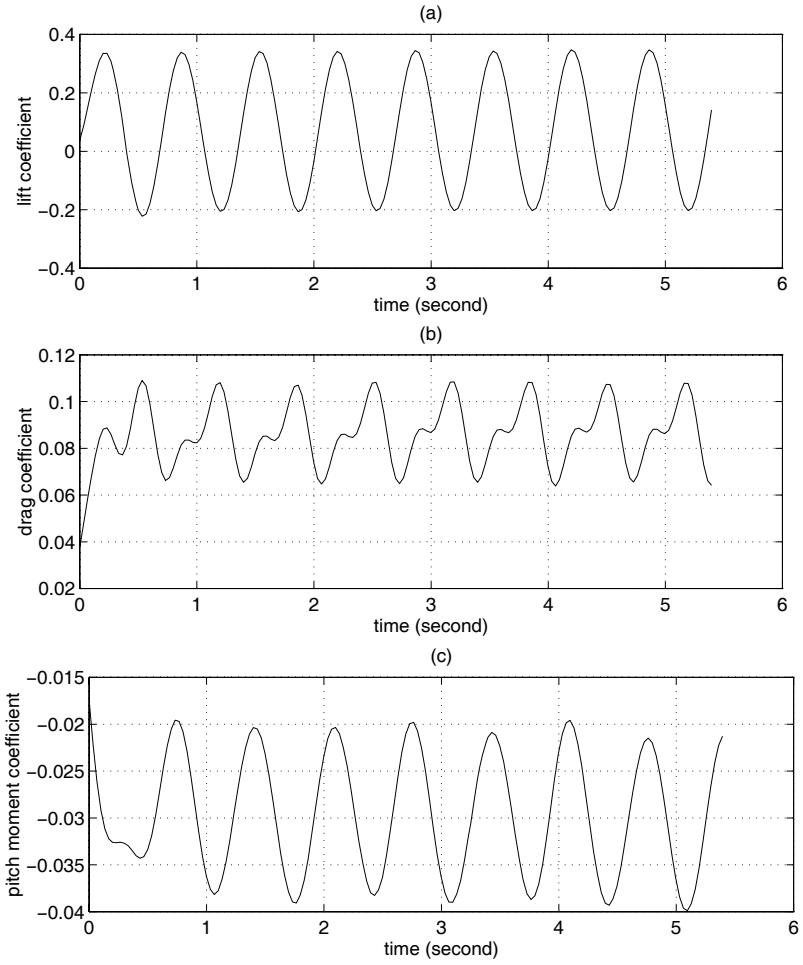

Figure 2.23: Aerodynamic coefficient time histories for plunge oscillatory maneuver of $h_A = 0.5\ ft, f = 1.5\ Hz$ and $\alpha_0 = 0^o$ at the tunnel speed of V=67 ft/s

2.8 Summary

In this chapter, the data reduction techniques for the harmonic oscillatory tests of the DyPPiR have been developed based on the multirate signal processing method. First the sting is modeled as a cantilever beam with the model mounted on the free end, and the associated elastic modes of the sting were identified by using the Discrete Fourier Transform. Based on these results, it was found that the aerodynamic responses to the preprogrammed inputs can be resolved from other frequency components of the balance readings in the frequency domain. Thus digital systems based on multirate signal processing approach were developed to extract the aerodynamic responses to the preprogrammed input time histories. The performances of the developed digital systems were then illustrated by reducing the data for an oscillatory pitch maneuver and an oscillatory plunge maneuver. Using these techniques, all the experimental data in the current harmonic oscillatory tests have been reduced.

Chapter 3

Unsteady Aerodynamic Data and Analyses

In Chapter 2, we performed the harmonic oscillatory tests for an F-18 configuration, and obtained the corresponding aerodynamic responses to the preprogrammed inputs. In this chapter, we are going to present some of these results, look at them in detail and analyze the associated unsteady aerodynamic characteristics.

Besides the harmonic oscillatory data obtained above, we also investigate some other unsteady aerodynamic measurements from the documented references. These data include the lift-curve characteristics for an airfoil pitching-up at constant rate in Ref. [18], the normal force responses for the harmonic oscillations in pitch for a highly swept delta wing in Ref. [30], and the longitudinal aerodynamics for an F-18 configuration pitching-up and pitching-down at various constant rates, also in Ref. [30]. All these experimental results provide the insights into the unsteady aerodynamic characteristics from various aspects. We will briefly discuss these results in this chapter and provide some basis for modeling the unsteady aerodynamic characteristics in following chapters.

3.1 Harmonic Oscillatory Maneuvers in Pitch

Numerous studies have documented the hysteresis and overshoot characteristics as the model is undergoing pitch oscillations at high angles of attack. The flow mechanisms responsible for these unsteady effects are the dynamic lags of the vortex bursting and flow separations. Because of these flow lags, it is generally expected that the aerodynamic forces and moment will exhibit similar hysteresis loops in the pitch oscillatory maneuvers.

In the current pitch oscillatory tests, however, the tested angle of attack range is below 40^o and the reduced frequencies $\hat{\omega} = \omega c/2V$ in the tests are not large. In such testing conditions, the flowfields may not result in significant dynamic effects of vortex bursting and flow separations.

In this section, we first illustrate some typical pitch oscillatory results, then analyze the aerodynamic characteristics associated with them, and finally provide some more results for unsteady aerodynamics modeling.

3.1.1 Data Illustrations

Figures 3.1, 3.2 and 3.3, respectively, plot the lift, the drag and the pitch moment coefficients for the pitch oscillations of amplitude of 5^o, about three mean angles of attack (0^o, 12^o and 24^o) with two extreme frequencies (0.5 Hz and 1.414 Hz) at the tunnel speed of 67 ft/s. The static data are also shown in the plots.

From Figures 3.1 and 3.2, one observed no significant hysteresis loops for the lift and the drag coefficients in the oscillations for the current angle of attack range and the frequencies. This observation suggests that the dynamic lags of the vortex and separation flows are small in the current oscillatory maneuvers. The flowfields around the model are pretty much at

the attached flow conditions. However, one can see the significant hysteresis loops for the pitch moment coefficients at such flow conditions from Figure 3.3. It can further be observed that these hysteresis loops are dependent on the amplitudes, the frequencies and the mean angles of attack of the oscillations. One can also see, from these plots, that as the model is oscillated at high angles of attack, the hysteresis loops become large and as the oscillatory frequencies are increased, the sizes of these hysteresis loops are also increased.

The unsteady aerodynamic characteristics responsible for the above observations can be attributed to the effects of the pitch rate $q(t)$ and the $\dot{\alpha}(t)$. The associated flow mechanism can be analyzed as follows.

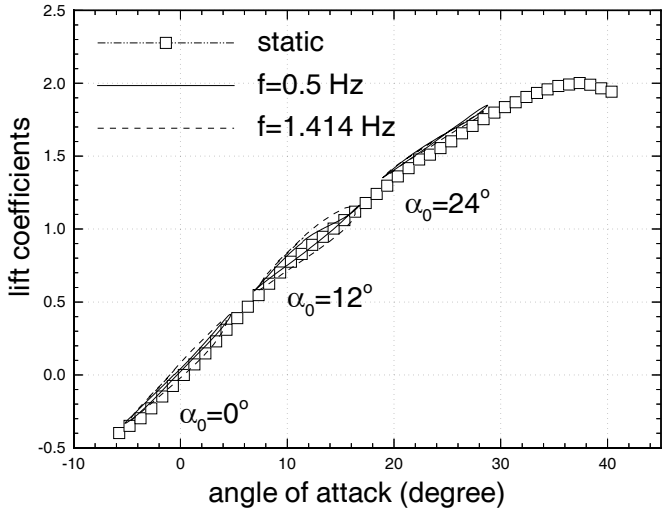

Figure 3.1: Lift coefficient for pitch oscillation with amplitude of 5 degrees

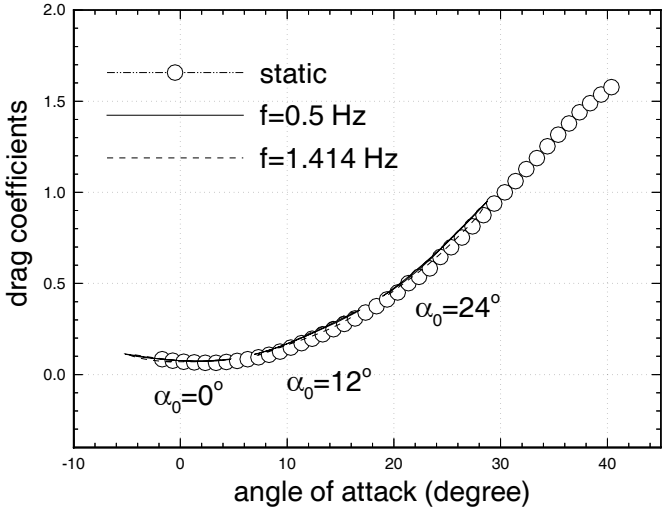

Figure 3.2: Drag coefficient for pitch oscillation with amplitude of 5 degrees

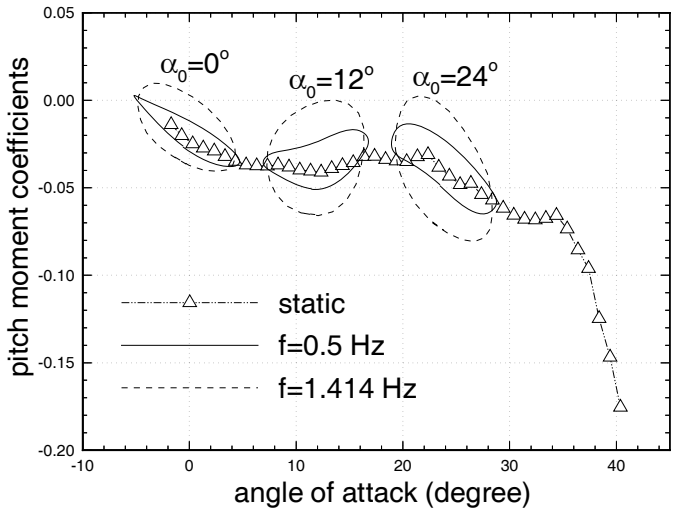

Figure 3.3: Pitch moment coefficient for pitch oscillation with amplitude of 5 degrees

3.1.2 Pitch Rate Effects

Suppose that the unsteady aerodynamics in the current oscillatory maneuvers can be modeled by the following static systems,

$$\begin{aligned} C_L &= C_L(\alpha, q) \\ C_D &= C_D(\alpha, q) \\ C_m &= C_m(\alpha, q) \end{aligned} \tag{3.1}$$

For the current oscillatory maneuvers in pitch, the motion time histories are given by Eq.(2.1). Substituting those motion time histories into Eq.(3.1), we can obtain the corresponding time histories of the aerodynamic coefficients.

By looking at the motion time histories given in Eq.(2.1), one can see that the angle of attack $\alpha(t)$ and the pitch rate $q(t)$ have a phase difference of 90 degrees. Thus if we plot the pitch rate versus the angle of attack, we will get a loop in the $q - \alpha$ plane. Therefore, the dependencies of aerodynamic coefficients on the pitch rate can produce hysteresis loops in the pitch oscillatory maneuvers.

The pitch rate effects represent the aerodynamic characteristics that accompany rotation of the aircraft about a spanwise axis through the C.G. while α remains fixed. Both the wing and the tail are affected by the rotation, although, when the aircraft has a tail, the wing contribution to C_L and C_m due to pitch rate is negligible in comparison with that of the tail for most cases.

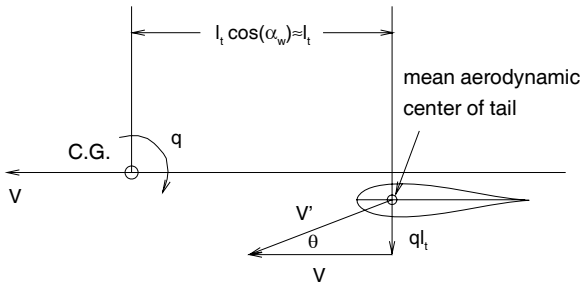

Figure 3.4: Effect of rotation on tail angle of attack

As is illustrated in Figure 3.4, the main effect of $q(t)$ on the tail is to increase its angle of attack by $q(t)l_t/V$, where l_t is the length from the C.G. of the aircraft to the tail mean aerodynamic center, and V is the flight speed. It is this change in the tail angle of attack that accounts for the changes of the forces on the tail. It is generally assumed

that the instantaneous forces on the tail correspond to its instantaneous angle of attack, i.e., no account is taken of the fact that it takes a finite time for the tail lift to build up to its steady-state value following a sudden change in $q(t)$. Therefore, the results are obtained under quasistatic assumptions. Thus, the change in tail lift coefficient caused by the rotation of the aircraft is,

$$\Delta C_{Lt} = a_t \Delta\alpha_t = a_t \frac{q l_t}{V} \tag{3.2}$$

where a_t is the tail lift slope.

The corresponding increments in aircraft lift and pitch moment coefficients that corresponds to ΔC_{Lt} are,

$$\begin{aligned} \Delta C_L &= \frac{S_t}{S}\Delta C_{Lt} = \frac{S_t}{S} a_t \frac{q l_t}{V} \\ \Delta C_m &= -V_H \Delta C_{Lt} = -a_t V_H \frac{q l_t}{V} \end{aligned} \tag{3.3}$$

where S and S_t are the reference areas of the wing-body and tail, respectively. V_H is the tail volume ratio which is defined as,

$$V_H = \frac{l_t S_t}{S c} \tag{3.4}$$

Based on the changes in lift and pitch moment as given in Eq.(3.3), the pitch rate derivatives are defined as,

$$\begin{aligned} \frac{\partial C_L}{\partial q} &= a_t \frac{S_t}{S}\frac{l_t}{V} \\ \frac{\partial C_m}{\partial q} &= a_t V_H \frac{l_t}{V} \end{aligned} \tag{3.5}$$

With the modeling of the pitch rate effects as the above derivatives, the aerodynamic coefficients given in Eq.(3.1) can be written as,

$$\begin{aligned} C_L &= C_L(\alpha) + C_{L\hat{q}} q\hat{t} \\ C_D &= C_D(\alpha) + C_{D\hat{q}} q\hat{t} \\ C_m &= C_m(\alpha) + C_{m\hat{q}} q\hat{t} \end{aligned} \tag{3.6}$$

where the $C_{a\hat{q}},\ a = L, D, or\ m$, are the corresponding aerodynamic derivatives with respect to the nondimensional pitch rate $\hat{q} = q\hat{t}$. The $\hat{t}$ is the characteristic time of the flow which is defined as,

$$\hat{t} = \frac{c}{2V} \tag{3.7}$$

From Eq.(3.6), one can see, more clearly, that if the aerodynamic coefficients have large pitch rate dependencies, they will have large hysteresis loops in the pitch oscillations. If the aerodynamic coefficients have weak pitch rate dependencies, the resulting hysteresis loops will be small. As was discussed above, the pitch moment generally has large pitch rate dependency since the forces on the tail are major forces to generate the pitch moment. The lift generally has small pitch rate dependency because the forces on the tail are just a small portion of the total lift on the aircraft. The pitch rate dependency of drag coefficient is neglected in this analysis. One can see these results very clearly from Figures 3.1, 3.2 and 3.3.

We can illustrate one more example for the pitch rate effects. From Ref. [39], the expressions of the aerodynamic coefficients for an F-18 aircraft configuration were obtained by the interpolation of the table lookups as follows,

$$\begin{aligned} C_L &= \begin{cases} 0.732 + 0.0751\alpha, & -5 \le \alpha \le 10 \\ 0.569 + 0.106\alpha - 0.00148\alpha^2, & 10 \le \alpha \le 40 \end{cases} \\ C_D &= \begin{cases} 0.1423 - 0.00438\alpha + 0.0013\alpha^2, & -5 \le \alpha \le 20 \\ -0.3580 + 0.0473\alpha - 0.0000348\alpha^2, & 20 \le \alpha \le 40 \end{cases} \\ C_m &= -0.1885 - 0.00437\alpha - 0.123q \end{aligned} \tag{3.8}$$

where α is in degrees and q in radians per second.

We then simulate this aerodynamic system given in Eq.(3.8) for the pitch oscillatory maneuvers. Since the dependencies of the lift and the drag coefficients on the pitch rate are neglected in this system, there are no hysteresis loops existing in the oscillations. However, there are hysteresis loops for the pitch moment coefficient in the oscillations because of the relatively large pitch rate dependency. Figure 3.5 shows the simulation results of Eq. (3.8) by using the motion time history measurements associated with the experimental results as shown in Figure 3.3.

From Figure 3.5, one can see the responsibility of the pitch rate for the hysteresis loops in the pitch oscillatory motions. From the plots, one can also see that these hysteresis loops are dependent on the amplitudes and the frequencies of the oscillatory motions, but independent of the mean angles of attack since the static pitch moment coefficient is linear in α and q, and the other unsteady aerodynamic effects are not included in this system.

Looking at the experimental results as shown in Figure 3.3, however, one can see that the shapes of the hysteresis loops depend not only on the amplitudes and the frequencies, but also on the mean angles of attack of the oscillations. These results imply the nonlinearities in α and q, i.e., the derivatives of C_m with respect to $\alpha(t)$ and $q(t)$ are no longer constant. The unsteady aerodynamics of the pitch rate $q(t)$ and of $\dot{\alpha}$ must be considered and properly

modeled for the current harmonic oscillatory tests.

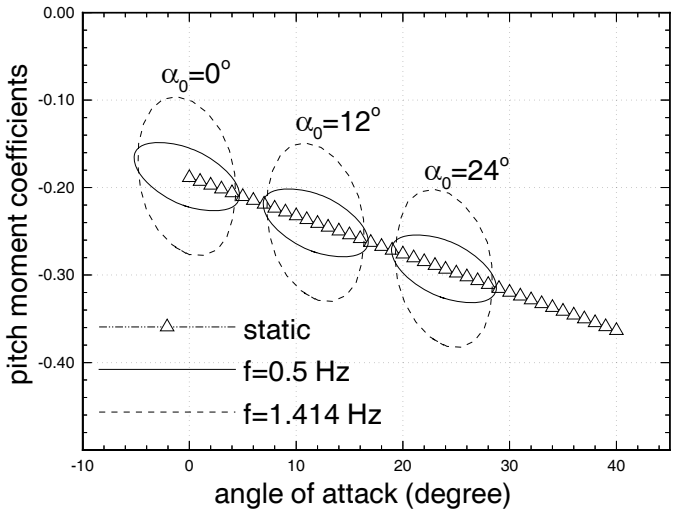

Figure 3.5: Pitch moment coefficient of the static aerodynamic system

3.1.3 The $\dot{\alpha}(t)$ Effects

The $\dot{\alpha}(t)$ effects owe their existence to the fact that the pressure distribution on a wing or tail does not adjust itself instantaneously to its equilibrium value when the angle of attack is suddenly changed. The calculation of this effect, or its measurement involves the unsteady flows.

Systematic discussions of the $\dot{\alpha}(t)$ effects are beyond the scope of present work. One can refer to Refs. [1,2] for details. Currently, we are mainly concerned with the large hysteresis loops of pitch moment coefficients in the pitch oscillatory motions. Since the lift on the tail surface makes significant contribution to the pitch moment, the $\dot{\alpha}(t)$ effects on the tail lift is the major interest. There is a traditional method[1,2] for evaluating the contributions of the tail surface, based on the lag of the downwash. It neglects entirely the nonstationary character of the lift response of the tail to changes in tail angle of attack, and attributes the result entirely to the fact that the downwash at the tail does not respond instantaneously to changes in wing angle of attack. The downwash is assumed to be dependent primarily on the strength of the wing's trailing vortices in the neighborhood of the tail. Since the vorticity is convected with the stream, then a change in the circulation at the wing will not be felt as a change in downwash at the tail until a time $\Delta t = l_t/V$ has elapsed, where l_t is the length from the C.G. of the aircraft to the tail mean aerodynamic center, as shown in Figure 3.6. This delay is then modeled such that the instantaneous downwash at the tail, $\epsilon(t)$, corresponds to the wing angle of attack $\alpha(t)$ at time $(t - \Delta t)$. The corrections to the quasistatic downwash and tail angle of attack are therefore,

$$\begin{aligned} \Delta\epsilon &= \frac{\partial\epsilon}{\partial\alpha}\dot{\alpha}\Delta t \\ &= -\frac{\partial\epsilon}{\partial\alpha}\dot{\alpha}\frac{l_t}{V} \\ &= -\Delta\alpha_t \end{aligned} \tag{3.9}$$

The correction to the tail lift coefficient for the downwash lag is then,

$$\Delta C_{Lt} = a_t \Delta\alpha_t = a_t \dot{\alpha} \frac{l_t}{V} \frac{\partial \epsilon}{\partial \alpha} \tag{3.10}$$

The corresponding corrections to the aircraft lift and pitch moment coefficients are then obtained from ΔC_{Lt} as,

$$\begin{aligned} \Delta C_L &= \Delta C_{Lt} \frac{S_t}{S} \\ &= a_t \dot{\alpha} \frac{l_t}{V} \frac{S_t}{S} \frac{\partial \epsilon}{\partial \alpha} \\ \Delta C_m &= -V_H \Delta C_{Lt} \\ &= -a_t \dot{\alpha} V_H \frac{l_t}{V} \frac{\partial \epsilon}{\partial \alpha} \end{aligned} \tag{3.11}$$

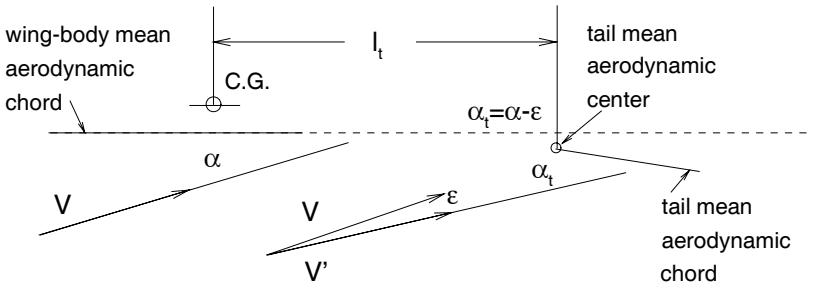

Figure 3.6: Wing downwash of the flow at the tail

From Eq.(3.11), one can see that the contributions of the $\dot{\alpha}$ effects to the lift and the pitch moment coefficients are proportional to $\dot{\alpha}$. These $\dot{\alpha}$ corrections will produce hysteresis loops for the corresponding aerodynamic coefficients in the pitch oscillatory motions because of the 90^o phase difference of the $\dot{\alpha}$ from α.

In principle, one can see, from these analyses, that the pitch moment generally has large $\dot{\alpha}(t)$ dependencies because the tail lift is the major force to generate the pitch moment while the lift has small $\dot{\alpha}(t)$ dependencies because the tail lift is just a small portion in the total lift of the aircraft. The $\dot{\alpha}(t)$ dependencies of drag are neglected in this analysis.

In the above, the $\dot{\alpha}(t)$ effects are modeled based on the corrections of the lift on the tail due to the lag of the downwash. The corresponding corrections are proportional to the values of the $\dot{\alpha}(t)$ and the delay of the downwash response, i.e., the time Δt it takes the flow from the C.G. of the aircraft to the tail mean aerodynamic center. In Refs. [1,2], the $\dot{\alpha}(t)$ derivatives are defined accordingly as,

$$\begin{aligned} \frac{\partial C_L}{\partial \dot{\alpha}} &= a_t \frac{l_t}{V} \frac{S_t}{S} \frac{\partial \epsilon}{\partial \alpha} \\ \frac{\partial C_m}{\partial \dot{\alpha}} &= -a_t V_H \frac{l_t}{V} \frac{\partial \epsilon}{\partial \alpha} \end{aligned} \tag{3.12}$$

These $\dot{\alpha}(t)$ derivatives are then included in the conventional stability derivative representation of aerodynamic characteristics to model the $\dot{\alpha}(t)$ effects. With the $\dot{\alpha}(t)$ effects added to Eq.(3.6), we have,

$$\begin{aligned} C_L &= C_L(\alpha) + C_{L_{\hat{q}}} q\hat{t} + C_{L_{\dot{\hat{\alpha}}}} \dot{\alpha}\hat{t} \\ C_D &= C_D(\alpha) + C_{D_{\hat{q}}} q\hat{t} + C_{D_{\dot{\hat{\alpha}}}} \dot{\alpha}\hat{t} \\ C_m &= C_m(\alpha) + C_{m_{\hat{q}}} q\hat{t} + C_{m_{\dot{\hat{\alpha}}}} \dot{\alpha}\hat{t} \end{aligned} \tag{3.13}$$

where the $C_{a_{\dot{\hat{\alpha}}}},\ a = L, D, or\ m$, are the corresponding aerodynamic derivatives with respect to the $\dot{\hat{\alpha}} = \dot{\alpha}\hat{t}$. $\hat{t}$ is the characteristic time of the flow which is defined in Eq.(3.7).

Based on the representation as given in Eq.(3.13), one can see that both the pitch rate $q(t)$ and the $\dot{\alpha}(t)$ will produce hysteresis loops of aerodynamic coefficients in the oscillatory pitch maneuvers since $q(t) = \dot{\alpha}(t)$ in the maneuvers and they both have a 90^o phase difference from the angle of attack $\alpha(t)$. Therefore, the hysteresis loops as shown in Figures 3.1, 3.2,

and 3.3 are the combinations of both the pitch rate $q(t)$ and the $\dot{\alpha}(t)$ effects. One can also see, from these figures, that the hysteresis loops of the pitch moment coefficients in the pitch oscillations are large because of its relatively large pitch rate and $\dot{\alpha}(t)$ dependencies. The hysteresis loops of the lift coefficients are small because of the small pitch rate and $\dot{\alpha}(t)$ dependencies. One can not see a obvious hysteresis loop of the drag coefficient in the pitch oscillations. That is because the corresponding pitch rate and $\dot{\alpha}(t)$ dependencies are negligibly small.

The above discussions are based on the assumption of the steady-state aerodynamics. As we pointed out, however, the $\dot{\alpha}(t)$ effects owe their existence to the fact that the pressure distribution on the aircraft does not adjust itself instantaneously to its equilibrium value when the angle of attack is suddenly changed. This effect totally involves unsteady aerodynamic characteristics. In this respect, the $\dot{\alpha}(t)$ effects are very different from those of the pitch rate which can be well determined on the basis of the steady-state aerodynamics. The analysis of the $\dot{\alpha}(t)$ derivatives discussed above neglects entirely the nonstationary character of the lift responses to the changes in angle of attack. It only gives out an estimate of this effect qualitatively. In unsteady flight conditions, the aerodynamic forces and moment are strictly speaking functionals of some state variables. Their dependencies on these state variables are not only on the instantaneous flight conditions but on their entire past histories. They contain the information required for the determination of the instant and future values of the aerodynamic characteristics. Therefore, it is advisable to develop a state-space model to describe the unsteady aerodynamics for general flight conditions as follows,

$$\begin{aligned} \frac{dx(t)}{dt} &= f(x, \alpha, q) \\ C_a(t) &= g(x, \alpha, q) \end{aligned} \tag{3.14}$$

where $a = L,\ D$, or m.

In Eq.(3.14), $x(t)$ is the state variable which contains all the information about the entire

past histories of the flows, $\alpha(t)$ and $q(t)$ are input variables which describe the flight conditions, and $C_a(t)$ are aerodynamic coefficients which are the outputs of this aerodynamic system.

For the oscillatory maneuvers in pitch, the information of the adjustment of the pressure distribution on the aircraft, or the lag of the downwash at the tail, due to the changes of the angle of attack, is contained in the state variable $x(t)$. The aerodynamic coefficients are then determined by this state variable and the the instant values of the input variables $\alpha(t)$ and $q(t)$.

Furthermore, this state-space representation can be extended to the high angle of attack regime where the separated and vortex flows are developed. In such flow conditions, the traditional stability derivative approach can not be used if valid results are to be obtained. For the state-space representation, however, the information of the flow separation and vortex bursting is contained in the state variables. The corresponding aerodynamic coefficients can then be determined by the state variables and the input variables. We will develop a state-space model to describe the unsteady aerodynamics in the following chapters.

3.1.4 Nondimensional Analysis of Hysteresis Loops

In the above, we provided some insights into the mechanisms of the hysteresis loops of the aerodynamic coefficients in the pitch oscillatory maneuvers. It was seen that the pitch rate $q(t)$ and the $\dot{\alpha}(t)$ effects are responsible for these loops. In this section, we are going to study some nondimensional quantities which can characterize these hysteresis loops. Since the hysteresis loops of the lift and drag coefficients are small, we will focus on those of the pitch moment coefficients in the analysis.

The descriptions of the pitch oscillatory motions are given by Eq.(2.1) in Chapter 2. As one can see that the motions are characterized by the amplitudes α_A and the frequencies ω for fixed mean angles of attack α_0. The testing conditions include the tunnel speed V. In general, people use the reduced frequency $\hat{\omega}$ to characterize these harmonic oscillatory motions, i.e.,

$$\hat{\omega} = \frac{\omega c}{2V} \tag{3.15}$$

As one can see, however, the reduced frequency $\hat{\omega}$ defined above does not contain any information about the amplitude of the oscillation. Since the pitch rate in the oscillation depends not only on the frequency but also on the amplitude, the amplitude information should be taken into account in characterizing the unsteady aerodynamic effects in the pitch oscillations. In the current research, we use the normalized maximum pitch rate $\hat{q}_{max}$ or normalized maximum derivative of angle of attack $\hat{\dot{\alpha}}_{max}$ as nondimensional quantity characterizing the pitch oscillations. Thus, in pitch oscillatory maneuvers, we have

$$\begin{aligned} \hat{q}_{max} &= \hat{\dot{\alpha}}_{max} \\ &= \hat{\omega}\alpha_A \\ &= \frac{c}{2V}\omega\alpha_A \end{aligned} \tag{3.16}$$

Therefore, for the maneuvers with the same nondimensional quantity $\hat{q}_{max}$, the corresponding aerodynamic coefficients will show the same aerodynamic characteristics through the hysteresis loops. Before we can show the performance of this nondimensional quantity, we need to properly define and express the characteristics of hysteresis loops in the oscillations.

From the previous analysis about the mechanism of hysteresis loops, we know that the hysteresis loops are the results of the dynamic delays of aerodynamic characteristics from the static values at the corresponding angle of attack, due to the unsteady motions. Therefore, the maximum offsets of the hysteresis loops from the static curves of the corresponding aerodynamic coeffcients can be used to characterize these unsteady flow effects in the oscillations. Thus, for the oscillatory maneuvers in pitch with the same $\hat{q}_{max}$, the maximum offsets of the corresponding hysteresis loops from the static curves of aerodynamic coefficients are expected to be the same, and the shapes of these hysteresis loops are also expected to be similar. These discussions can further be elaborated through the plots of the experimental results.

Tables 3.1 through 3.3 list some typical pitch oscillatory maneuvers in current wind-tunnel tests, associated with the corresponding values of $\hat{q}_{max}$. The maneuvers with amplitude 5 degrees are listed as group A in table 3.1 while the maneuvers with amplitudes 7.07 degrees and 10 degrees are listed as group B and group C in Table 3.2 and 3.3, respectively. Thus the amplitudes of the oscillations are the same in each group of maneuvers listed in the tables. Then each table includes several maneuver sets, each of which contains two maneuvers with same amplitude, frequency and tunnel speed but different mean angles of attack. One is about the mean angle of attack of zero degrees, and the other about the mean angle of attack of 24 degrees. We will first look at the maneuvers with same $\hat{q}_{max}$ in each individual group where the amplitudes are constant. Then we will investigate the maneuvers with same $\hat{q}_{max}$ in all these groups where the amplitudes can be different from maneuver to maneuver.

Table 3.1: Pitch Oscillatory Maneuvers: Group A ($\alpha_A = 5^o$)

Maneuvers	**Mean AOA**	**Frequency**	**Amplitude**	**Speed**	$\hat{q}_{max} \times 10^3$
A_1	$0^o, 24^o$	0.707 Hz	5^o	95 ft/s	1.6031
A_2	$0^o, 24^o$	0.707 Hz	5^o	67 ft/s	2.2730
A_3	$0^o, 24^o$	1.0 Hz	5^o	95 ft/s	2.2730
A_4	$0^o, 24^o$	1.0 Hz	5^o	67 ft/s	3.2064
A_5	$0^o, 24^o$	1.414 Hz	5^o	95 ft/s	3.2064
A_6	$0^o, 24^o$	1.414 Hz	5^o	67 ft/s	4.5338

Table 3.2: Pitch Oscillatory Maneuvers: Group B ($\alpha_A = 7.07^o$)

Maneuvers	**Mean AOA**	**Frequency**	**Amplitude**	**Speed**	$\hat{q}_{max} \times 10^3$
B_1	$0^o, 24^o$	0.5 Hz	7.07^o	95 ft/s	1.6030
B_2	$0^o, 24^o$	0.5 Hz	7.07^o	67 ft/s	2.2730
B_3	$0^o, 24^o$	0.707 Hz	7.07^o	95 ft/s	2.2730
B_4	$0^o, 24^o$	0.707 Hz	7.07^o	67 ft/s	3.2064
B_5	$0^o, 24^o$	1.0 Hz	7.07^o	95 ft/s	3.2064
B_6	$0^o, 24^o$	1.0 Hz	7.07^o	67 ft/s	4.5338
B_7	$0^o, 24^o$	1.414 Hz	7.07^o	95 ft/s	4.5338
B_8	$0^o, 24^o$	1.414 Hz	7.07^o	67 ft/s	6.4108

In group A, one can see, from Table 3.1, that the maneuver set A_2 has same value of the nondimensional quantity $\hat{q}_{max}$ as the maneuver set A_3, and also the A_4 has same $\hat{q}_{max}$ as the A_5. If the $\{A_i, A_j, ..., \} \in \hat{q}_{max}$ is used to denote the sets A_i, A_j, ..., having a value of the nondimensional quantity $\hat{q}_{max}$, then in group A, we have

$$\{A_2, A_3\} \in 0.00227, \qquad \{A_4, A_5\} \in 0.00321 \tag{3.17}$$

As we discussed above, each maneuver in {...} will have same unsteady aerodynamic characteristics in the pitch oscillations since they have same nondimensional characteristic quantity $\hat{q}_{max}$. In other words, the hysteresis loops of these maneuvers in the pitch oscillations will have same maximum offsets from the static curves of the corresponding aerodynamic coefficients. As an illustration, Figure 3.7 plots the hysteresis loops of the pitch moment coefficients for the maneuvers in sets A_4 and A_5, respectively. As one can see, from these

Table 3.3: Pitch Oscillatory Maneuvers: Group C ($\alpha_A = 10^o$)

Maneuvers	**Mean AOA**	**Frequency**	**Amplitude**	**Speed**	$\hat{q}_{max} \times 10^3$
C_1	$0^o, 24^o$	0.5 Hz	10^o	95 ft/s	2.2730
C_2	$0^o, 24^o$	0.5 Hz	10^o	67 ft/s	3.2064
C_3	$0^o, 24^o$	0.707 Hz	10^o	95 ft/s	3.2064
C_4	$0^o, 24^o$	0.707 Hz	10^o	67 ft/s	4.5338
C_5	$0^o, 24^o$	1.0 Hz	10^o	95 ft/s	4.5338
C_6	$0^o, 24^o$	1.0 Hz	10^o	67 ft/s	6.4127

plots, the hysteresis loops for the maneuvers in sets A_4 and A_5 not only have the same maximum offsets from the static curve, but also have almost the same shapes since the hysteresis loops of the corresponding maneuvers in these two sets nearly coincide with one another. These results show that the corresponding oscillatory maneuvers in sets A_4 and A_5 have the same unsteady aerodynamic characteristics because they have same nondimensional quantity $\hat{q}_{max}$. Similar plots can be obtained for the maneuvers in sets A_2 and A_3.

Similarly, by looking at the oscillatory maneuvers in groups B and C from Tables 3.2 and 3.3, respectively, we have,

$$\begin{aligned} &\{B_2, B_3\} \in 0.00227, \quad \{B_4, B_5\} \in 0.00321, \quad \{B_6, B_7\} \in 0.00453 \\ &\{C_2, C_3\} \in 0.00321, \quad \{C_4, C_5\} \in 0.00453 \end{aligned} \tag{3.18}$$

Figures 3.8 and 3.9 plot the hysteresis loops of the pitch moment coefficients for the oscillatory maneuvers in sets B_4 and B_5, and for the oscillatory maneuvers in sets C_2 and C_3, respectively. From Figure 3.8, one can see that the hysteresis loops of the oscillatory maneuvers in set B_4 almost coincide with those of the corresponding maneuvers in set B_5. It can also be observed from Figure 3.9 that the hysteresis loops of the oscillatory maneuvers in set C_2 nearly coincide with those of the corresponding maneuvers in set C_3. The similar plots can also be obtained for maneuver sets $\{B_2, B_3\}$, $\{B_6, B_7\}$ and $\{C_4, C_5\}$.

In summary, the hysteresis loops of the pitch oscillatory maneuvers in each group given in Tables 3.1 through 3.3 are going to be same if the corresponding maneuvers have same values of the nondimensional quantity $\hat{q}_{max}$. In such a case, these maneuvers have not only the same aerodynamic characteristics, but also the same time histories of the aerodynamic coefficients. These results are obtained from the oscillatory maneuvers in each individual group whose maneuvers have same amplitude in the oscillations. However, if the amplitudes of the oscillations are different, the associated hysteresis loops can't coincide with one another because the motion time histories are different. Since the unsteady aerodynamics in the pitch oscillations are characterized by the dynamic delays of the aerodynamic coefficients from the corresponding static values, these delay effects could still be the same even if the individual time histories of the aerodynamic coefficients are different. As we discussed before, the maximum offsets of the hysteresis loops from the corresponding static curves characterize these dynamic delay effects. Therefore, we expect the maximum offsets of the hysteresis loops to be the same for the maneuvers which have different amplitudes but same nondimensional quantity $\hat{q}_{max}$ in the oscillations.

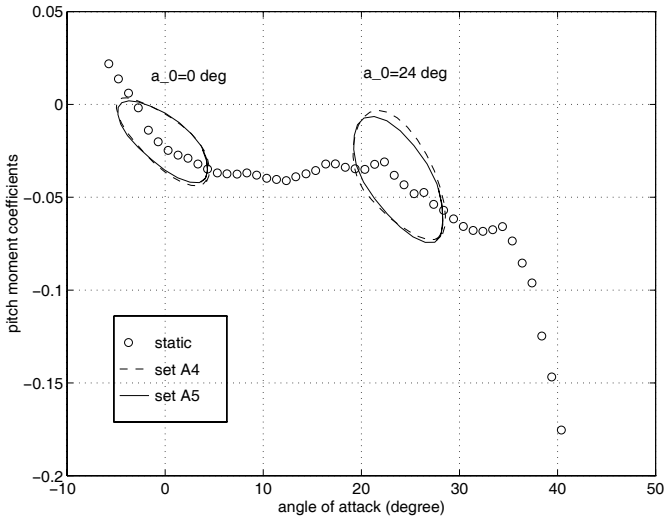

Figure 3.7: Hysteresis loops for maneuvers in sets A_4 and A_5

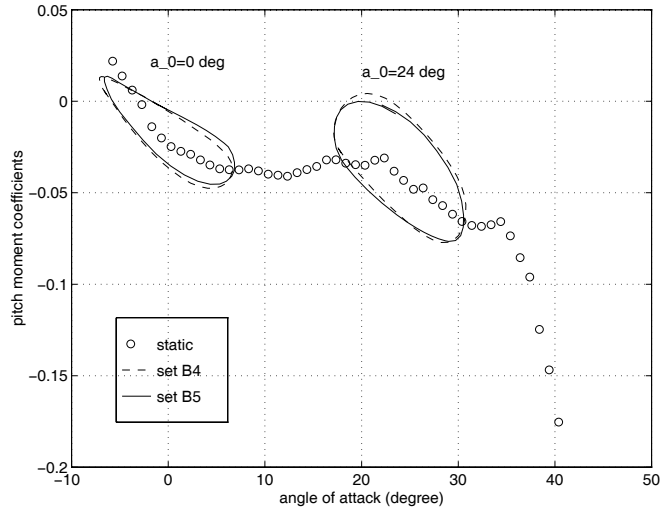

Figure 3.8: Hysteresis loops for maneuvers in sets B_4 and B_5

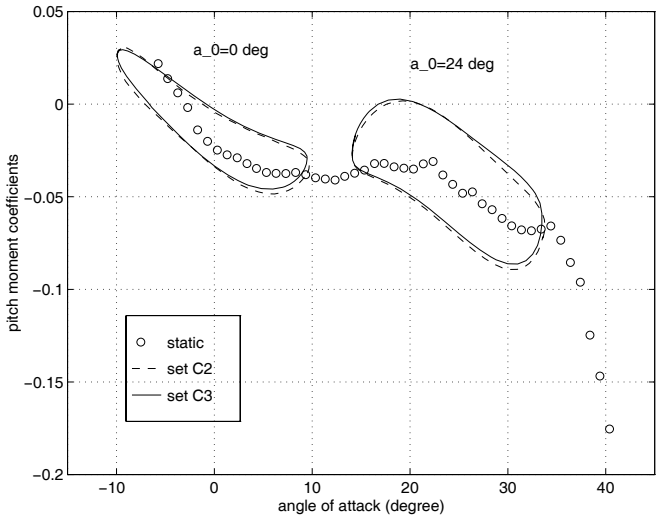

Figure 3.9: Hysteresis loops for maneuvers in sets C_2 and C_3

From Tables 3.1 through 3.3, the oscillatory maneuvers with same values of $\hat{q}_{max}$ in groups $A,\ B$, and C can be put as follows,

$$\begin{aligned}
&\{A_1,\ B_1\} \in 0.00160 \\
&\{A_2,\ A_3,\ B_2,\ B_3,\ C_1\} \in 0.00227 \\
&\{A_4,\ A_5,\ B_4,\ B_5,\ C_2,\ C_3\} \in 0.00321 \\
&\{A_6,\ B_6,\ B_7,\ C_4,\ C_5\} \in 0.00453 \\
&\{B_8,\ C_6\} \in 0.00641
\end{aligned} \tag{3.19}$$

The hysteresis loops of the oscillatory maneuvers in $\{A_4,\ A_5\}$, $\{B_4,\ B_5\}$, and $\{C_2,\ C_3\}$ have been shown in Figure 3.7, Figure 3.8, and Figure 3.9, respectively. From Eq.(3.19), one can see that all the maneuvers in these three sets have the value of nondimensional quantity $\hat{q}_{max}$ as 0.00321 but the amplitudes are different in each of these three sets. To show the unsteady aerodynamic effects for maneuvers of different amplitudes, we plot the hysteresis loops of the oscillatory maneuvers in set $\{A_4,\ B_4,\ C_2\}$ in Figure 3.10.

From Figure 3.10, one can see that the hysteresis loops of the maneuvers in sets A_4, B_4, and C_2 are correspondingly tangential to one another at both the top and bottom points where the maximum offsets of the hysteresis loops from static curve occur. In such a case, the maximum offsets of the hysteresis loops from static curve are all the same, even though the hysteresis loops with small amplitude are totally contained in those with large amplitude. We say that the hysteresis loops of the maneuvers in sets A_4, B_4, and C_2 satisfy the tangential conditions. As we discussed above, the actual time histories of the aerodynamic coefficients are different in these maneuvers, but the unsteady aerodynamic characteristics are the same since the associated hysteresis loops have the same maximum offsets from static curve. These maximum offsets of the hysteresis loops define the size of the dynamic delays and adjustment of the flows due to the unsteady oscillatory motions.

We are going to show one more example for the tangential conditions. The hysteresis loops of the oscillatory maneuvers for another set $\{A_6,\ B_6,\ C_4\}$, corresponding to a larger value of $\hat{q}_{max}$ (0.00453), are plotted in Figure 3.11. From the plots, one can see that the tangential conditions discussed above are still true, i.e., the hysteresis loops of the maneuvers are correspondingly tangential to one another at both the top and bottom points where the maximum offsets of the hysteresis loops from static curve occur. However, one can observe a small displacement from the tangential conditions for the hysteresis loops corresponding to the mean angle of attack of 24^o. Based on this observation, our conclusion is that the tangential conditions discussed above hold for the unsteady flows at low angles of attack. For the unsteady flows at high angles of attack, especially with large value of $\hat{q}_{max}$, this condition is expected to be verified by further experimental results.

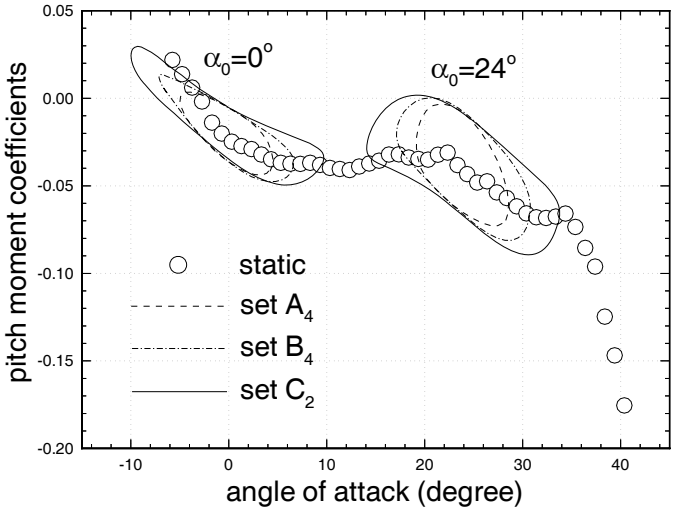

Figure 3.10: Hysteresis loops for maneuvers in sets A_4, B_4 and C_2

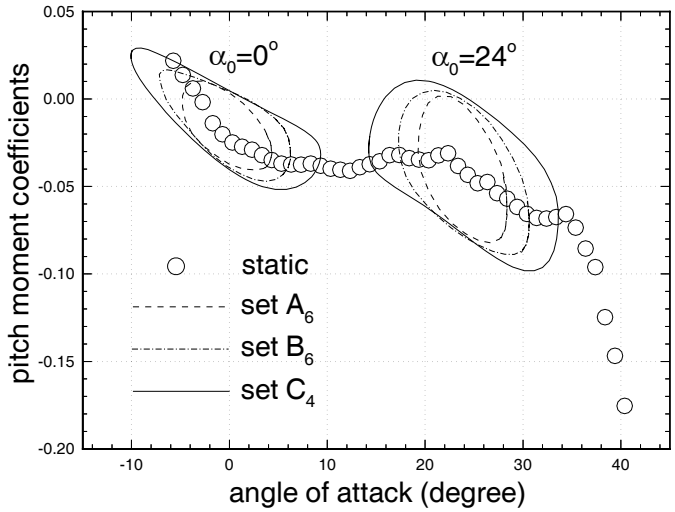

Figure 3.11: Hysteresis loops for maneuvers in sets A_6, B_6 and C_4

The tangential conditions discussed above imply a result that might be worth further discussion. From the pattern of the hysteresis loops satisfying this condition, we know that all these loops are tangential to one another at both the top and bottom points where the maximum offsets of the hysteresis loops from static curve occur. Based on this fact, if the reduced frequency $\hat{\omega}$ of the oscillation is decreased, the corresponding amplitude α_A has to be increased so that $\hat{q}_{max} = \hat{\omega}\alpha_A$ is still a constant. In this case, the resulting hysteresis loops will be stretched along the static curve in both directions as illustrated in Figure 3.12. If the reduced frequency is increased, however, the α_A has to be decreased accordingly. In such a case, the resulting hysteresis loops will be compressed along the static curve also in both directions. In the limit of this case, if the aircraft is oscillated at a small amplitude but very high frequency, the resulting pitch moment coefficient will jump up and down between the two tangential points at the top and bottom as shown in Figure 3.12.

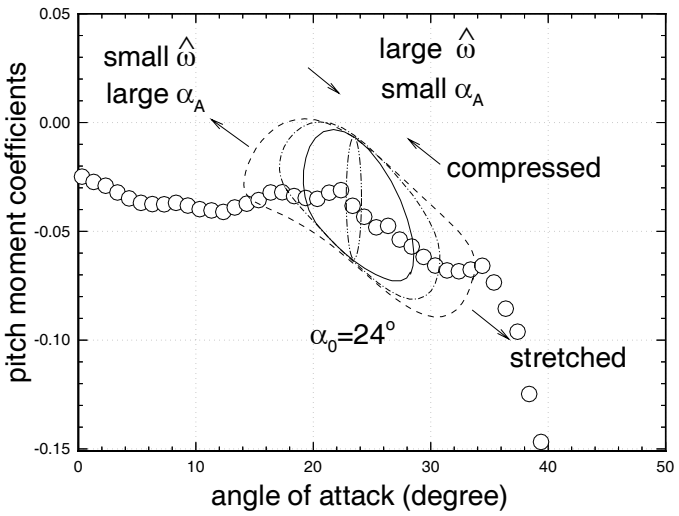

Figure 3.12: Hysteresis loop pattern

The next topic we are going to discuss is the reduced frequncy $\hat{\omega}$. As we mentioned before, the reduced frequency $\hat{\omega}$ does not contain any information about the amplitudes of the oscillations, so that it is not sufficient to characterize the unsteady aerodynamics for these oscillatory maneuvers.

From Tables 3.1 through 3.3, one can see that the oscillatory maneuvers in sets A_4, B_6, and C_6 have same value of the reduced frequency $\hat{\omega} = 0.0367$ but their $\hat{q}_{max}$ are different because their amplitudes are not the same. Figure 3.13 plots the hysteresis loops associated with these oscillatory maneuvers. From the plots, one can see that for the hysteresis loops corresponding to large amplitudes, the associated maximum offsets from the static curves are large, while for the hysteresis loops corresponding to small amplitudes, the maximum offsets are small. These results suggest that the dynamic delays and adjustment of the flows due to the unsteady oscillatory motions are different in these flowfields. Therefore, the associated unsteady aerodynamic characteristics are also different.

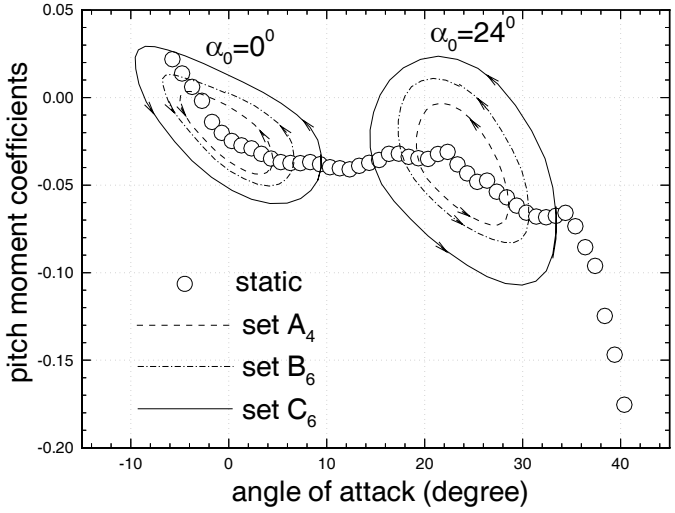

Figure 3.13: Hysteresis loops for maneuvers in sets A_4, B_6, and C_6

The last issue we are going to address is the direction of the loops. From their time histories, we identify that all these hysteresis loops are going in the counterclockwise direction as shown in Figure 3.13. The algebraic signs of the aerodynamic derivatives: $C_{m\hat{q}} + C_{m\dot{\hat{\alpha}}}$ are responsible for the loop direction. The reasons can be explained are as follows.

Assume that the aerodynamic coefficients can be represented by the stability derivative formulation given in Eq.(3.13). Thus the pitch moment coefficient can be written as,

$$C_m = C_m(\alpha) + C_{m\hat{q}} q\hat{t} + C_{m\dot{\hat{\alpha}}} \dot{\alpha}\hat{t} \tag{3.20}$$

As we know, for sinusoidal oscillations, if we plot the rate $\dot{\alpha}(t)$ versus the angle of attack $\alpha(t)$, we will get a clockwise loop because this plot is equivalent to the that of $cos(\omega t)$ vs $sin(\omega t)$, or $-sin(\omega t)$ vs $cos(\omega t)$. If we plot negative rate $-\dot{\alpha}(t)$ versus the angle of attack $\alpha(t)$, however, the loop direction will be reversed to the counterclockwise direction. As a result of this fact, if the aerodynamic derivative $C_{m\hat{q}} + C_{m\dot{\hat{\alpha}}}$ in Eq.(3.20) is negative, the resulting hysteresis loops in the pitch oscillations ($q = \dot{\alpha}$) are in the counterclockwise directions. The experimental results as shown in Figure 3.13 suggest that the aerodynamic derivative $C_{m\hat{q}} + C_{m\dot{\hat{\alpha}}}$ be negative.

3.2 Harmonic Oscillatory Maneuvers in Plunge

In the last section, we discussed, in detail, the experimental results for harmonic oscillatory maneuvers in pitch where both the pitch rate $q(t)$ and the $\dot{\alpha}(t)$ effects are applied. In this section, we are going to illustrate some typical experimental results for harmonic oscillatory maneuvers in plunge where only the $\dot{\alpha}(t)$ effects are applied. Then we compare the results with those of harmonic oscillatory maneuvers in pitch and briefly discuss the differences.

Figure 3.14 plots the aerodynamic coefficients for the plunge oscillatory maneuvers with the amplitude of 0.5 ft, the frequency of 1.5 Hz for two mean angles of attack of 0^o and 24^o at the tunnel speed of 67 ft/s.

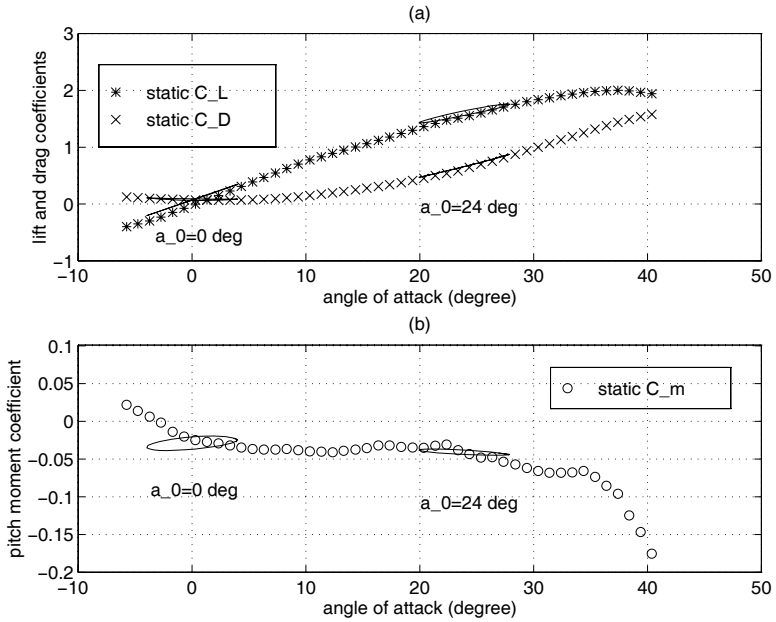

Figure 3.14: Aerodynamic coefficients for plunge oscillatory maneuvers with $h_A = 0.5\ ft, f = 1.5\ Hz$ at the tunnel speed of V=67 ft/s

From Figure 3.14 (a), one observed no significant hysteresis loops for the lift and drag coefficients except for the small loop of lift coefficient at mean angle of attack of 24 degrees. From Figure 3.14 (b), one can see relatively large hysteresis loop in the pitch moment coefficient at zero mean angle of attack. The mechanism responsible for these $\dot{\alpha}$ effects has been discussed in previous section. At mean angle of attack of 24 degrees, however, the associated hysteresis loop of pitch moment coefficient becomes small. This result can not be explained at this time and we don't have other experimental results to verify this observation.

3.3 Brief Summary and Aerodynamic Modeling

In last two sections, we pesented some typical experimental data of the harmonic oscillatory tests obtained in Chapter 2, and discussed the associated unsteady aerodynamic characteristics. Two types of the unsteady aerodyanmic effects are involved in these harmonic oscillatory tests, i.e., the $\dot{\alpha}$ effects and the $q(t)$ effects. As we pointed out, the $\dot{\alpha}(t)$ effects owe their existence to the fact that the pressure distribution on the aircraft does not adjust itself instantaneously to its equilibrium value when the angle of attack is suddenly changed. This effect totally involves unsteady aerodynamic characteristics. The previous analysis of the $\dot{\alpha}(t)$ derivatives neglects entirely the nonstationary character of the lift responses to the changes in angle of attack, so that the unsteady aerodynamic characteristics are not modeled.

The pitch rate $q(t)$ effects can be well-determined by the associated stability derivatives on the basis of the steady-state aerodynamics. However, at high angles of attack where separated and vortex flows are developed, the stability derivative representation can not be used. The values of the unsteady derivatives are found to be strongly dependent on the amplitude and frequency of aircraft oscillations[3].

In summary, properly modeling of the unsteady aerodynamic characteristics up to high angle of attack regime is highly desirable. In the next chapter, we are going to develop a state-space representation to describe the unsteady aerodynamics up to high angle of attack regime on the basis of the unsteady wind-tunnel measurements. Since the current harmonic oscillatory tests do not cover the high angle of attack regime, we need some other unsteady aerodynamic data including high angles of attack to generate such a model. Therefore the following unsteady aerodynamic data up to and beyond the stall range are selected from the references for the present aerodynamic modeling.

3.4 Lift Coefficient Data for an Airfoil Pitching at Constant Rate

The wind-tunnel studies of dynamic stall for an NACA 0015 airfoil pitching about the midchord at a constant rate were reported by Jumper, *et al*[18−19]. They studied the flowfields of the airfoil from attachment to separation and determined the lift and pitch moment coefficients as functions of angle of attack for 100 test cases, covering 20 dynamic airspeed and pitch rate combinations. Their results showed that there are significant delays of the stall and the magnitude of the maximum lift coefficient from the static values for the ramping airfoil. These delays are found to be proportional to the variation of the angle of attack for fixed freestream velocity. Typical lift-curve characteristics for this ramping airfoil at various pitch rates are shown in Figure 6.1 in Chapter 6.

3.5 Normal Force Coefficients for an Oscillating Delta Wing

Figure 6.6 in Chapter 6 plots the normal force coefficients of a 70^o delta wing oscillating in pitch, which are reported by Brandon[30]. From the plots, it is observed that, different from the oscillatory tests discussed above, the normal forces also show the significant hysteresis loops. This result occurs because Brandon's tests were conducted at high angles of attack where there are vortex development and breakdown on this oscillating wing. The fluid-mechanical processes that are causing these hysteresis loops are the dynamic lags of delta wing vortex build-up and breakdown in the high-rate/large-amplitude pitch oscillations.

For the flowfields on a swept delta wing, a central feature of the vortex formation from a swept leading edge at finite incidence angle is the vortex core. At a sufficiently high

angle of attack, this core breaks down, causing loss of local lift. For stationary wings, the location of vortex breakdown x_b, defined as the distance from the apex of the wing at which the vortex core diameter abruptly increases, attains its minimum value at maximum angle of attack, and conversely. A full description of these and other features, as well as a synopsis of theoretical development pertaining to flows past wings and analogous internal tube flows, was given by Wedemeyer[24].

3.6 Wind-tunnel Results for an F-18 Aircraft in Ramp Motions

Brandon[30] investigated and publishes the unsteady aerodynamic behaviors for an F-18 aircraft in ramp motions up to high angle of attack regime. The test configuration incorporates a moderately swept wing with a highly swept leading-edge extension (LEX) which generate concentrated vortical flowfields similar to those of a delta wing. In addition to the vortical flowfields, the aircraft also incorporates moderately swept wings and tail surfaces which can create separation flows over the configuration. These two types of flowfields can interact each other. In such a hybrid flowfield, both the separation and vortex burst phnomena exist. His experiments were conducted at such flow conditions.

The lift, drag and pitch moment coefficients from the static test and unsteady tests of ramp motions up to high angles of attack for this aircraft are plotted in Figures 6.10 through 6.15.

The static results show that the flowfield over the model at high angles of attack is dominated by a strong vortex system generated by the LEX. This vortex system contribute both to increased lift and reduced pitch stability. Development of the LEX vortex system starts at very moderate angles of attack. At these conditions, the vortex system trails over

the wing and passes just outboard of the vertical tails. With increasing angle of attack, breakdown of the vortices progresses forward such that the burst point moves over the wing and LEX, associated with a substantial decrease in lift and a substantial increase in pitch stability.

For the flow structures observed in the static test, the dynamic tests using constant pitch rate motions show the effects of the pitch rate and the persistence of the unsteady aerodynamic effects. For the aircraft pitching up at constant rate, an increase in lift coefficient due to pitch rate over entire range of motion has been observed and the maximum increment of the lift coefficient occurred beyond the angle of attack for maximun lift at the static test. A number of factors must be responsible for these observations. The dominant one is the flow lag associated first with flow separation and vortex formation at the low angles of attack, and then with vortex breakdown at the higher angles of attack.

For the aircraft pitching down at constant rate, the flow condition on the model was characterized by complete flow separation and vortex breakdown at beginning. During the pitch-down motion, the formation of the LEX vortex system lags in comparison to the static case and reattachment of the wing flow is delayed. This result causes large decreases in lift coefficient due to the motion. As pitch rate is increased, the loss in lift increases due to the lags in vortex development and wing flow reattachment. All these unsteady aerodynamic characteristics are expected to be properly modeled.

Chapter 4

Unsteady Aerodynamic Model

In previous chapters, we described various types of the unsteady aerodynamic data for several configurations, including an NACA 0015 airfoil, a 70^o delta wing, and F-18 configurations. The associated unsteady aerodynamic characteristics were also discussed. In this chapter, we are going to develop an aerodynamic model in the form of Eq.(3.14) to describe the unsteady aerodynamics on the basis of the unsteady aerodynamic data obtained.

Determining and describing the aerodynamic forces and moments on an aircraft is a very important subject in atmospheric flight mechanics. It is primarily this aerodynamic ingredient that distinguishes flight mechanics from other branches of mechanics. As we discussed in previous chapters, the conventional stability derivative description neglects entirely the nonstationary character of the aerodynamic responses to the changes in angle of attack, so that it is many times questioned based on studies of the unsteady aerodynamics, especially at high angle of attack region where separated and vortex flows are presented. In general unsteady flight conditions, the aerodynamic forces and moments are strictly speaking functionals of some state variables associated with flight conditions. These variables are dependent not only on the instantaneous flight conditions but on their entire past histories. They contain the information about the flowfields required for the determination of

the instant and future values of the aerodynamic characteristics. Based on these points, we are going to develop a state-space representation to describe the unsteady aerodynamics up to the high angle of attack regime.

To illustrate the possibility of generating a valid state-space model, simple examples will be considered. The first example is the unsteady flow about an airfoil with trailing-edge separation. The second is the unsteady flows about a slender delta wing with vortex breakdown. On the basis of these examples, the structures of the approximate state-space model is proposed to describe the unsteady aerodynamics for an aircraft.

4.1 State Equation for Separated Flows

Most wings of conventional aircraft have a rough airfoil with a turbulent boundary layer. On these airfoils, flow separation mainly begins at the trailing edge, and moves to the leading edge as angle of attack is increased. This form of flow separation is valid for relatively slow variations of the angle of attack. In such a flow, a nondimensional coordinate $x \in [0, 1]$ can be introduced to describe the position of the separation point on the airfoil surface. The value $x = 1$ corresponds to fully attached flow, while $x = 0$ corresponds to complete flow separation. In Ref. [13], the x is taken as a state variable for the separated flow and the following first order differential equation is used to describe the movement of the separation point in unsteady flow conditions:

$$\tau_1 \frac{dx}{dt} + x = x_0(\alpha_{eff}) \tag{4.1}$$

where $x_0(\alpha)$ is the static state dependency of the separation point on the angle of attack, and α_{eff} is an effective angle of attack which gives an equivalent static state value of angle of attack to locate the separation position. Including the time delay due to the quasi-steady

aerodynamic effects, α_{eff} is formulated as[13],

$$\alpha_{eff}(t) = \alpha(t) - \tau_2 \dot{\alpha}(t) \tag{4.2}$$

In above equations, parameter τ_2 defines the total time delay of the flow separation and reattachment due to the quasi-steady aerodynamic effects such as the circulation and boundary-layer convection lags. τ_1 is the relaxation time constant which defines the transient aerodynamics effects, i.e., dynamic properties of the separated flow adjustment when a flow condition is changed.

To apply Eq. (4.1), we have to know the driving function $x_0(\alpha)$. The steady state position of separation point is generally a nonlinear function of angle of attack. In Ref. 26], this function $x_0(\alpha)$ is suggested to be obtained from static wind tunnel measurements. But in order to be applicable for identification purposes, here in present research, we use an inverse exponential function with two parameters to approximate it, that is, we assume the following function for $x_0(\alpha)$:

$$x_0(\alpha) \triangleq \frac{1}{1 + e^{\sigma(\alpha - \alpha_s)}} \tag{4.3}$$

Eq. (4.3) defines a family of continuous functions with two parameters: (α_s, σ) where α_s is the angle of attack at which the flow separation is at the mid-chord point, and σ is the slope factor. A family of the flow separation functions with variation of σ for fixed $\alpha_s = 20^o$ is shown in Fig. 4.1, from which one can see that by changing α_s, the function shown in Figure 4.1 can be shifted horizontally to the desired place while through the variation of σ, the slope of the function can be adjusted to the desired level.

Therefore, using this inverse exponential function, the separation characteristics of different airfoils can be approximated. α_s and σ are expected to be determined from wind tunnel experimental data.

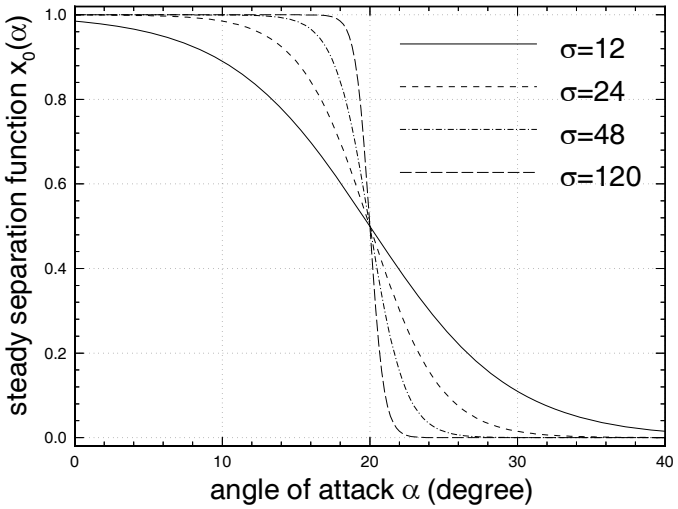

Figure 4.1: Flow separation function for $\alpha_s = 20^o$

The pitch rate effects on the flow separation are not modeled in previous work. Since the pitch rate q can change the local angle of attack along the chord length, the effective angle of attack defined in Eq.(4.2) needs to be adjusted. This pitch rate effect can be approximated by modifying the effective angle of attack as

$$\alpha_{eff}(t) = \alpha(t) - \tau_2\dot{\alpha}(t) - \tau_3 q(t)[\alpha(t) - \alpha_s] \tag{4.4}$$

where α_s is defined in Eq. (4.3). This modification approximately models the effects that pitch up (down) rate causes the local angle of attack to decrease (increase) along the length in front of rotation point and to increase (decrease) along the length behind this point. Thus, the dynamics of the separation point can still be modeled by the first-order system given in Eq.(4.1) with effective angle of attack $\alpha_{eff}(t)$ given in Eq. (4.4).

In Eqs. (4.1) and (4.4) , x is the state of the system, and α and q are input variables. This mathematical formulation can also be used to describe the unsteady flow of a 3-dimensional delta wing with vortex flows. As we know, the flow field over highly swept delta wing is

dominated by the presence of a strong leading-edge vortex system. When the angle of attack is increased from zero degrees, the leading-edge vortices begin to develop on the wing. As the angle of attack is further increased, the vortex burst point travels forward onto the wing, and moves towards the apex. When the vortex burst point reaches the apex of the wing, the flow field over the wing is characterized by fully separated flow. For such a flow pattern, we can also define a nondimensional coordinate $x \in [0, 1]$ to describe the vortex burst position. The movement of the vortex burst location at unsteady flow conditions can still be governed by the same first-order differential equation (4.1) with α_{eff} defined by Eq.(4.4).

4.2 Output Equations for Aerodynamic Coefficients

The drag, lift and pitch moment coefficients are the outputs of the system of interest. They are functions of state $x(t)$ and inputs: $\alpha(t)$ and $q(t)$.

$$\begin{aligned} C_D &= C_D(x, \alpha, q) \\ C_L &= C_L(x, \alpha, q) \\ C_m &= C_m(x, \alpha, q) \end{aligned} \tag{4.5}$$

For general configurations, these functions are not known. Certain practical schemes have to be developed so that using wind tunnel data, these relations can be approximated by a system identification method.

We still use Taylor series expansions of Eq. (4.5). In order to resemble the current approach of stability derivatives, however, we do the expansions in terms of α and q about the origin, while holding state x fixed. Take the lift coefficient as example. We can write,

$$\begin{aligned} C_L(x,\alpha,q) &= C_{L0} + (\frac{\partial C_L}{\partial \alpha})_0 \alpha + (\frac{\partial C_L}{\partial q})_0 q \\ &\quad + \frac{1}{2}[(\frac{\partial^2 C_L}{\partial \alpha^2})_0 \alpha^2 + (\frac{\partial^2 C_L}{\partial q^2})_0 q^2 + 2(\frac{\partial^2 C_L}{\partial \alpha \partial q})_0 \alpha q] + ... \end{aligned} \tag{4.6}$$

Since all the partial derivatives in Eq. (4.6) are evaluated at $(\alpha, q) = (0, 0)$, they only depend on state variable x. C_{L0} is the lift coefficient when α and q equal zero. At such conditions, the flow is generally attached. Therefore we can treat C_{L0} as a constant, independent of state variable x.

The classical assumption of linear aerodynamic theory[1] is to accept the linear reduction of Eq. (4.6) as a representation of the aerodynamic coefficient. This assumption works well for attached flows at low angles of attack, but at high angles of attack the terms up to second derivatives should generally be retained for sufficient accuracy. Here we include the quadratic terms in the representation of the aerodynamic coefficient for general use, even though we may use linear approximations for some special cases in present study.

$$C_L = C_{L0} + C_{L\alpha}(x)\alpha + C_{L\hat{q}}(x)\hat{q} + \Delta^2 C_L \tag{4.7}$$

where

$$\Delta^2 C_L \triangleq \frac{1}{2}[C_{L\alpha^2}(x)\alpha^2 + C_{L\hat{q}^2}(x)\hat{q}^2 + 2C_{L\alpha\hat{q}}(x)\alpha\hat{q}] \tag{4.8}$$

Here, $\hat{q} = q\hat{t}$ is the nondimensionalized pitch rate. $\hat{t}$ is the characteristic time of the flow, which is defined in Eq.(3.7).

In above equations, derivatives such as $C_{L\alpha}, C_{L\hat{q}}$ are still known as stability derivatives. But different from the conventional case, these derivatives are no longer constant. They depend on the state of flow separation, or vortex burst.

We know that all the derivatives in Eq. (4.7) are functions of state variable x, but these functions are still not explicitly known. In present study, we still resort to Taylor series expansion to derive an approximate representation of these derivatives for identification use.

Taking $C_{L\alpha}(x)$ as example, the expansion about some constant $\hat{a}, \in [0, 1]$ is,

$$C_{L\alpha}(x) = C_{L\alpha}(\hat{a}) + (\frac{\partial C_{L\alpha}}{\partial x})_{\hat{a}}(x - \hat{a}) + \frac{1}{2}(\frac{\partial^2 C_{L\alpha}}{\partial x^2})_{\hat{a}}(x - \hat{a})^2 + R_2(x) \tag{4.9}$$

where all the derivatives are evaluated at $x = \hat{a}$, and the the residual term $R_2(x)$ in the expansion is

$$R_2(x) = \frac{1}{6}(\frac{\partial^3 C_{L\alpha}}{\partial x^3})_{\hat{a}}[\xi(x) - \hat{a}]^3 \tag{4.10}$$

If the expansion is considered to be taken about $\hat{a} = \frac{1}{2}$, then we have

$$|[\xi(x) - \frac{1}{2}]^3| \leq (\frac{1}{2})^3 = \frac{1}{8} \tag{4.11}$$

and

$$|R_2(x)| \leq \frac{1}{48}|(\frac{\partial^3 C_{L\alpha}}{\partial x^3})_{\frac{1}{2}}| = 0.0208 C_3 \tag{4.12}$$

where constant C_3 is the magnitude of third derivative of $C_{L\alpha}(x)$ with respect to x, evaluated at $x = \frac{1}{2}$.

Under the assumption of existence of all derivatives in the expansion (4.9), the residual term $R_2(x)$ is bounded by Eq.(4.12). So if Eq. (4.9) is used as an approximation to $C_{L\alpha}(x)$ by neglecting the residual term $R_2(x)$, i.e.,

$$\begin{aligned} C_{L\alpha}(x) &= C_{L\alpha}(\hat{a}) + (\frac{\partial C_{L\alpha}}{\partial x})_{\hat{a}}(x-\hat{a}) + \frac{1}{2}(\frac{\partial^2 C_{L\alpha}}{\partial x^2})_{\hat{a}}(x-\hat{a})^2 \\ &= [C_{L\alpha}(\hat{a}) - (\frac{\partial C_{L\alpha}}{\partial x})_{\hat{a}}\hat{a} + \frac{1}{2}(\frac{\partial^2 C_{L\alpha}}{\partial x^2})_{\hat{a}}\hat{a}^2] \\ &\quad +[(\frac{\partial C_{L\alpha}}{\partial x})_{\hat{a}} - (\frac{\partial^2 C_{L\alpha}}{\partial x^2})_{\hat{a}}\hat{a}]x + \frac{1}{2}(\frac{\partial^2 C_{L\alpha}}{\partial x^2})_{\hat{a}}x^2 \\ &= a + bx + cx^2 \end{aligned} \tag{4.13}$$

the error is also bounded by Eq.(4.12). Furthermore, when this representation is used in identification process, the overall error can be minimized by choice of the coefficients a, b and c.

Another aspect of this representation is the interpretation of the coefficients: a, b and c. We know that $x = 1$ corresponds to attached flow while $x = 0$ corresponds to complete flow separation. If we write the polynominal in Eq.(4.13) in terms of $y = 1 - x$ instead of x, that is

$$\begin{aligned} C_{L\alpha} &= a_1 + b_1(1-x) + c_1(1-x)^2 \\ &= a_1 + b_1 y + c_1 y^2 \end{aligned} \tag{4.14}$$

then constant a_1 is exactly the lift coefficient slope of attached flow, corresponding to the value of the conventional stability derivative while b_1 and c_1 correspond to the contributions to the lift coefficient slope due to flow separation.

Variable y is actually a complementary version of variable x. Their relationship is

$$x + y = 1 \tag{4.15}$$

From Eq.(4.15), the complementary flow separation function $y_0(\alpha)$ dual to $x_0(\alpha)$ in Eq.(4.3) can be determined as,

$$\begin{aligned} y_0(\alpha) &= 1 - x_0(\alpha) \\ &= \frac{1}{1 + e^{-\sigma(\alpha - \alpha_s)}} \end{aligned} \tag{4.16}$$

Using this complementary flow separation variable, all the other aerodynamic derivatives can similarly be represented in terms of the following quadratic polynominals,

$$\begin{aligned} C_{L\hat{q}}(y) &= a_2 + b_2 y + c_2 y^2 \\ C_{L\alpha^2}(y) &= 2(a_3 + b_3 y + c_3 y^2) \\ C_{L\hat{q}^2}(y) &= 2(a_4 + b_4 y + c_4 y^2) \\ C_{L\alpha\hat{q}}(y) &= a_5 + b_5 y + c_5 y^2 \end{aligned} \tag{4.17}$$

where $a_i, i = 1, 2, ..., 5$ correspond to the values of the conventional stability derivatives for attached flow while b_i and $c_i, i = 1, 2, ..., 5$ are contributions to the corresponding stability derivatives due to flow separation. All these constants are to be determined from wind tunnel data.

Similar expressions can be derived for drag and pitch moment coefficients: C_D and C_m.

4.3 State-Space Representation

Using Eqs.(4.15) and (4.16), we can represent the dynamic equation (4.1) that governs the state of unsteady flow separation in terms of the complementary state variable $y(t)$. Using this state and inputs (α, q) we can obtain the aerodynamic coefficients as outputs from the above formulations.

Based on all these formulations, we propose the following state-space representation of unsteady aerodynamics at high angles of attack:

$$\begin{aligned}
&\tau_1 \frac{dy}{dt} + y = y_0(\alpha_{eff}) \\
&\alpha_{eff} = \alpha - \tau_2 \dot{\alpha} - \tau_3 q(\alpha - \alpha_s) \\
&C_D = C_{D0} + C_{D\alpha}(y)\alpha + C_{D\hat{q}}(y)\hat{q} + \Delta^2 C_D \\
&C_L = C_{L0} + C_{L\alpha}(y)\alpha + C_{L\hat{q}}(y)\hat{q} + \Delta^2 C_L \\
&C_m = C_{m0} + C_{m\alpha}(y)\alpha + C_{m\hat{q}}(y)\hat{q} + \Delta^2 C_m
\end{aligned} \tag{4.18}$$

where the complementary flow separation function $y_0(\alpha)$ is given by Eq.(4.16), and all the derivatives with respect to α and $\hat{q}$ are quadratic polynominals of y.

In the above state-space model, the unknown parameters in the dynamic equation are $\tau_1, \tau_2, \tau_3, \alpha_s, \sigma$. The unknown parameters in output equations are C_{D0}, C_{L0}, C_{m0}, and those quadratic polynominal coefficients in the aerodynamic derivatives. If the assumption of linear aerodynamic theory is used, the number of unknowns in determining each aerodynamic coefficient is 7. This number of unknowns, however, will increase to 16 if the second derivative terms are included. All these parameters are expected to be estimated from selected wind tunnel data.

Chapter 5

Parameter Identification Method

The state-space model given in Eq. (4.18) is valid for both static and unsteady flow conditions. The parameters in the model can be roughly divided into two groups. One group, like α_s, σ, determines the static characteristics of separation flow while the other group, like τ_1, τ_2 and τ_3, characterizes the dynamic properties of flow separation and reattachment. In order to make the model a good representation of aerodynamic characteristics at high angles of attack, we should use both static and unsteady wind tunnel data to identify these unknown parameters.

The identification method used here is the minimum mean-square error approach. We first define the the mean-square errors between the experimental data and model outputs as follows.

In the static case, suppose that for a given sequence of the angle of attack: $\alpha_i, i = 0, 1, 2, ..., l$, the wind tunnel measurements of aerodynamic coefficients at these points are

$$\{\hat{C}_D(\alpha_i), \hat{C}_L(\alpha_i), \hat{C}_m(\alpha_i), i = 0, 1, 2, ..., l\} \tag{5.1}$$

Using model (4.18), the static aerodynamic coefficients at corresponding angle of attack

for a set of assumed values of the unknown parameters can be obtained as:

$$\{C_D(\alpha_i), C_L(\alpha_i), C_m(\alpha_i), i = 0, 1, 2, ..., l\} \tag{5.2}$$

In such a case, the mean-square error between static sequences (5.1) and (5.2) can be defined as,

$$\epsilon_1 = \frac{1}{3}(\epsilon_{D1} + \epsilon_{L1} + \epsilon_{m1}) \tag{5.3}$$

where

$$\begin{aligned}
\epsilon_{D1} &\triangleq \frac{1}{l+1}\sum_{i=0}^{l}[C_D(\alpha_i) - \hat{C}_D(\alpha_i)]^2 \\
\epsilon_{L1} &\triangleq \frac{1}{l+1}\sum_{i=0}^{l}[C_L(\alpha_i) - \hat{C}_L(\alpha_i)]^2 \\
\epsilon_{m1} &\triangleq \frac{1}{l+1}\sum_{i=0}^{l}[C_m(\alpha_i) - \hat{C}_m(\alpha_i)]^2
\end{aligned} \tag{5.4}$$

Similarly, we can define the mean-square error between wind tunnel measurements and dynamic responses of the model at unsteady flow conditions.

Suppose that for given time histories of inputs at separation flow conditions:

$$\{\alpha(t), q(t), 0 \leq t \leq T\} \tag{5.5}$$

the corresponding wind tunnel measurements of aerodynamic coefficient time histories at sampling points are

$$\{\hat{C}_D(t_j), \hat{C}_L(t_j), \hat{C}_m(t_j), j = 0, 1, 2, ..., n\} \tag{5.6}$$

where $t_0 = 0 < t_1 < ... < t_j < t_{j+1} < ... < t_n = T$.

Using the input time histories (5.5), we can simulate the state-space model in Eq. (4.18) for the assumed values of the unknown parameters in the model. The responses of the outputs at the corresponding sampling points are expressed as,

$$\{C_D(t_j), C_L(t_j), C_m(t_j), j = 0, 1, 2, ..., n\} \tag{5.7}$$

The mean-square error between these two dynamic sequences are defined similarly as,

$$\epsilon_2 = \frac{1}{3}(\epsilon_{D2} + \epsilon_{L2} + \epsilon_{m2}) \tag{5.8}$$

where

$$\begin{aligned}
\epsilon_{D2} &\triangleq \frac{1}{n+1}\sum_{j=0}^{n}[C_D(t_j) - \hat{C}_D(t_j)]^2 \\
\epsilon_{L2} &\triangleq \frac{1}{n+1}\sum_{j=0}^{n}[C_L(t_j) - \hat{C}_L(t_j)]^2 \\
\epsilon_{m2} &\triangleq \frac{1}{n+1}\sum_{j=0}^{n}[C_m(t_j) - \hat{C}_m(t_j)]^2
\end{aligned} \tag{5.9}$$

In order to make the static and dynamic responses of the model match the corresponding wind tunnel data, we choose the unknown parameters in such a way that the sum of the mean-square errors for steady and unsteady flow conditions is minimized:

$$\epsilon = \epsilon_1 + \epsilon_2 \tag{5.10}$$

where ϵ_1 and ϵ_2 are static and dynamic errors between experimental data and the proposed model, defined in Eq. (5.3) and (5.8), respectively. Such parameters that produce the minimum mean-square error are used as our identification results.

Chapter 6

Model Performance Validation

We are going to demonstrate the performance of the proposed model identified using wind tunnel measurements. Before we start the identification procedure, we have something to say about the identifiability of τ_3 effects in the model (4.18).

In wind tunnel experiments, we generally can not separate the pitch rate from the variation of angle of attack, that is, experiments are conducted at $q(t) = \dot{\alpha}(t)$. In such a case, the effects of τ_3 may not be separable from those of τ_2. We can show this result by the following.

Consider the argument $\alpha_{eff}(t)$ in the driving function y_0 in model (4.18). When $q(t) = \dot{\alpha}(t)$, we have,

$$\begin{aligned} \alpha_{eff} &= \alpha - \tau_2\dot{\alpha} - \tau_3 q(\alpha - \alpha_s) \\ &= \alpha - \tau_2\dot{\alpha} - \tau_3\dot{\alpha}(\alpha - \alpha_s) \\ &= \alpha - [\tau_2 + \tau_3(\alpha - \alpha_s)]\dot{\alpha} \\ &= \alpha - \hat{\tau}_2\dot{\alpha} \end{aligned} \tag{6.1}$$

where

$$\hat{\tau}_2 = \tau_2 + \tau_3(\alpha - \alpha_s) \tag{6.2}$$

In this case, the effective angle of attack in model (4.18) is actually of the form,

$$\alpha_{eff} = \alpha - \hat{\tau}_2 \dot{\alpha} \tag{6.3}$$

This equation appears to be equivalent to Eq. (4.2) except that $\hat{\tau}_2$ here is no longer a constant but a linear function of angle of attack. This observation suggests that the pitch rate effects enter the system in the same way as the variation of angle of attack. So using such wind tunnel data, the τ_3 effects may not be separable from those of τ_2. We are going to show this result in the following example.

6.1 Aerodynamic Model of an NACA 0015 Airfoil

In Chapter 3, we discussed the aerodynamic characteristics associated with the wind tunnel data[18] for an NACA 0015 airfoil pitching up at constant rates. Here we are going to use these data to identify the proposed model.

For this airfoil pitching up at constant rate, the input histories can be expressed as,

$$\begin{aligned} \alpha(t) &= \dot{\alpha} t, \quad 0 \leq \alpha(t) \leq 38^o \\ q(t) &= \dot{\alpha} \end{aligned} \tag{6.4}$$

where $\dot{\alpha}$ is constant.

The wind tunnel measurements[18] of lift coefficient for the static and four dynamic cases are shown as circle and square in Fig. 6.1, respectively. The wind tunnel data of drag and pitch moment coefficients for one dynamic case are shown as triangle for drag and diamond for pitch moment in Fig. 6.2.

Here we use the first derivative (linear) terms as representation of lift and pitch moment coefficients. For drag coefficient, we include one α^2 term.

Using the parameter identification procedure mentioned above, we obtain the unknown parameters of the proposed model in Eq. (4.18) as follows:

a. Parameters in Dynamic Equation

$$\begin{aligned} &\tau_1 = 1.071\hat{t}, \qquad &&\tau_2 = 6.781\hat{t} \\ &\tau_3 = 0.005\hat{t} \\ &\alpha_s = 18.391\ deg, \quad &&\sigma = 44.63 \end{aligned} \tag{6.5}$$

b. Expressions of Aerodynamic Coefficients

$$\begin{aligned} C_L &= -0.011 + C_{L\alpha}(y)\alpha + C_{L\hat{q}}(y)\hat{q} \\ C_D &= 0.039 + C_{D\alpha}(y)\alpha + 2.748\alpha^2 + C_{D\hat{q}}(y)\hat{q} \\ C_m &= 0.073 + C_{m\alpha}(y)\alpha + C_{m\hat{q}}(y)\hat{q} \end{aligned} \tag{6.6}$$

where α is in radians while σ is in per radian. The aerodynamic derivatives are

$$\begin{aligned} C_{L\alpha}(y) &= 3.443 - 3.124y + 1.377y^2 \\ C_{L\hat{q}}(y) &= 0.749 + 99.850y - 101.728y^2 \\ C_{D\alpha}(y) &= -0.179 - 4.297y + 3.796y^2 \\ C_{D\hat{q}}(y) &= -0.993 + 172.266y - 167.856y^2 \\ C_{m\alpha}(y) &= -0.014 - 7.918y + 6.471y^2 \\ C_{m\hat{q}}(y) &= -3.120 + 113.937y - 78.021y^2 \end{aligned} \tag{6.7}$$

Using the identification results given above, we can simulate the model for the flow conditions of interest. The corresponding responses are ploted as solid lines in Figures 6.1 and 6.2, respectively. From these plots, one can see that the model responses match the experimental data very well.

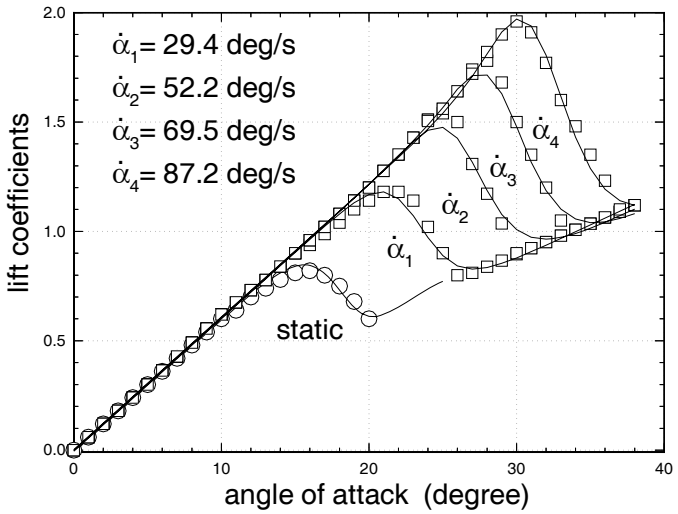

Figure 6.1: Static and dynamic lift coefficients of NACA 0015 airfoil

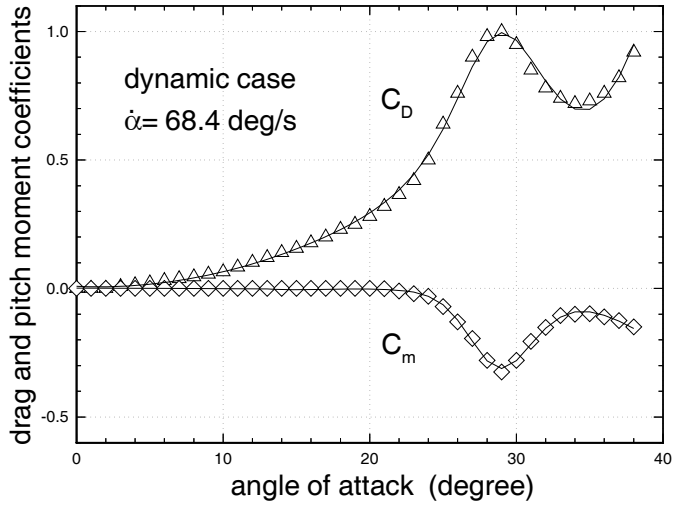

Figure 6.2: Dynamic drag and pitch moment coefficients of NACA 0015 airfoil

From the time constants given in Eq. (6.5), one can see that τ_2 is nearly 7 times as big as τ_1. This result means that for unsteady flow over this airfoil, the delay in flow separation and reattachment on the upper surface of the airfoil is a dominant phenomenon. The aerodynamic transient process is very short compared with this delay. τ_3 is very small compared with τ_1 and τ_2. This result means that $\hat{\tau}_2$ in Eq.(6.2), which defines the total time delay of flow separation, is nearly independent of angle of attack. In this sense, the pitch rate effects on the flow separation are not separable from those of variation of angle of attack by using these data. We will neglect the τ_3 term in the following discussions because of the data we are using.

For the aerodynamic derivatives given in Eq.(6.7), the constant terms correspond to the values of conventional stability derivatives for attached flow. One can see from Eq.(6.7) that this constant is 3.443 for the lift coefficient, corresponding to the lift curve slope of an NACA 0015 airfoil for attached flow. This value matches the wind-tunnel experimental result at low angles of attack as presented in Ref. [18]. At high angles of attack, however, where separated flow is developed, the values of unsteady derivatives are no longer constant. It depends on the complementary state variable y which is governed by a differential equation driven by the time histories of the motion. This effect can result in strong dependencies of the unsteady aerodynamic derivatives on the amplitude and frequency of the airfoil oscillations.

The time histories of the complementary state variable y associated with the ramp motion time histories given in Eq. (6.4) are plotted in Figure 6.3 from which one can see the dynamic lags of the separation flows. The corresponding lift coefficient derivatives are plotted as function of angle of attack for several pitch rates in Figure 6.4 for $C_{L_\alpha}(y)$ and in Figure 6.5 for $C_{L_{\hat{q}}}(y)$. From the figures, one can view the dependencies of unsteady aerodynamic derivatives on motion time histories.

Similar results can be shown for drag and pitch moment coefficients.

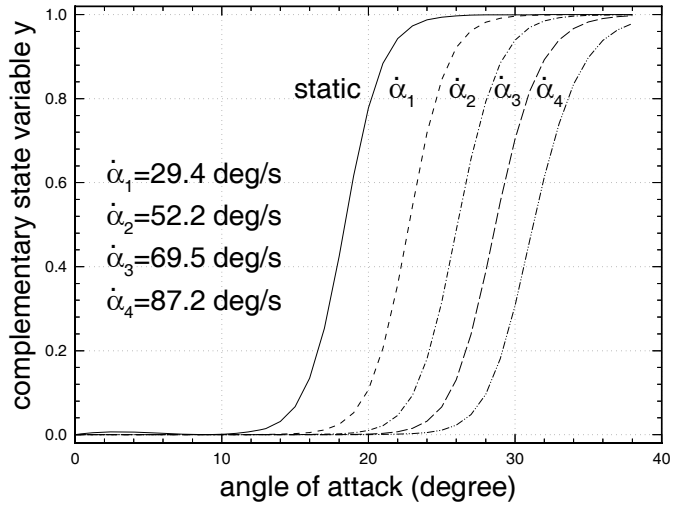

Figure 6.3: Complementary state variables y of NACA 0015 airfoil

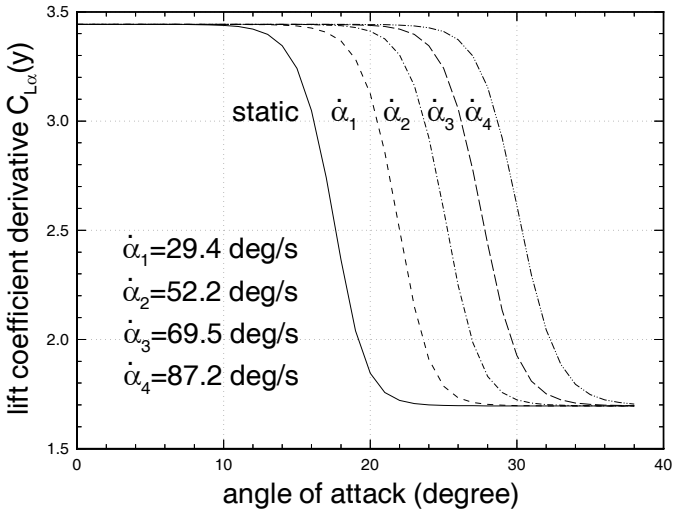

Figure 6.4: lift coefficient derivative $C_{L\alpha}$ of NACA 0015 airfoil

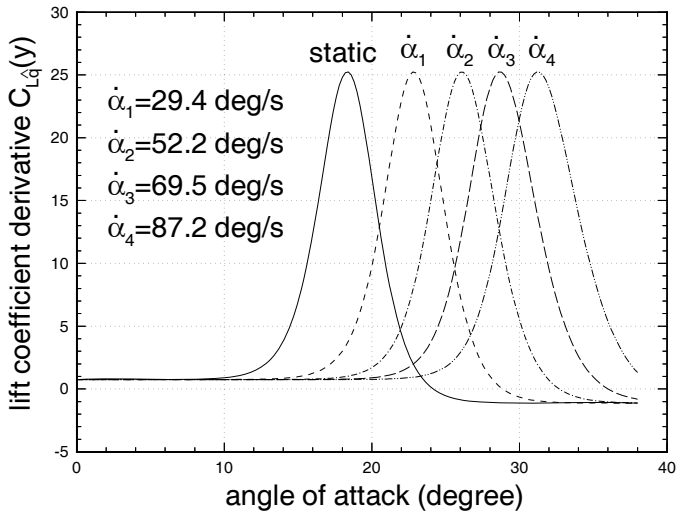

Figure 6.5: lift coefficient derivative $C_{L\hat{q}}$ of NACA 0015 airfoil

6.2 Aerodynamic Model of a 70^o Delta Wing

It is well known that vortical flow plays a dominant role in the high angle of attack characteristics of modern aircraft. Since the flow field over a 70^o delta wing is dominated by the presence of a strong leading-edge vortex system, the study of its aerodynamic characteristics can provide useful insights into those of an aircraft.

In Chapter 3, the wind tunnel data[30] and the associated aerodynamic characteristics were discussed for a 70^o flat delta wing oscillating in pitch about various mean angles of attack. Here we will describe the unsteady aerodynamics associated with these unsteady data by the proposed model.

The motion of the wing in this case can similarly be described by

$$\begin{aligned} \alpha(t) &= \alpha_0 + \alpha_A sin\omega t \\ \dot{\alpha}(t) &= \omega\alpha_A cos\omega t \\ q(t) &= \dot{\alpha}(t) \end{aligned} \tag{6.8}$$

The experimental data include the static measurements of normal force coefficient for various angles of attack and the dynamic measurements of steady-state normal force coefficient when the wing is oscillated about various mean angles of attack from 22^o to 37^o. The amplitude is fixed at $\alpha_A = 16^o$ and the frequency at $\omega = 4.36$ rad/sec. These measurements are plotted in Fig. 6.4 as circle for static case and as square for the dynamic oscillation.

Using linear terms in the determination of aerodynamic coefficients in Eq. (4.18), we obtain the following identification results:

a. Parameters in Dynamic Equation

$$\begin{aligned} &\tau_1 = 17.32\hat{t} && \tau_2 = 4.69\hat{t} \\ &\alpha_s = 42.91 \ \ deg && \sigma = 15.01 \end{aligned} \tag{6.9}$$

b. Normal Force Coefficient

$$\begin{aligned} C_N &= -0.010 + (2.422 - 2.138y + 0.659y^2)\alpha \\ &\quad +(1.195 + 0.174y + 0.360y^2)\hat{q} \end{aligned} \tag{6.10}$$

Because the pitch rate $q(t)$ is equal to the variation of angle of attack $\dot{\alpha}(t)$ in the oscillations, the τ_3 terms in Eq. (4.18) still comes out negligibly small. Therefore, it is not shown in Eq.(6.9). Using these results, we can simulate the model. The responses of the model to sinusoidal input (6.8) are plotted in Fig. 6.6 as solid lines. From the plots, we can see that the model responses accurately match the experimental data.

Different from flow over an airfoil, one can see, from Eq. (6.9), that τ_1 is approximately 4 times as big as τ_2 for the flow over the delta wing. This observation suggests that the transient properties are the dominant characteristics for vortex burst dynamics in this flowfield.

Similarly, the constant terms of normal force coefficient derivatives in Eq.(6.10) correspond to the values of conventional stability derivatives at low angles of attack. As angle of attack increases, however, the complementary state variable y is no longer zero and these aerodynamic derivatives will depend on the time histories of the motion. Figure 6.7 plots the time histories of the complementary state variable associated with the current oscillatory motions. One can see the hysteresis loops of this variable due to the dynamic lags of vortex bursting. The corresponding normal force coefficient derivatives are plotted as function of angle of attack for the current pitch oscillations in Figure 6.8 for $C_{N\alpha}(y)$ and in Figure 6.9 for $C_{N\hat{q}}(y)$. From the figures, one can view the dependencies of unsteady aerodynamic derivatives on motion time histories.

From these examples, one can see that in spite of the differences in flow mechanisms over airfoil and delta wing, the transient and time lag features of separation and vortex flows can be well described by a first-order system.

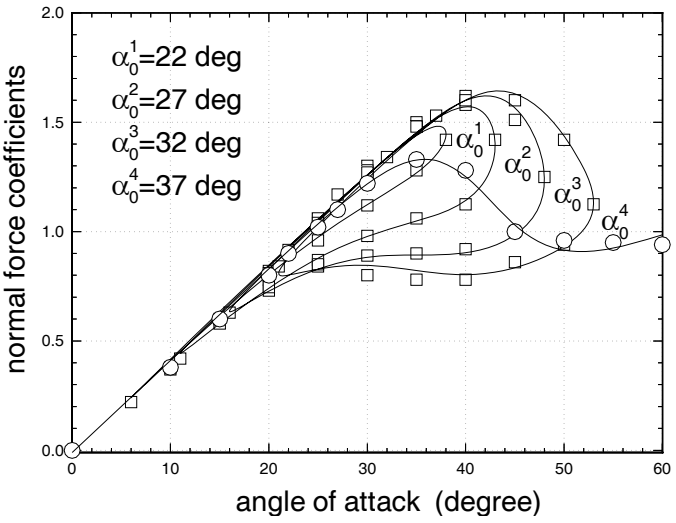

Figure 6.6: Normal force coefficients of 70^o flat delta wing

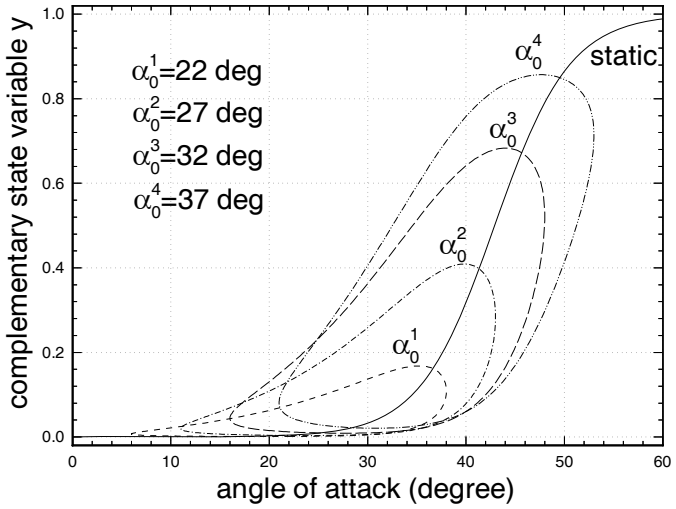

Figure 6.7: Complementary state variable y of 70^o flat delta wing

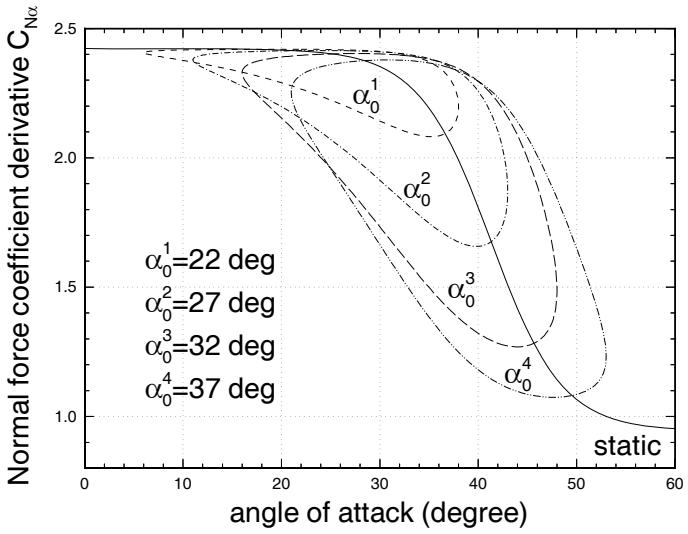

Figure 6.8: Normal force coefficient derivative $C_{N\alpha}$ of 70^o flat delta wing

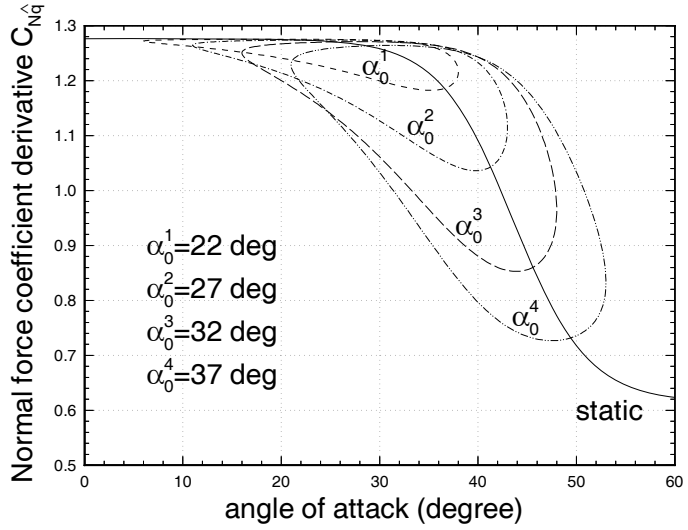

Figure 6.9: Normal force coefficient derivative $C_{N\hat{q}}$ of 70^o flat delta wing

6.3 Unsteady Aerodynamic Model for an Aircraft

Modern aircraft geometries consist of highly swept strakes, forebodies, and leading-edge wing extensions which generate concentrated vortical flow fields similar to those of 70^o delta wing. In addition to the vortical fields, these aircraft can also incorporate moderately swept wings and tail surfaces which create separation flows over the configuration. These two types of flowfields can interact with each other. In such a hybrid flowfield, both the separation and vortex burst phenomena exist. Since the dynamic properties of these two phenomena can be described individually by state-space model (4.18), it is reasonable to use this model as the simplest approximation for the full aircraft, that is, we can still use the following first-order system to describe the characteristics of an aircraft:

$$\begin{aligned} &\tau_1 \frac{dy}{dt} + y = y_0(\alpha_{eff}) \\ &\alpha_{eff} = \alpha - \tau_2 \dot{\alpha} - \tau_3 q(t)[\alpha(t) - \alpha_s] \\ &C_a = C_{a0} + C_{a\alpha}(y)\alpha + C_{a\hat{q}}(y)\hat{q} + \Delta^2 C_a \end{aligned} \tag{6.11}$$

where $a = D, L$, and m.

In order to test how well this model can do in describing the aerodynamic characteristics of a full aircraft, we are going to identify the proposed model on the basis of the unsteady wind tunnel measurements of the F-18 aircraft configurations discussed in Chapter 3.

We have two types of unsteady aerodynamic measurements. One is the harmonic oscillatory data obtained for one F-18 configuration in Chapter 2, and the other is the aerodynamic measurements in the ramp motions for another F-18 configuration. We will identify a model based on the data for each configuration. Since the tests of the ramp maneuvers cover the high angle of attack range, we first describe the associated aerodynamic characteristics using proposed model. Then we will discuss the harmonic oscillatory maneuvers.

6.3.1 Model Based on Ramp Maneuver Data

For the aircraft pitching at constant rate, the input time histories can be again written as:

$$\begin{aligned} \alpha(t) &= \dot{\alpha}t + 5, \quad 5^o \leq \alpha(t) \leq 75^o \\ q(t) &= \dot{\alpha} \end{aligned} \tag{6.12}$$

where $\dot{\alpha}$ is constant.

The static and dynamic wind tunnel data associated with the constant pitch-rate ramp motion in Ref. [30] are shown in Figures 6.10 and 6.11 for lift coefficients, in Figures 6.12 and 6.13 for drag coefficients, and in Figures 6.14 and 6.15 for pitch moment coefficients. In these figures, the static data are plotted as circle while dynamic data are plotted as square for positive pitch rates and triangle for negative pitch rates. All these data are to be used in identification of the proposed model.

Including the second derivative terms in output equation, we obtain the following identification results: *a. Parameters in Dynamic Equation*

$$\begin{aligned} &\tau_1 = 14.755\hat{t}, \qquad \tau_2 = 1.937\hat{t} \\ &\alpha_s = 36.644^o, \qquad \sigma = 7.05 \end{aligned} \tag{6.13}$$

b. Expression of Aerodynamic Coefficients

$$\begin{aligned} C_L &= -0.037 + (5.075 + 1.615y - 3.839y^2)\alpha \\ &\quad +(-4.555 + 1.222y + 1.524y^2)\alpha^2 \\ &\quad +(-4.060 + 57.037y - 1.021y^2)\hat{q} \\ &\quad +(102.3 - 2026.5y + 2388.4y^2)\hat{q}^2 \\ &\quad +(61.051 - 141.450y + 45.808y^2)\alpha\hat{q} \end{aligned} \tag{6.14}$$

$$\begin{aligned} C_D &= 0.079 + (-0.239 + 5.880y - 3.774y^2)\alpha \\ &\quad +(1.710 - 5.487y + 3.442y^2)\alpha^2 \\ &\quad +(-6.682 + 56.272y + 50.228y^2)\hat{q} \\ &\quad +(-177.619 + 460.195y + 880.022y^2)\hat{q}^2 \\ &\quad +(59.589 - 152.679y + 36.563y^2)\alpha\hat{q} \end{aligned} \tag{6.15}$$

$$\begin{aligned} C_m &= -0.046 + (0.621 + 1.531y - 1.671y^2)\alpha \\ &\quad +(-2.188 + 2.097y - 0.547y^2)\alpha^2 \\ &\quad +(-15.358 + 82.546y - 25.891y^2)\hat{q} \\ &\quad +(9.419 + 1844.82y - 1178.75y^2)\hat{q}^2 \\ &\quad +(24.383 - 155.510y + 105.108y^2)\alpha\hat{q} \end{aligned} \tag{6.16}$$

With the identification results given in Eqs. (6.13), (6.14), (6.15) and (6.16), we simulate the system (6.11) with input time histories given in Eq.(6.12). The corresponding responses are plotted as solid lines in Figures 6.10 through 6.15, respectively. From these plots, one can see that the system responses match the experimental data very well.

From the above results, one can see that τ_1 is approximately 7 times as big as τ_2. This result shows that in the unsteady flowfield around the aircraft with highly swept strakes, forebodies, and leading-edge wing extensions, transient properties associated with vortex burst dynamics are dominant effects in governing the unsteady aerodynamic characteristics of the aircraft. τ_3 still comes out negligibly small so as to be neglected.

In all the above, the identifiability of the parameters and the performance of the proposed model have been demonstrated by using the wind tunnel measurements of an airfoil, a flat delta wing and, finally, a realistic aircraft. The identification results show that within the

framework of the proposed state-space model, it is possible to analyze complex unsteady aerodynamics in high angle-of-attack regime for an aircraft.

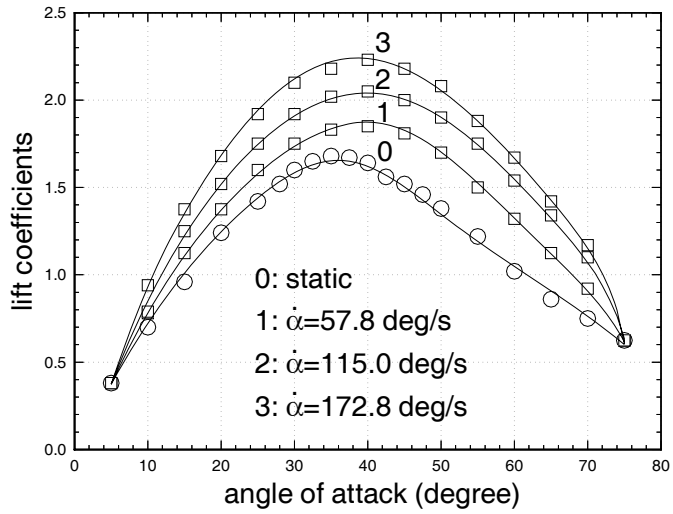

Figure 6.10: Lift coefficient of F-18 aircraft for positive pitch rates

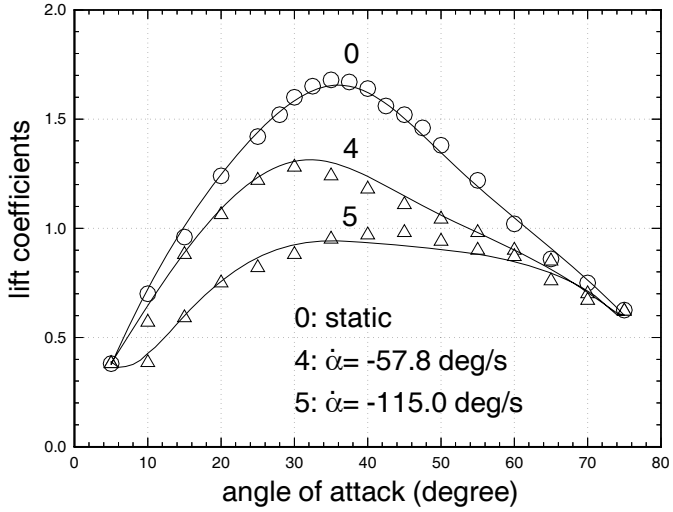

Figure 6.11: Lift coefficient of F-18 aircraft for negative pitch rates

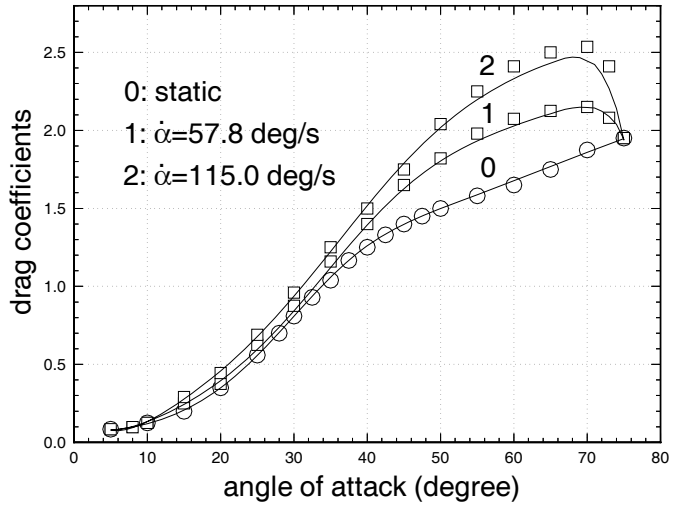

Figure 6.12: Drag coefficient of F-18 aircraft for positive pitch rates

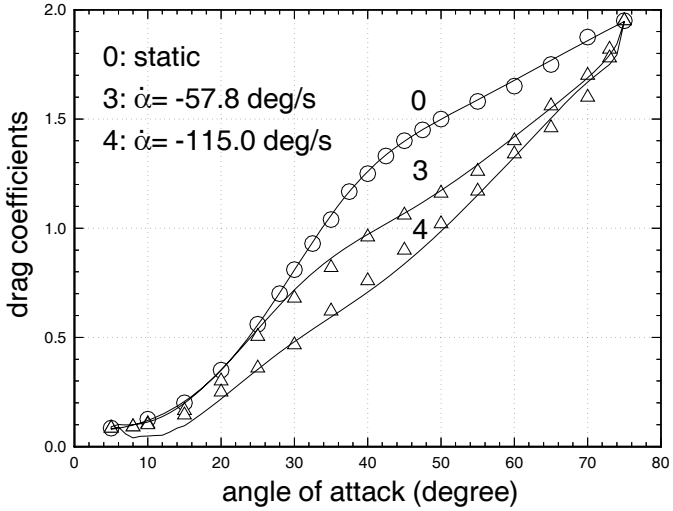

Figure 6.13: Drag coefficient of F-18 aircraft for negative pitch rates

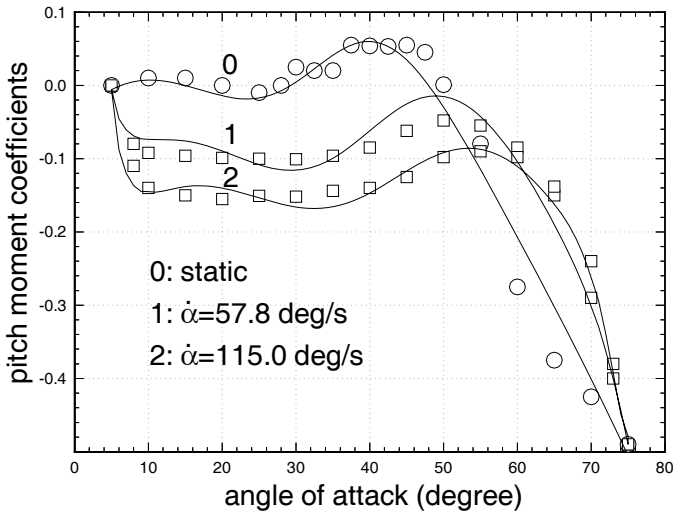

Figure 6.14: Pitch moment coefficient of F-18 aircraft for positive pitch rates

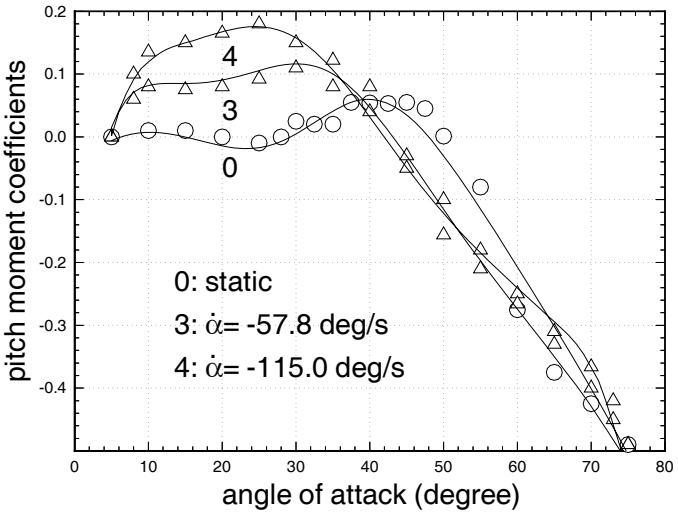

Figure 6.15: Pitch moment coefficient of F-18 aircraft for negative pitch rates

6.3.2 Model Based on Harmonic Oscillatory Maneuver Data

We obtained two types of harmonic oscillatory data in Chapters 2 and 3, one is oscillating in pitch, and the other is oscillating in plunge. For the oscillatory maneuvers in pitch, we have a large number of measurements in the angle of attack range of interest, and the obtained results are consistent to those in previous tests. Therefore, these data have relatively high fidelities. For the oscillatory maneuvers in plunge, however, we only tested a few maneuvers. As we know from Chapter 3, some observations about the measurements of these few maneuvers cannot be explained at this time, and also we are short of data to further verify the aerodynamic characteristics associated with these observations. Therefore we will focus on the pitch oscillation data in present unsteady aerodynamic modeling.

From the discussions in Chapter 3, one observed no significant hysteresis loops for the lift and drag in these harmonic oscillations. These observations may suggest that, different from the flowfields discussed above, the dynamic lags of the vortex and separated flows are small in those harmonic oscillatory tests. However, one observed significant hysteresis loops for the pitch moment in the oscillations. It was further observed that these hysteresis loops are dependent on the amplitudes, the frequencies, and the mean angles of attack for given tunnel speed in the oscillatory tests. The unsteady aerodynamic characteristics associated with these loops were attributed to the effects of the $\dot{\alpha}(t)$ and $q(t)$. As we discussed in Chapter 3, the characteristics of the tail lift responses in the oscillatory motions are responsible for these hysteresis loops since the tail lift is the major contribution to the pitch moment. The $\dot{\alpha}(t)$ can produce the dynamic delay of the tail lift responses to the change of the flight conditions while the pitch rate $q(t)$ can change the tail angle of attack instantaneously. The corresponding delay effects may be related to the time it takes the flow to move from the C.G. of the aircraft to the tail. Therefore the associated flow mechanisms are quite different from what we discussed in the previous examples.

In spite of the different flow mechanisms, we still use the same model structure in Eq.(6.11)

to model the unsteady aerodynamic characteristics associated with these oscillatory maneuvers. According to the above discussions, we will focus on the pitch moment only. Since the flowfields are pretty much at quasi-steady flow conditons, we will neglect the relaxation time constant τ_1 to simplify the analysis. In this case, τ_2 and τ_3 may become time constants associated with the delays of the tail lift responses to the change of the flight conditions, and the state variable $y(t)$ is just a shaping function for the unsteady flowfields of the aircraft. Therefore, the model (6.11) reduces to,

$$\begin{aligned} y &= y_0[\alpha - \tau_2\dot{\alpha} - \tau_3 q(\alpha - \alpha_s)] \\ C_m &= C_{m0} + C_{m\alpha}(y)\alpha + C_{m\hat{q}}(y)\hat{q} + \Delta^2 C_m \end{aligned} \tag{6.17}$$

Here we use the static data and select two extreme sets of oscillatory data discussed in Chapter 3 to identify the proposed model. One is set A_4 in Table 3.1 and the other is set C_2 in Table 3.3, containing 4 maneuvers altogether. The tunnel speed for these maneuvers is 67 ft/s, and thus the characteristics time can be computed as

$$\hat{t} = \frac{c}{2V} = \frac{0.7857}{2(67)} = 5.8634 \times 10^{-3} \tag{6.18}$$

On the basis of these data, the identification results are as following,

a. Parameters in State Equation

$$\begin{aligned} &\tau_2 = 5.3382\hat{t}, \qquad &&\tau_3 = 0.1705\hat{t} \\ &\alpha_s = 29.0383^o, \qquad &&\sigma = 8.7204 \end{aligned} \tag{6.19}$$

b. Expression of Pitch Moment Coefficient

$$\begin{aligned} C_m &= -0.0213 + (-0.2815 + 6.1048y + 1.7546y^2)\alpha \\ &\quad +(0.1153 - 16.6258y + 6.8465y^2)\alpha^2 \\ &\quad +(-5.0994 - 1.8078y + 50.1242y^2)\hat{t}q \end{aligned} \tag{6.20}$$

For the results as given in Eqs.(6.14) and (6.15), we are going to discuss some basic features of the model in the following aspects.

1. Time Constants: τ_2 and τ_3

From the time constants as given in Eq.(6.19), one can see that τ_2 is nearly 30 times as big as τ_3. Therefore, the delay effects due to the $\dot{\alpha}$ are large while the delay effects due to the pitch rate q are small. This result is exactly what we expect since the $\dot{\alpha}$ produces the delays of the tail lift responses to the angle of attack change because it takes time for the flow to travel from the C.G. to the tail while the pitch rate can change the tail angle of attack almost instantaneously.

2. Identification Accuracy

Using the results obtained, we can simulate the model using the the measured input time histories. The responses of the model are plotted as solid lines in Figure 6.16 for maneuver set A_4 and in Figure 6.17 for maneuver set C_2. The corresponding measurements of the pitch moment coefficients are plotted as dashed lines in each Figure. From these plots, one can see that the model responses match the experimental data very well.

3. An Example of Model Prediction Capability

Here we further compute the model responses to some other oscillatory maneuvers whose experimental measurements were not included in estimating the model. Figure 6.18 plots the model responses to maneuver set B_4 picked from Table 3.2 and the corresponding experimental data. From the plots, one can see the accuracy of the model in matching the experimental data. Although we can not completely evaluate the aerodynamic prediction capabilities of the model through a few simulations, this example already shows some good features of the proposed model in predicting the aerodynamic characteristics.

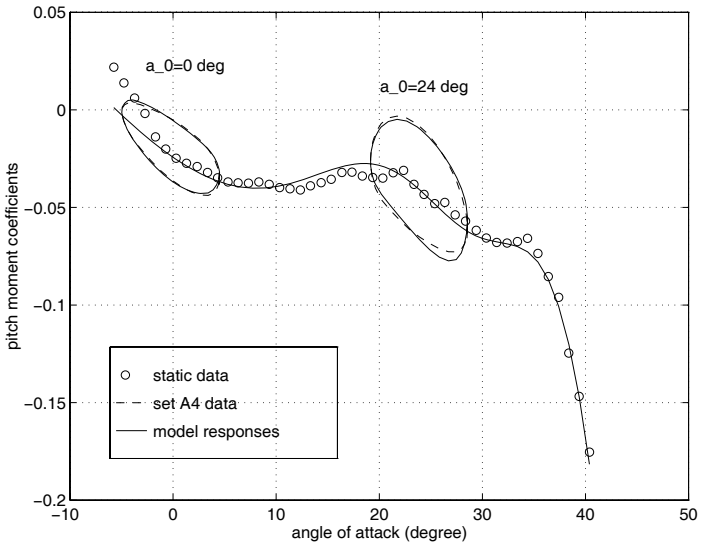

Figure 6.16: Model Responses and Measurements for Maneuver Set A_4

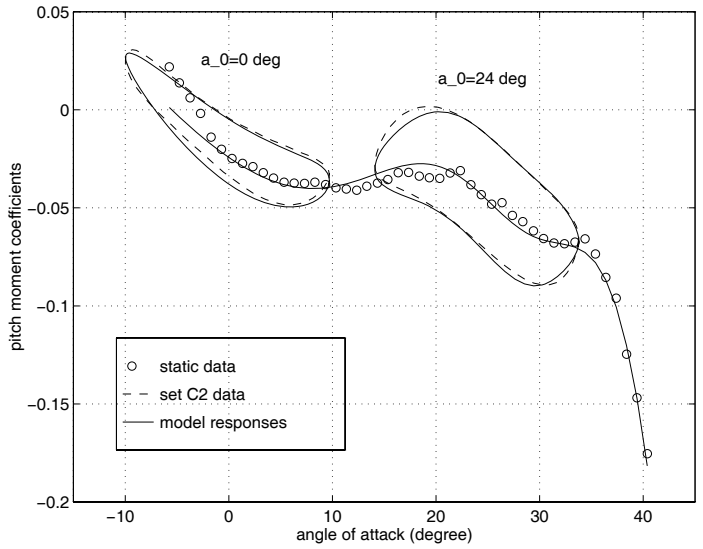

Figure 6.17: Model Responses and Measurements for Maneuver Set C_2

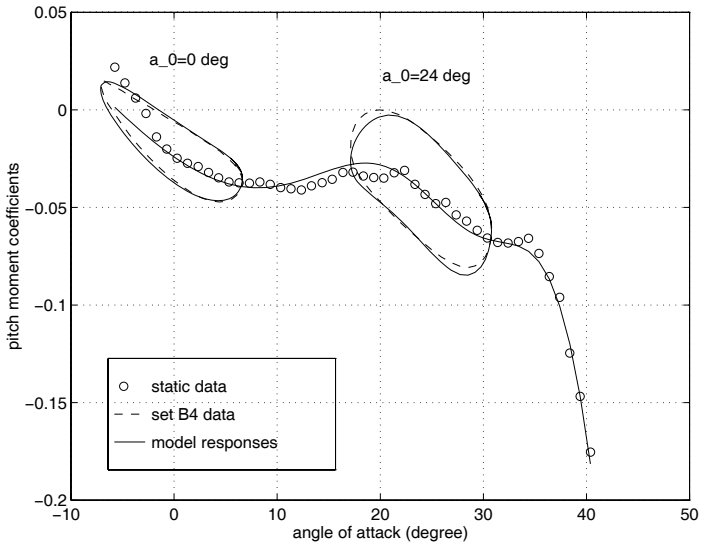

Figure 6.18: Model Responses and Measurements for Maneuver Set B_4

4. Characteristics Time Scales

In Eqs.(6.19) and (6.20), we present the aerodynamic model in a form scaled by the characteristics time $\hat{t}$. Specifically, all the model parameters related to the motions are presented in terms of the characteristics time $\hat{t}$, including time constants: τ_2 and τ_3, and the aerodynamic derivative $C_{m\hat{q}}$. The purpose is trying to model the tunnel speed effects on these quantities, resembling the nondimensional analysis performed in Chapter 3. In the identification process, we estimated the model by using the experimental data with the same characteristics time given in Eq.(6.18), and in the model performance validations as shown in Figures 6.16, 6.17 and 6.18, all the model responses are computed for the oscillatory maneuvers with the same characteristics time $\hat{t}$. Here, we are going to investigate the performance of this characteristics time modeling in predicting the aerodynamic characteristics.

We pick the maneuver set A_5 in Table 3.1 and the maneuver set C_3 in Table 3.3 for the investigations. The tunnel speed for the oscillatory maneuvers in these sets is 95 ft/s, and thus the associated characteristics time can be computed as

$$\hat{t} = \frac{0.7857}{2(95)} = 4.1353 \times 10^{-3} \tag{6.21}$$

Substituting this new characteristics time into the aerodynamic model as given in Eqs.(6.19) and (6.20), we compute the model responses to the measured input time histories for the maneuvers in sets A_5 and C_3, respectively. In Figure 6.19, these obtained responses are plotted as solid lines, and the corresponding aerodynamic measurements are plotted as dashed lines for maneuvers in set A_5 and as dashed-dotted lines for maneuvers in set C_3. From these plots, one can see that the model responses very well match the corresponding experimental data. Therefore, the introduction of the characteristics time in the aerodynamic model includes the tunnel speed effects on the aerodynamic characteristics. The ignorance of the characteristics time effects in the aerodynamic modeling can result in large errors. This result can further be seen clearly through the following computations.

We re-compute the model responses to the maneuvers in sets A_5 and C_3, respectively. However, instead of using the characteristics time given in Eq.(6.21), we use the characteristics time given in Eq.(6.18). The obtained model responses are plotted as solid lines in Figure 6.20 for maneuvers in set A_5 and in Figure 6.21 for maneuvers in set C_3. In the plots, the corresponding experimental measurements are also shown as dashed lines. As one can see, from these plots, that the errors between the model responses and the experimental measurements are large. Therefore these characteristics time effects have to be included in the aerodynamic model.

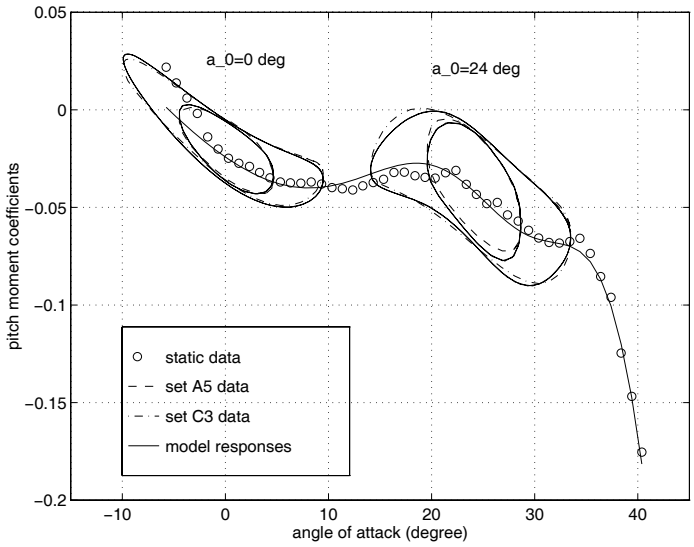

Figure 6.19: Model Responses and Measurements for Maneuver Sets A_5 and C_3

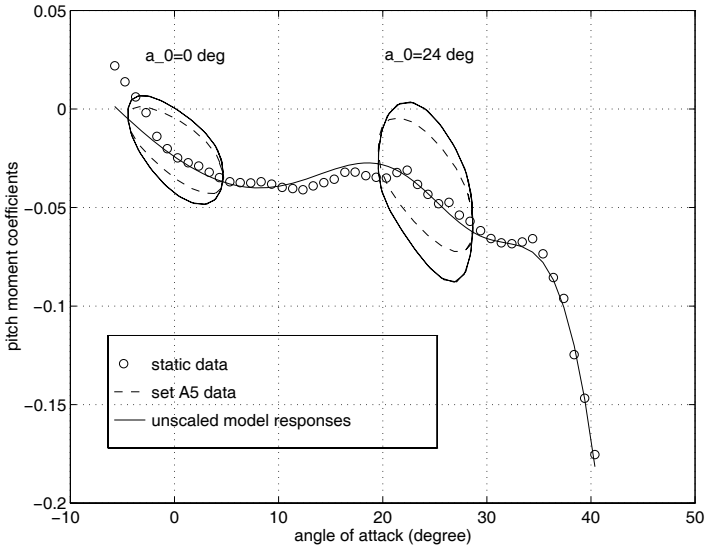

Figure 6.20: Unscaled Model Responses and Measurements for Maneuver for Maneuver Set A_5

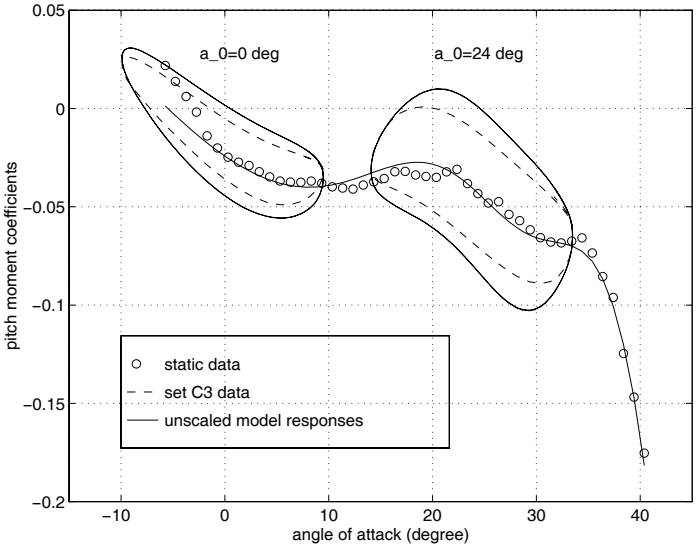

Figure 6.21: Unscaled Model Responses and Measurements for Maneuver for Maneuver Set C_3

5. Improvement of Stability Derivative Approach

From the above discussions, one can see that the proposed aerodynamic model is very compact in structure. It only involves a few parameters but has very good performance in predicting the aerodynamic characteristics in the angle of attack range of current interest. This model is certainly a significant improvement to the traditional stability derivative modeling.

In the stability derivative approach, the aerodynamic coefficient is expressed as,

$$C_m = C_{m0} + C_{m\alpha}\alpha + C_{m\hat{q}}\hat{t}q \tag{6.22}$$

and the aerodynamic derivatives are then determined using the in-phase and the out-of-phase components of the experimental measurements for the oscillatory maneuvers by,

$$\begin{aligned} C_{m\alpha} &= \frac{2}{\alpha_A T}\int_0^T C_m(t)sin(\omega t)dt \\ C_{m\hat{q}}\hat{t} &= \frac{2}{\alpha_A \omega T}\int_0^T C_m(t)cos(\omega t)dt \end{aligned} \tag{6.23}$$

where $C_m(t)$ is the measurement of the aerodynamic coefficient time histories, and T is the period of the oscillatory motion. The derivations and details of this approach are included in Appendix A.

However, the values of the aerodynamic derivatives obtained are strongly dependent on the amplitude and frequency of the aircraft oscillations. This fact makes this approach limit its applications. As an illustration, Tables 6.1 and 6.2 show some of the computational results of the out-of-phase derivatives $C_{m\hat{q}}\hat{t}$ using different oscillatory data. As one can see, from the tables, that the values of $C_{m\hat{q}}\hat{t}$ are dependent on the amplitude, the frequency and the mean angles of attack of the oscillations, and it is a nontrivial problem to obtain a description for practical use based on these computational results. However, the aerodynamic description proposed in this research model the aerodynamic derivatives as

Table 6.1: Out-of-Phase Derivatives Using the Data for Amplitude $\alpha_A = 5^o$

Frequency	**Mean AOA**	**Amplitude**	$C_{m\hat{q}}\hat{t}$
0.5 Hz	0^o	5^o	-0.0292
0.5 Hz	12^o	5^o	-0.0490
0.5 Hz	24^o	5^o	-0.0557
1.0 Hz	0^o	5^o	-0.0268
1.0 Hz	12^o	5^o	-0.0415
1.0 Hz	24^o	5^o	-0.0485
1.414 Hz	0^o	5^o	-0.0255
1.414 Hz	12^o	5^o	-0.0399
1.414 Hz	24^o	5^o	-0.0443

functions of the state variable which is driven by the input time histories. The resulting aerodynamic derivatives can be dependent on the the amplitude, the frequency, and the mean angle of attack of the oscillation. From all the previous discussions, we can see that the proposed model is doing a good job. It certainly improves the traditional stability derivative approach.

The the model is still under investigation, however. Several aspects need to be addressed, such as which parameters are dominant in the model, what is the minimum number of parameters needed for a valid description, and what kind of unsteady wind tunnel data should be used for the model identifications, and even the reform of the model structure. These questions should be addressed in the future research.

Table 6.2: Out-of-Phase Derivatives Using the Data for Amplitude $\alpha_A = 10^o$

Frequency	**Mean AOA**	**Amplitude**	$C_{m\hat{q}}\hat{t}$
0.5 Hz	0^o	10^o	-0.0309
0.5 Hz	12^o	10^o	-0.0466
0.5 Hz	24^o	10^o	-0.0566
1.0 Hz	0^o	10^o	-0.0284
1.0 Hz	12^o	10^o	-0.0404
1.0 Hz	24^o	10^o	-0.0504

6.4 Summary

A state-space model is presented in this chapter to describe the unsteady aerodynamic characteristics in high angle-of-attack regime. First-order differential equations are used to govern the dynamics of separation and vortex flows. Taylor series expansion in terms of input variables are used in determination of aerodynamic characteristics, resembling the current approach of stability derivatives. The performance of the model has been validated by wind tunnel data of an airfoil, a delta wing and a realistic aircraft. The results show that within the framework of the proposed model, it is possible to obtain good agreement with different unsteady wind tunnel data in high angle-of-attack regime.

The models developed in current research are still under investigation, but the results obtained have demonstrated the potential of this method to model more complex unsteady aerodynamic characteristics of a full aircraft at high angles of attack.

Chapter 7

Conclusions and Suggestions for Future Work

7.1 DyPPiR Experiments and Data Reductions

Low-speed wind-tunnel experiments were conducted for a fighter aircraft configuration through the harmonic oscillatory motions in the Virginia Tech Stability Wind Tunnel. The model was sting-mounted on the DyPPiR through a six-component strain-gage balance. Because the elastic deformation of the sting, however, the elastic modes of the sting enter the system when the model is oscillating sinusoidally. To obtain the aerodynamic responses to the pre-programmed input time histories, we use a multirate digital signal processing approach to design a digital system for data reduction. First, we identify the frequencies of the elastic modes of the sting by using Discrete Fourier Transform. Then we design the sampling rate conversion system in digital domain to reduce the bandwidth of the sampled data. In this resampling process, the effects of the noise and the sting modes with high frequencies are removed from the data. Finally, we design Finite Impulse Response filters with linear phase characteristics to reject the effects of the dominant mode of the sting. After these operations in digital domain, we reject all the effects of the elastic modes of the

sting, and end up with the aerodynamic characteristics responses to the measured input time histories. Following conclusions can be made for this digital system,

1. Digital signal processing is an effective approach for unsteady wind-tunnel data reductions when the maneuvers of interest are periodic motions whose frequencies lie far away from the sting frequencies.

2. Sampling rate conversion system in digital domain is essential and important in the data processing. It can be used to reduce the bandwidth of interest and achieve the low rate without introducing distortion to the data, resulting in efficient filter designs.

3. Linear phase FIR filters are designed using Remez exchange algorithms in the data reductions. Linear phase characteristics guarantee no phase distortion on the data while the magnitude distortions are within the specified tolerances.

The following recommendations about the DyPPiR tests and the associated data reduction for the future are,

1. A stiff sting structure is highly desirable.

2. Implementations of the sampling rate conversion system in the programmable digital signal processing (DSP) chips are suggested and these DSP chips can be included in the DyPPiR data acquisition systems.

3. Linear phase FIR filters can also be implemented in the DSP chips. In such a case, we can implement the digital data reduction system in hardware, and read the aerodynamic characteristics directly from the output of the DyPPiR data acquisition systems.

7.2 Structures of Aerodynamic Model

A state-space model has been developed to describe the unsteady aerodynamic characteristics up to the high angles of attack regime. A complementary flow separation variable is introduced as the state of flow separation or vortex burst. A first-order differential equation is used to govern the dynamics of flow separation or vortex bursting through this state variable. Taylor series expansion in terms of the input variables are used in the determination of aerodynamic characteristics, resembling the current approach of the stability derivatives. However, these derivatives are no longer constant. They are dependent on the state variable of flow separation or vortex burst. In this way, the changes in stability derivatives with the angle of attack have been included dynamically. The performances of the model have been validated by the wind-tunnel measurements of a NACA 0015 airfoil, a 70^o delta wing and two F-18 aircraft configurations. These results show that within the framework of the proposed model, it is possible to obtain good agreement with different unsteady wind tunnel data in high angle-of-attack regime. Based on these primary results on the model, we have the following conclusions about the framework of the proposed model.

1. The introduced state equation very well characterizes the separation flows of an airfoil, the vortex flows of a delta wing, or even the hybrid flows of separation and vortex flows around a realistic aircraft.

2. For the dynamics of the flowfields that are governed by a first-order differential equation, the pure time delays are the dominant characteristics for separation flows while the transient properties are the dominant effects for vortex flows.

3. The expressions for aerodynamic coefficients using Taylor series expansions in terms of the input variables are consistent with the current stability derivative approach. These derivatives have further been modeled as quadratic polynominals of the state variable. The associated errors have been proven to be bounded. The identification results show that

these derivatives are dependent on the amplitudes and frequencies of aircraft oscillations.

4. Within the dynamic range the experimental data covers, the proposed model is identifiable in the sense that a unique optimal estimate of the model exist. But the obtained model is not guaranteed to work outside the dynamic range mentioned.

The basic purpose in the current unsteady aerodynamic modeling up to the high angle of attack region is to present a model with much flexibility in the analysis of the high angle of attack unsteady aerodynamic characteristics. The results show that the proposed model is very effective and comprehensive in the prediction of unsteady aerodynamics. They also encourage the extension of the dynamic model to more detailed analysis of not only the high angle of attack regime but of all flight situations which may be anticipated for an aircraft during its preliminary design. The following suggestions are recommended for further development of the model:

1. We have modeled the pitch rate effects on the state of the vortex and separation flows associated with a time constant τ_3. But in the current wind-tunnel tests, the pitch rate is the same as the variations of the angle of attack. Therefore, the effects of the pitch rate are not separable from those of the variations of the angle of attack. In the future, we need the experimental data with the pitch rate different from the variation of angle of attack to investigate the pitch rate effects on the state of the flowfields.

2. Currently, we are still short of the experimental data and also short of understanding the flow physics of the unsteady aerodynamics. Also the model structure is still under investigation. Thus, it does not seem to be sufficient to study the dominant parameters in the model at the present time. As the model structure is further refined and the better understanding of flow mechanisms is achieved, the dominance of the parameters in the model should be investigated systematically.

3. As we discussed, the dynamic properties of flow separation and vortex burst are different in nature. Flow separation is dominated mainly by time delay while vortex burst is characterized mainly by transient properties. In a flowfield around an aircraft, where both phenomena exist, lumping two different dynamic properties into one state variable may not a good description. Some properties, such as interaction effects, may be lost. In such a case, the state-space model with only one state variable may not be sufficient to describe the dynamic properties of such complex flows. We recommend to define two state variables for these hybrid flowfields, with one representing the nominal position of vortex burst, and the other the nominal position of flow separation. Further development of the model is expected.

4. As the research results mentioned above accumulate, the identifiability and uniqueness of the model need to be studied systematically.

Bibliography

[1] Etkin, B., "Dynamics of Atmospheric Flight", John Wiley and Sons, Inc. New York, 1972.

[2] Etkin, B., "Dynamics of Flight- Stability and Control ", John Wiley and Sons, Inc. New York, 1982.

[3] Chambers, J. R. and Grafton, S. B., "Investigation of Lateral Directional Dynamic Stability of a Tilt-Wing V/Stol Transport", NASA TN D-5637, 1970

[4] Levinsky, E. S., "Theory of the Wing Span Loading Instabilities Near Stall", AGARD-CP-204, Prediction of Aerodynamic Loading, 1976.

[5] Hreha, M. A., "A Dynamic Model for Aircraft Poststall Departure", Ph.D. Dissertation in Aerospace and Ocean Engineering, Virginia Polytechnic Institute and State University, Blacksburg, Virginia, May 1982.

[6] Ericsson, L. E. and Reding, J. P., "Dynamic Stall at High Frequency and Large Amplitude", *Journal of Aircraft*, Vol. 17, No. 3, 1980, pp. 136-142.

[7] Tobak, M., "On the Use of the Indicial Function Concept in the Analysis of Unsteady Motions of Wings and Wing-Tail Combinations", NACA Report 1188, 1954.

[8] Tobak, M. and Schiff, L. B., "On the Formulation of the Aerodynamic Characteristics in Aircraft Dynamics", NACA TR R-456, 1976.

[9] Goman, M.G., "Mathematical Description of Aerodynamic Forces and Moments at Nonstationary Flow Regimes with a Nonunique Structure", *Proceedings of the TSAGI* (in Russian), Issue 2195, Moscow, 1983, pp.1-35.

[10] Peters, D.A., "Toward a Unified Lift Model for Use in Roter Blade Stability", *Journal of American Helicopters Society*, Vol. 30, No. 3, 1985, pp.32-42.

[11] Goman, M.G., Khrabrov, A.N., Stolyarov, G.I., Tyrtyshnikov, S.L., and Usoltzev, S.P., "Mathematical Description of Longitudinal Aerodynamic Characteristics of an Aircraft at High angles of attack with Accounting for Dynamic Effects of Separated Flow", *Preprint of TSAGI* (in Russian), Moscow, No. 9, 1990.

[12] Leishman, J.G., and Nguyen, K.Q.,"State-Space Representation of Unsteady Airfoil Behavior", *AIAA Journal*, Vol.28, No.5, 1990, pp.836-844.

[13] Goman, M. and Khrabrov, A., "State-Space Representation of Aerodynamic Characteristics of an Aircraft at High Angles of Attack", *Journal of Aircraft,* Vol. 31, No. 5, Sept.-Oct., 1994, pp.1109-1115.

[14] Fischenberg, D., "Identification of an Unsteady Aerodynamic Stall Model From Flight Test Data", AIAA Paper 95-3438, Aug. 1995.

[15] Ericsson, L. E. and Reding, J. P., "Unsteady Airfoil Stall, Review and Extension", *Journal of Aircraft*, Vol. 8, August 1971, pp.609-616.

[16] Wagner, H.,"Uber die Enstehung des dynamishen Auftriebs von Tragflugeln", Z.angew. Math. U.Mech. 5, 1925, pp.17-35.

[17] Garick, I.E., "Nonsteady Wing Characteristics", Aerodynamic Components of Aircraft at High Speeds. Editors: Donovan, A.F. and Lawrence, H.R., Princeton University Press, 1957, pp.658-793.

[18] Jumper, E.J., Schreck, S.J. and Dimmick, R.L., "Lift-Curve Characteristics for an Airfoil Pitching at Constant Rate", *Journal of Aircraft*, Vol. 24, No. 10, Oct. 1987, pp.680-687.

[19] Daley, D. C. and Jumper, E.J., "Experimental Investigation of Dynamic Stall for a Pitching Airfoil", *Journal of Aircraft,* Vol. 21, No. 10, Oct. 1984, pp.831-832.

[20] Niven, A. J. and Galbraith, R. A. McD., "Experimental on the Establishment of Full Attached Airfoil Flow from the Full Stalled Condition During Ramp-Down Motions", International Council of the Aeronautical Sciences, Paper 90-3.4.3, September 1990.

[21] Ericsson, L. E., "Dynamic Airfoil Flow Separation and Reattachment", *Journal of Aircraft*, Vol. 32, No. 6, November-December 1995, pp.1191-1197.

[22] Ericsson, L. E., "Flow Reattachment on Wings in Pitch-Down Motion", International Council of the Aeronautical Sciences Paper 94-3.4.4, September 1994.

[23] Ericsson, L. E., "Pitch-Down Dynamic Stall Characteristics", AIAA Paper 94-0535, January 1994.

[24] Wedemeyer, E., "Vortex Breakdown",*High Angle of Attack Aerodynamics,* AGARD Lecture Series 121, 1982, pp.9-1-9-7.

[25] Atta, R. and Rockwell, D., "Leading-Edge Vortices Due to Low Reynolds Number Flow Past a Pitching Delta Wing",*AIAA Journal*, Vol. 28, No. 6, June 1990, pp.995-1004.

[26] Atta, R. and Rockwell, D., "Hysteresis of Vortex Development and Breakdown on an Oscillating Delta Wing",*AIAA Journal,* Vol. 25, No. 11, November 1987, pp.1512-1513.

[27] McCroskey, W.J., "Unsteady Airfoils", *Annual Review of Fluid Mechanics*, Vol. 14, 1982, pp.285-312.

[28] Gad-el-Hak, M. and Ho, C.M., "The Pitching Delta Wing", *AIAA Journal*, Vol. 23, Nov. 1985, pp. 1660-1665.

[29] Ericsson, L. E., "Pitch Rate Effects on Delta Wing Vortex Breakdown", *Journal of Aircraft,* Vol. 33, No. 3, May-June 1996, pp.639-642.

[30] Brandon, J. M., "Dynamic Stall Effects and Application to High Performance Aircraft", AGARD Report No. 776, Apr. 1991, pp.2.1-2.15.

[31] Liiva, J., Davenport, F. J., Gray, L., and Walton, I. C., "Two-Dimensional Tests of Airfoils Oscillating Near Stall", TR 68-13, U. S. Army Aviation Labs., Fort Eustis, VA, April 1968.

[32] Windsor, R. I., "Measurements of Aerodynamic Forces on an Oscillating Airfoil", TR-69-98, U. S. Army Aviation Labs., Eustis, VA, March 1970.

[33] Carr, L. W., McAlister, K. W., and McCroskey, W. J., "Analysis of the Development of Dynamic Stall Based on Oscillating Airfoil Experiments", NASA TN D-8382, January 1977.

[34] Ericsson, L. E. and Reding, J. P., "Dynamic Stall at High Frequency and Large Amplitude", *Journal of Aircraft,* Vol. 17, No. 3, 1980, pp. 136-142.

[35] Fan, Y. and Lutze, F. H.,"Identification of an Unsteady Aerodynamic Model at High

Angles of Attack", AIAA Paper 96-3407.

[36] Crochiere, R.E. and Rabiner, L.R., *Multirate Digital Signal Processing,* Prentice Hall, Englewood Cliffs, NJ, 1983.

[37] Oppenheim, A.V. and Schafer, R.W., *Discrete Time Signal Processing*, Prentice Hall, Englewood Cliffs, NJ, 1989.

[38] Hamming, R.A., *Digital Filters,* Prentice Hall, Englewood Cliffs, NJ, 1991.

[39] Fan, Y.G., Lutze, F.H. and Cliff, E.M.,"Time-Optimal Lateral Maneuvers of An Aircraft", *AIAA Journal of Guidance, Control and Dynamics,* Vol. 18, No. 5, Sept.-Oct. 1995, pp.1105-1112

Appendix A

In-Phase and Out-of-Phase Derivatives

A.1 Stability Derivatives

As we discussed at the beginning, traditional stability derivative approach in formulation of aerodynamic forces and moments acting on an aircraft in arbitrary motion is using the linear terms in their Taylor series expansions. Let C_a be an aerodynamic coefficient where $a = L$, D, or m, then it can be expressed as,

$$C_a(\alpha, \hat{q}) = C_{a0} + C_{a\alpha}\alpha + C_{a\hat{q}}\hat{q} \tag{A.1}$$

where $C_{a\alpha}$ and $C_{a\hat{q}}$ are defined as

$$C_{a\alpha} = (\frac{\partial C_a}{\partial \alpha})_{ref}, \quad C_{a\hat{q}} = (\frac{\partial C_a}{\partial \hat{q}})_{ref} \tag{A.2}$$

and the subscript ref indicates that the derivatives are evaluated at some reference point, and $\hat{q} = q\hat{t}$, where $\hat{t}$ is defined in Eq.(3.7) in Chapter 3.

These derivatives are known as aerodynamic stability derivatives since the static stability at the equilibrium can be determined by their signs and magnitudes. Based on this idea, a

major fraction of the total effort in aerodynamic research in the past has been devoted to the determination, by theoretical and experimental means, of the aerodynamic derivatives needed for application to flight mechanics problems. This method for modeling aerodynamic characteristics has been found to work extremely well for attached flows at low angles of attack. Furthermore the addition of quadratic terms in the expansions, expressing the changes in stability derivatives, can extend the useful range of flight conditions of practical applications. Including the quadratic terms in the expansions, we can express C_a as,

$$C_a(\alpha, \hat{q}) = C_{a0} + C_{a\alpha}\alpha + C_{a\hat{q}}\hat{q} + \frac{1}{2}(C_{a\alpha^2}\alpha^2 + 2C_{a\alpha\hat{q}}\alpha\hat{q} + C_{a\hat{q}^2}\hat{q}^2) \tag{A.3}$$

where $C_{a\alpha}$ and $C_{a\hat{q}}$ are still defined in Eq.(A.2) and the other derivatives are defined as following,

$$C_{a\alpha^2} = (\frac{\partial^2 C_a}{\partial \alpha^2})_{ref}, \quad C_{a\alpha\hat{q}} = (\frac{\partial^2 C_a}{\partial \alpha \partial \hat{q}})_{ref}, \quad C_{a\hat{q}^2} = (\frac{\partial^2 C_a}{\partial \hat{q}^2})_{ref} \tag{A.4}$$

Differentiating representation (A.3) with respect to α and $\hat{q}$, respectively, we obtain the following

$$\begin{aligned} \frac{\partial C_a}{\partial \alpha} &= C_{a\alpha} + C_{a\alpha^2}\alpha + C_{a\alpha\hat{q}}\hat{q} \\ \frac{\partial C_a}{\partial \hat{q}} &= C_{a\hat{q}} + C_{a\alpha\hat{q}}\alpha + C_{a\hat{q}^2}\hat{q} \end{aligned} \tag{A.5}$$

From Eq.(A.5), one can see that unlike the case of using the linear representation (A.1), the derivatives of C_a with respect to α and $\hat{q}$ are no longer constant. They become dependent on the angle of attack α and pitch rate $\hat{q}$.

In above formulations, using either linear or quadratic aerodynamics, it is assumed that all the coefficients in the expansions are constants. On the basis of this assumption, the experimental data in harmonic oscillatory tests can be used to compute these derivatives, resulting the in-phase and the out-of-phase derivatives.

A.2 Determination of Stability Derivatives

This approach in determining certain stability derivatives, or contributions of stability derivatives uses the measurements of in-phase and out-of-phase components of aerodynamic forces and moments corresponding to the harmonic sinusoidal pitch, yaw, or roll motions. Here our purpose is to illustrate the basic principle of this approach. Therefore we will discuss only the pitch motion. For the oscillatory motion in pitch with mean angle of attack α_0, amplitude α_A and frequency ω, the time histories of angle of attack and pitch rate are given in Eq.(2.1).

A.2.1 Linear Aerodynamics Solution

If the linear representation (A.1) is used, the lift coefficient time history corresponding to the harmonic oscillatory motion in Eq.(2.1) is,

$$C_a(t) = C_{a0} + C_{a\alpha}\alpha_0 + C_{a\alpha}\alpha_A sin(\omega t) + C_{a\hat{q}}\hat{q}_{max} cos(\omega t) \tag{A.6}$$

Here $C_a(t)$ is the output signal of an aerodynamic coefficient which can be obtained from wind-tunnel measurements for the harmonic oscillatory motion in Eq.(2.1). In such a case, the in-phase and out-of-phase output signals can be generated by multiplying $C_a(t)$ by $sin(\omega t)$ and $cos(\omega t)$, respectively.

$$\begin{aligned} S_{in}(t) &= C_a(t) sin(\omega t) \\ S_{out}(t) &= C_a(t) cos(\omega t) \end{aligned} \tag{A.7}$$

Using Eq. (A.6), the in-phase and out-of-phase output signals can be expressed in terms of aerodynamic derivatives as,

$$\begin{aligned} S_{in}(t) &= (C_{a0} + C_{a\alpha}\alpha_0)sin(\omega t) + C_{a\alpha}\alpha_A sin^2(\omega t) + C_{a\hat{q}}\hat{q}_{max}cos(\omega t)sin(\omega t) \\ S_{out}(t) &= (C_{a0} + C_{a\alpha}\alpha_0)cos(\omega t) + C_{a\alpha}\alpha_A sin(\omega t)cos(\omega t) + C_{a\hat{q}}\hat{q}_{max}cos^2(\omega t) \end{aligned} \quad (A.8)$$

From Eq. (A.8), one can see that the in-phase and out-of-phase output signals are periodic. In order to extract the information about the aerodynamic characteristics from these signals, we look at the average values of these signals over one period.

Define the in-phase and out-of-phase aerodynamic components as the average values of the corresponding in-phase and out-of-phase signals, that is,

$$\begin{aligned} \bar{S}_{in} &= \frac{1}{T}\int_0^T S_{in}(t)dt \\ \bar{S}_{out} &= \frac{1}{T}\int_0^T S_{out}(t)dt \end{aligned} \quad (A.9)$$

where $T = 2\pi/\omega$ is the time of a period.

From this definition and by using Eq. (A.8), the in-phase and out-of-phase aerodynamic components can be evaluated through the following integrations,

$$\begin{aligned} \bar{S}_{in} &= \frac{1}{T}\{\int_0^T (C_{a0} + C_{a\alpha}\alpha_0)sin(\omega t)dt + \int_0^T C_{a\alpha}\alpha_A sin^2(\omega t)dt + \\ &\quad \int_0^T C_{a\hat{q}}\hat{q}_{max}cos(\omega t)sin(\omega t)dt\} \\ \bar{S}_{out} &= \frac{1}{T}\{\int_0^T (C_{a0} + C_{a\alpha}\alpha_0)cos(\omega t)dt + \int_0^T C_{a\alpha}\alpha_A sin(\omega t)cos(\omega t)dt + \\ &\quad \int_0^T C_{a\hat{q}}\hat{q}_{max}cos^2(\omega t)dt\} \end{aligned} \quad (A.10)$$

Since $C_{a\alpha}$ and $C_{a\hat{q}}$ are assumed constant, the integrals on the right hand sides of Eq.(A.10) can be evaluated as the following,

$$\begin{aligned}
&\int_0^T sin(\omega t)dt = 0, \qquad \int_0^T cos(\omega t)dt = 0 \\
&\int_0^T sin(\omega t)cos(\omega t)dt = 0 \\
&\int_0^T sin^2(\omega t)dt = \int_0^T cos^2(\omega t)dt = \frac{T}{2}
\end{aligned} \tag{A.11}$$

Substituting these results into Eq.(A.10), we can express the aerodynamic derivatives $C_{a\alpha}$ and $C_{a\hat{q}}$ in terms of the in-phase and out-of-phase aerodynamic components, respectively, as

$$\begin{aligned}
C_{a\alpha} &= \frac{2}{\alpha_A}\bar{S}_{in} = \frac{2}{\alpha_A T}\int_0^T C_a(t)sin(\omega t)dt \\
C_{a\hat{q}} &= \frac{2}{\hat{q}_{max}}\bar{S}_{out} = \frac{2}{\hat{q}_{max}T}\int_0^T C_a(t)cos(\omega t)dt
\end{aligned} \tag{A.12}$$

This expression provides a basis for determining the aerodynamic derivatives by experimental means. If we oscillate the aircraft according to the motion time histories given in Eq.(2.1) and compute the in-phase and out-of-phase aerodynamic components through the measurements of the corresponding in-phase and out-of-phase aerodynamic signals, then the aerodynamic derivatives can be obtained directly by Eq. (A.12). This result is obtained under the assumptions of linear aerodynamics (A.1) and constant derivative coefficients.

A.2.2 Nonlinear Aerodynamics Solution

If nonlinear representation (A.3) is used, the aerodynamic coefficient time history can then be obtained by substituting Eq.(2.1) into Eq.(A.3) as follows,

$$\begin{aligned}
C_a(t) &= C_{a0} + C_{a\alpha}\alpha_0 + \frac{1}{2}C_{a\alpha^2}{\alpha_0}^2 + \\
&\quad (C_{a\alpha} + C_{a\alpha^2}\alpha_0)\alpha_A sin(\omega t) + (C_{a\hat{q}} + C_{a\alpha\hat{q}}\alpha_0)\hat{q}_{max}cos(\omega t) + \\
&\quad \frac{1}{2}[C_{a\alpha^2}{\alpha_A}^2 sin^2(\omega t) + 2C_{a\alpha\hat{q}}\alpha_A\hat{q}_{max}sin(\omega t)cos(\omega t) + C_{a\hat{q}^2}\hat{q}_{max}^2 cos^2(\omega t)]
\end{aligned} \tag{A.13}$$

The in-phase and out-of-phase aerodynamic components can still be defined as,

$$\begin{aligned} \bar{S}_{in} &= \frac{1}{T}\int_0^T C_a(t)sin(\omega t)dt \\ \bar{S}_{out} &= \frac{1}{T}\int_0^T C_a(t)cos(\omega t)dt \end{aligned} \tag{A.14}$$

Through Eq.(A.13), noting Eq.(A.11) and the following integrals,

$$\begin{aligned} &\int_0^T sin^3(\omega t)dt = \int_0^T cos^3(\omega t)dt = 0 \\ &\int_0^T sin^2(\omega t)cos(\omega t)dt = \int_0^T sin(\omega t)cos^2(\omega t)dt = 0 \end{aligned} \tag{A.15}$$

we then obtain,

$$\begin{aligned} C_{a\alpha} + C_{a\alpha^2}\alpha_0 &= \frac{2}{\alpha_A}\bar{S}_{in} \\ &= \frac{2}{\alpha_A T}\int_0^T C_a(t)sin(\omega t)dt \\ C_{a\hat{q}} + C_{a\alpha\hat{q}}\alpha_0 &= \frac{2}{\hat{q}_{max}}\bar{S}_{out} \\ &= \frac{2}{\hat{q}_{max}T}\int_0^T C_a(t)cos(\omega t)dt \end{aligned} \tag{A.16}$$

Comparing Eq.(A.16) with Eq.(A.12), one can see that when the nonlinear aerodynamic representations are used, the in-phase and out-of-phase aerodynamic components as defined in Eq.(A.14), scaled by half the amplitudes will not be equal to $C_{a\alpha}$ or $C_{a\hat{q}}$ directly if the mean angle of attack α_0 is nonzero. High order derivative terms will be included. Actually, when the nonlinear aerodynamic representations are used, the derivatives of aerodynamic coefficient with respect to α and $\hat{q}$ are no longer constant. They are dependent on the angle of attack and pitch rate time histories as indicated in Eq.(A.5).

Substituting the angle of attack and pitch rate time histories given in Eq.(2.1) into Eq.(A.5), we obtain the corresponding dynamic oscillatory derivative time histories as follows,

$$\begin{aligned}\frac{\partial C_a}{\partial \alpha} &= C_{a\alpha} + C_{a\alpha^2}\alpha_0 + C_{a\alpha^2}\alpha_A sin(\omega t) + C_{a\alpha\hat{q}}\hat{q}_{max} cos(\omega t) \\ \frac{\partial C_a}{\partial \hat{q}} &= C_{a\hat{q}} + C_{a\alpha\hat{q}}\alpha_0 + C_{a\alpha\hat{q}}\alpha_A sin(\omega t) + C_{a\hat{q}^2}\hat{q}_{max} cos(\omega t) \end{aligned} \tag{A.17}$$

These dynamic derivatives are also periodic. Their average values in a period are given as,

$$\begin{aligned}(\frac{\partial C_a}{\partial \alpha})_{ave} &= \frac{1}{T}\int_0^T \frac{\partial C_a}{\partial \alpha} dt = C_{a\alpha} + C_{a\alpha^2}\alpha_0 \\ (\frac{\partial C_a}{\partial \hat{q}})_{ave} &= \frac{1}{T}\int_0^T \frac{\partial C_a}{\partial \hat{q}} dt = C_{a\hat{q}} + C_{a\alpha\hat{q}}\alpha_0 \end{aligned} \tag{A.18}$$

As one can see from Eqs.(A.16) and (A.18), the in-phase and out-of-phase aerodynamic components scaled by half the amplitudes are actually equal to the average values of the dynamic oscillatory derivatives.

Using the in-phase and out-of-phase aerodynamic components discussed above, we can determine the following stability derivatives,

$$C_{a\alpha}, \quad C_{a\hat{q}}, \quad C_{a\alpha^2}, \quad C_{a\alpha\hat{q}} \tag{A.19}$$

through the following procedures if the aerodynamic derivative coefficients are strictly constants.

(1) For the oscillatory motion about zero mean angle of attack: $\alpha_0 = 0$, we compute the in-phase and out-of-phase aerodynamic components as defined in Eq.(A.14) from the measurements. Then scaling these two components by half the amplitudes, we obtain $C_{a\alpha}$ and $C_{a\hat{q}}$, respectively.

(2) For the oscillatory motion about nonzero mean angle of attack: $\alpha_0 \neq 0$, we compute the in-phase and out-of-phase aerodynamic components from the corresponding measurements.

Then we can solve Eq.(A.16) for $C_{a\alpha^2}$ and $C_{a\alpha\hat{q}}$ as,

$$\begin{aligned} C_{a\alpha^2} &= \frac{1}{\alpha_0}[\frac{2}{\alpha_A}\bar{S}_{in} - C_{a\alpha}] \\ C_{a\alpha\hat{q}} &= \frac{1}{\alpha_0}[\frac{2}{\hat{q}_{max}}\bar{S}_{out} - C_{a\hat{q}}] \end{aligned} \tag{A.20}$$

Note that the results obtained here are independent of the amplitude and the frequency of the oscillations. However, it has been observed[13] that the results obtained from the tests are dependent on the amplitude and the frequency of the oscillations. This observation implies that the aerodynamic derivative coefficients in Eqs.(A.1) and (A.3) are not constants.

A.3 Analysis of In-phase and Out-of-phase Derivatives

In above discussions, a major assumption is the aerodynamic derivative coefficients are constants. This assumption implies a static aerodynamic system, i.e., the past time histories of flight conditions have no effects on the current aerodynamic forces and moments. This assumption, however, is not valid in general. The past time histories of motion have significant effects on the current aerodynamic forces and moments, especially at high angles of attack, where the separated and vortex flows are developed. In the state space model of unsteady aerodynamics developed in Chapter 4, the Taylor series expansions are still used to formulate the unsteady aerodynamics, but all the aerodynamic derivatives are no longer constant. They depend on the motion time histories through the complementary state variable. In such a case, the in-phase and out-of-phase aerodynamic components as defined above can still be measured and computed but they may not provide as much information of aerodynamic characteristics as we discussed above. Let's illustrate this result through the following example.

It is assumed here that the aerodynamic coefficient is approximated by the linear terms in its Taylor series expansions, but instead of being constant, the aerodynamic derivatives are now functions of the complementary state variable $y(t)$, that is,

$$C_a = C_{a0} + C_{a\alpha}(y)\alpha + C_{a\hat{q}}(y)\hat{q} \tag{A.21}$$

where $y(t)$ is governed by a first order differential equation driven by the motion time histories.

In this case, the in-phase and out-of-phase aerodynamic components can still be defined and represented by Eqs.(A.9) and (A.10), respectively, but since the aerodynamic derivatives $C_{a\alpha}(y)$ and $C_{a\hat{q}}(y)$ become dependent on the complementary state variable $y(t)$, the associated integrals in Eq.(A.10) can not be evaluated explicitly. In this case, the in-phase and out-of-phase aerodynamic components may not provide a complete description of the unsteady aerodynamic characteristics. This result can be shown through the following analyses.

For the in-phase aerodynamic component $\bar{S}_{in}$, Eq.(A.10) gives

$$\begin{aligned} \bar{S}_{in} &= \frac{1}{T}\{\int_0^T [C_{a0} + C_{a\alpha}(y)\alpha_0] sin(\omega t)dt + \int_0^T C_{a\alpha}(y)\alpha_A sin^2(\omega t)dt + \\ &\quad \int_0^T C_{a\hat{q}}(y)\hat{q}_{max} cos(\omega t) sin(\omega t)dt\} \end{aligned} \tag{A.22}$$

Since $sin^2(\omega t)$ does not change sign on $[0, T]$, the Weighted Mean Value Theorem for integrals can be used to evaluate the second integral in Eq.(A.22) as,

$$\begin{aligned} \frac{1}{T}\int_0^T C_{a\alpha}(y)\alpha_A sin^2(\omega t)dt &= C_{a\alpha}(\xi_1)\alpha_A \frac{1}{T}\int_0^T sin^2(\omega t)dt \\ &= \frac{1}{2}C_{a\alpha}(\xi_1)\alpha_A \end{aligned} \tag{A.23}$$

where ξ_1 is a value of $y(t)$ at some time instant, which depends on input amplitude α_A and frequency ω in general.

One can see, from Eq.(A.23), that $C_{a\alpha}(\xi_1)$ is actually the weighted Mean Value of $C_{a\alpha}(y)$ in a period and this value is generally function of the input amplitude and frequency. We define

$$\overline{C}_{a\alpha}(\alpha_A,\omega) \triangleq \frac{\int_0^T C_{a\alpha}(y)sin^2(\omega t)dt}{\int_0^T sin^2(\omega t)dt} \tag{A.24}$$

Thus, the in-phase aerodynamic component $\bar{S}_{in}$ can be expressed as

$$\bar{S}_{in} = \frac{1}{2}\overline{C}_{a\alpha}(\alpha_A,\omega)\alpha_A + \varepsilon_1(\alpha_A,\alpha_0,\omega) \tag{A.25}$$

where

$$\begin{aligned}\varepsilon_1(\alpha_A,\alpha_0,\omega) &= \frac{1}{T}\{\int_0^T [C_{a0}+C_{a\alpha}(y)\alpha_0]sin(\omega t)dt + \int_0^T C_{a\hat{q}}(y)\hat{q}_{max}cos(\omega t)sin(\omega t)dt\} \\ &= \frac{1}{T}\int_0^T [C_{a\alpha}(y)\alpha_0 + C_{a\hat{q}}(y)\hat{q}_{max}cos(\omega t)]sin(\omega t)dt \end{aligned} \tag{A.26}$$

and $\varepsilon_1(\alpha_A,\alpha_0,\omega)$ is negligible if the aerodynamic derivatives $C_{a\alpha}(y)$ and $C_{a\hat{q}}(y)$ are close to constants.

Similarly, the out-of-phase aerodynamic component $\bar{S}_{out}$ can be expressed as,

$$\bar{S}_{out} = \frac{1}{2}\overline{C}_{a\hat{q}}(\alpha_A,\omega)\hat{q}_{max} + \varepsilon_2(\alpha_A,\alpha_0,\omega) \tag{A.27}$$

where

$$\begin{aligned}&\overline{C}_{a\hat{q}}(\alpha_A,\omega) \triangleq \frac{\int_0^T C_{a\alpha}(y)cos^2(\omega t)dt}{\int_0^T cos^2(\omega t)dt} \\ &\varepsilon_2(\alpha_A,\alpha_0,\omega) \triangleq \frac{1}{T}\int_0^T C_{a\alpha}(y)[\alpha_0+\alpha_A sin(\omega t)]cos(\omega t)dt \end{aligned} \tag{A.28}$$

From Eqs.(A.25) and (A.27), we can see that the in-phase and out-of-phase aerodynamic components roughly give the estimations of the Weighted Mean Values of the aerodynamic

Table A.1: Oscillatory motion around zero mean angle of attack ($\alpha_0 = 0^o$)

$\hat{C}_{a\alpha}$	$\hat{\omega}_1$	$\hat{\omega}_2$	$\hat{C}_{a\hat{q}}$	$\hat{\omega}_1$	$\hat{\omega}_2$
$\alpha_A = 5^o$	4.6168	4.6234		2.3088	3.1351
$\alpha_A = 10^o$	4.6330	4.6385		2.5299	3.4086

Table A.2: Oscillatory motion around 20^o mean angle of attack ($\alpha_0 = 20^o$)

$\hat{C}_{a\alpha}$	$\hat{\omega}_1$	$\hat{\omega}_2$	$\hat{C}_{a\hat{q}}$	$\hat{\omega}_1$	$\hat{\omega}_2$
$\alpha_A = 5^o$	2.4855	2.4128		14.6354	16.2924
$\alpha_A = 10^o$	2.4521	2.4058		16.1935	19.6091
$\alpha_A = 20^o$	2.3354	2.4229		21.3063	28.2020

derivatives $C_{a\alpha}$ and $C_{a\hat{q}}$ in a period if the residual terms, ε_1 and ε_2, are negligible. These two Weighted Mean Values can depend on the amplitude and the frequency of the oscillations. In such a case, we may not be able to obtain much information of unsteady aerodynamic characteristics just from the in-phase and out-of-phase aerodynamic components.

A.4 Simulation Results

In order to illustrate the above discussions about the in-phase and out-of-phase aerodynamic components, we simulate the state-space model of the F-18 aircraft obtained as Eqs.(6.13) and (6.14) in Chapter 6 for harmonic oscillatory motions and compute the in-phase and out-of-phase aerodynamic components for lift coefficient. Then we scale these computed in-phase and out-of-phase components as,

$$\begin{aligned} \hat{C}_{L\alpha} &= \frac{2}{\alpha_A}\bar{S}_{in} \\ \hat{C}_{L\hat{q}} &= \frac{2}{\hat{q}_{max}}\bar{S}_{out} \end{aligned} \tag{A.29}$$

We compute the results discussed above for the oscillatory motion with two frequencies, two mean angles of attack, and three amplitudes. Table A.1 lists the computed results for

zero mean angle of attack while Table A.2 lists the results for 20^o mean angle of attack. In Tables A.1 and A.2, $\hat{\omega}_1 = 0.0542$ and $\hat{\omega}_2 = 0.1084$ are corresponding reduced frequencies.

From Tables A.1 and A.2, one can see that the scaled in-phase and out-of-phase aerodynamic components depend on the amplitudes, the frequencies, and the mean angles of attack of the oscillations. This result occurs because the computed values as shown in the tables are the weighted values of the time histries of the corresponding derivatives. These weighted values are not constant for different oscillatory motions.

Vita

Yigang Fan was born on August 22, 1960, in Kunming, China. He obtained the B.S. degree in aerospace engineering in 1982 and the M.S. degree in electrical engineering in 1986, both from the Northwestern Polytechnical University (NPU), Xian, China. Following that, he worked as a faculty member in the Department of Marine Engineering at Northwestern Polytechnical University. From 1993 to 1994, he was a visiting scholar in the Department of Aerospace and Ocean Engineering at Virginia Polytechnic Institute and State University, Blacksburg, Virginia. In 1994, he entered the Doctor of Philosophy program in aerospace engineering at Virginia Tech and obtained the Ph.D. degree in November 1997. In December 1997, he started working as a Post-Doctoral Research Associate also in aerospace engineering at Virginia Tech.

Yigang Fan is member of National Honor Society of **Phi Kappa Phi**